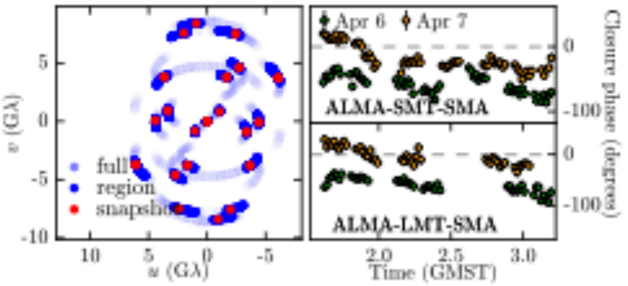

Figure 24. Left: (u, v)-coverage for the selected time window for dynamic imaging and modeling. The light-blue points show the coverage of the full night of observation, while the dark-blue points and the red points represent the coverage for the selected dynamic imaging region and a single 60 s snapshot from that region, respectively. Right: closure phases for Sgr A* (green and yellow) on two representative triangles during the selected time region.

9.2. Dynamic Imaging and Modeling Methods

To analyze Sgr A*'s spatially resolved dynamics during the 100-minute selected region of time on April 6 and 7, we use two methods: dynamic imaging and snapshot geometric modeling (also simply referred to as dynamic modeling). Both methods fit EHT 2017 data on 60 s snapshot integrations within the selected observation window but make different prior assumptions about the structure of the source in space and time. Note that, unlike in static imaging, we do not flux-normalize the data before dynamic analysis. Because the (u, v)-coverage is sparse even in the best available time window, both methods need to make strong prior assumptions about the spatial and/or temporal structure of the source to constrain the fits to the data. Note that when performing dynamic imaging/modeling fits we *do not* include a variability noise budget as is done in static imaging (Section 3.2.2).

Dynamic Imaging.—Dynamic imaging methods reconstruct a time-evolving image that best fits the observed evolution of Sgr A*. Our dynamic imaging approach is based on `StarWarps` (Bouman et al. 2018), which enforces continuity across an image and in time by means of spatial and temporal regularization (Section 4.4.2). Temporal regularization is set by a parameter β_Q^{-1}, which corresponds to the allowed variance between pixels in snapshots that are typically 60 s apart;[157] smaller values of β_Q^{-1} correspond to stronger continuity in time. Spatial regularization is imposed by a multivariate Gaussian prior on snapshots with a mean μ and covariance Λ that encourages spatial smoothness (see Equation (7) and Bouman et al. 2018). We examine the sensitivity of time-variable image features (e.g., PA) to different settings in the `StarWarps` imaging algorithm by running surveys over different values of the spatial regularization covariance Λ and data weights of the visibility amplitude and log closure amplitude; we typically keep β_Q^{-1} and the mean image μ fixed and examine the sensitivity of our results to these parameters separately across different surveys. Unless specified otherwise, in this paper we set β_Q^{-1} to 5×10^{-6} (Jy pixel^{-1})^2 and the prior mean μ and initialization image to an image of a uniform ring blurred by a 25 μas beam. These surveys result in distributions of the image features at each snapshot in time. For each of the measurements obtained from 54 parameter combinations, we draw 100 random samples from a normal distribution characterized by the image feature measurement and its associated error. These survey results are *not* posterior probability distributions, but they do provide a sense of the robustness of the sensitivity of movie reconstructions to changes in the algorithm parameters.

Geometric Modeling.—In our geometric modeling approach, a simple geometric model is fit to each 60 s snapshot *independently*, with no enforced correlations in time.[158] We consider several different m-ring models (Johnson et al. 2020), described by infinitesimally thin rings with azimuthal brightness variations decomposed into Fourier modes, which are subsequently blurred with a circular Gaussian kernel. The complexity of an m-ring model depends on the maximum number of Fourier modes, m, that are added (e.g., $m = 1$ corresponds to a simple crescent). To model a central floor, we include a Gaussian that is located at the center of the ring; the size and brightness of the Gaussian are additional model parameters.

For each m-ring model considered, we produce a multidimensional posterior using two modeling approaches. First, we consider a variational-inference-based approach, `DPI`, that fits to the log closure amplitudes and closure phases (Sun & Bouman 2021; Sun et al. 2022). Second, we consider a sampling-based method, `Comrade` (P. Tiede 2022, in preparation),[159] which fits to visibility amplitudes and closure phases. `Comrade` uses the nested sampling package `dynesty` (Speagle 2020) and the probabilistic programming language `Soss` (Scherrer & Zhao 2020). The different data products used by `DPI` and `Comrade` imply different assumptions made about the telescope amplitude gains—they are unconstrained in `DPI`, while in `Comrade` the gain amplitudes are more constrained and are included as model parameters during fitting (see Paper IV). As a result of these different data products, `DPI` and `Comrade` produce slightly different posteriors. Details of the geometric modeling approaches are further explained in Paper IV.[160]

Comparing Dynamic Imaging and Modeling.—Both dynamic imaging and modeling share a common goal of extracting time-resolved and spatially resolved structure in Sgr A*, but there are key differences between the methods in how prior assumptions about the spatial and temporal variability are incorporated. `StarWarps` imaging allows for more freedom in the recovered spatial structure but assumes strong temporal regularization between frames. In contrast, snapshot geometric modeling is restricted to a parameterized set of spatial structures but makes no assumptions on image correlations in time. Although snapshot geometric modeling cannot recover spatial structures outside of the m-ring model specifications, it allows for quantifying the uncertainty in m-ring model features (and their temporal variability), as it estimates full posterior distributions for the particular geometric model used.

Diagnostics.—To characterize our dynamic reconstructions, we mostly investigate trends of the brightness PA (see Equation (21) in M87* Paper IV) with time. The PA is a simple and easily characterizable feature of the brightness distribution around an asymmetric ring. For `Starwarps` reconstructed movies, we extract the ring PA on the different snapshots using

---

[157] Frames are sometimes separated by more than 60 s owing to the interval between scans.

[158] In the language of the temporal regularization parameter defined above, for geometric modeling $\beta_Q^{-1} \to \infty$.

[159] https://github.com/ptiede/Comrade.jl

[160] Note that model fits in Paper IV use 120 s snapshots, whereas in this section we use 60 s snapshots.

`REx`; in m-ring model fitting results, the PA is obtained directly from the fitted model as the argument of the first azimuthal Fourier mode.

Ring Assumption.—Many of the results in this section apply strong prior assumptions that Sgr A*'s underlying structure is ring-like, motivated by the ring morphology recovered in static image reconstructions using the full (u, v)-coverage (Section 7). `StarWarps` reconstructions enforce a ring constraint by setting the mean prior image μ to a ring with $\approx$50 μas diameter and a width set by a circular Gaussian blurring kernel. In geometric modeling, the ring assumption is intrinsically imposed by the structure of the m-ring model. In Section 9.4.1 and Appendix J we explore the sensitivity of our results to the choice of mean image μ in `StarWarps`.

9.3. Synthetic Data Tests

Sparse snapshot (u, v)-coverage can lead to artifacts in both imaging and geometric modeling results. These artifacts appear in static imaging but are further amplified in dynamic imaging owing to the far-sparser coverage (Farah et al. 2022). Thus, it is important to assess how the sparse (u, v)-coverage during the selected time window may affect the recovered results and whether it may introduce biases in recovered image features, particularly the PA of ring-like images.

9.3.1. Static Crescents

In Appendix J.3 we present synthetic data tests conducted to characterize the effect of the sparse snapshot EHT2017 (u, v)-coverage on PA recovery from static crescent images. These tests show that there are significant biases in the recovered PA from 60 s snapshots when the brightness asymmetry of the ground-truth ring image is low. When there is a strong asymmetry in the brightness distribution around the ring, however, the PA is accurately recovered even with 60 s snapshot (u, v)-coverage.

9.3.2. GRMHD Simulations

We explored how our methods perform in recovering time-varying PAs from three selected GRMHD simulation movies. We used three representative GRMHD movies from the GRMHD library presented in Paper V (see Section 5.2).[161] We generated visibility data from the three movies over the 100-minute dynamic analysis window on April 7 using the same procedure described in Section 5, including atmospheric noise, telescope gain errors, and polarimetric leakage.

Figure 25 presents results obtained from both dynamic imaging and modeling reconstructions of these three synthetic data sets. The ground-truth simulation PA evolution is recovered (with $\sim 30^\circ$) for the first two models (Simulations 1 and 2). However, there are several localized deviations in the recovered PA distributions from the ground truth in these models, especially when the instantaneous (u, v)-coverage worsens (e.g., during the LMT dropout time region). For the third model (Simulation 3) both the dynamic imaging and modeling methods recover significant offset from the true PA. One potential cause of this offset is the prominent extended jet structure to the northwest of the ring in the SANE simulation. This extended structure cannot be captured in either the dynamic imaging or modeling methods owing to their strong prior assumptions of a ring-like morphology.

In the bottom row of Figure 25, we investigate the complex variance of the Fourier transform of the reconstructed images across the selected time window for both the ground-truth (scattered) movies and the reconstructions. We find that in all three cases the reconstructions tend to introduce more variability than is present in the ground truth. In Simulations 1 and 2 this excess variability does not prevent the reconstructions from qualitatively recovering the correct PA trend, but the PA results are not correctly recovered in Simulation 3.

These results indicate that although we often recover the PA accurately from some realistic synthetic GRMHD data sets, we should remain cautious when interpreting Sgr A* dynamic results. Our methods sometimes incorrectly recover the PA, especially if extended structure is present that is not captured by the prior assumptions on the source structure made by the dynamic imaging and modeling methods. In addition to effects from extended structure, there may be additional uncharacterized systematic uncertainty from prior assumptions in the reconstructions in these results derived from extremely sparse snapshot Sgr A* coverage.

9.4. Sgr A* Spatiotemporal Characterization and Uncertainty

Here we present results of our analysis on Sgr A*'s spatially resolved temporal variability on minute timescales on April 6 and 7, using both dynamic imaging and snapshot geometric modeling methods. In Figure 26, we show detailed results for the Sgr A* PA evolution and data fits reconstructed using a restricted range of dynamic imaging and modeling parameters. In Figure 27 we show PA results obtained under a broader range of parameter settings.

In general, we find that snapshot geometric modeling results performed under different m-ring orders, scattering mitigation strategies, and modeling codes produce fairly consistent results. The modeling results show broad posteriors of PA at each 60 s snapshot but still indicate significant differences between April 6 and 7 and between the first and second halves of the 100-minute window on April 7. In rough terms, the PA on April 6 is centered around $\sim -50^\circ$, with some scatter around this value over the time window. In contrast, on April 7 the modeling results show PA posteriors that are initially centered around $\sim 90^\circ$ and then shift to values centered around $\sim -50^\circ$ in the second half of the time window.

Compared to snapshot geometric modeling, dynamic imaging allows for more freedom in spatial and temporal regularization and, as a result, is more sensitive to parameter choices. Dynamic imaging results can produce movies that reproduce the PA trends on April 6 and 7 recovered by snapshot modeling. These PA trends—a stable PA on April 6 and a shifting PA on April 7—are predominantly seen in dynamic imaging reconstructions with low temporal regularization and ring-like spatial priors. Geometric modeling makes similar assumptions, imposing no temporal regularization and enforcing ring structure in the form of the model. In Figure 26, we directly compare dynamic modeling and imaging results under these strong assumptions.

Even in the limited space of dynamic imaging reconstructions conducted with weak temporal regularization and ring-like mean prior images, the imaging results are sensitive to

---

[161] Simulations 1 and 2 are using a MAD GRMHD model with parameters $a_* = 0, i = 10, R_{\rm high} = 10$. Simulation 3 is using a SANE GRMHD model with $a_* = -0.94, i = 50, R_{\rm high} = 160$.

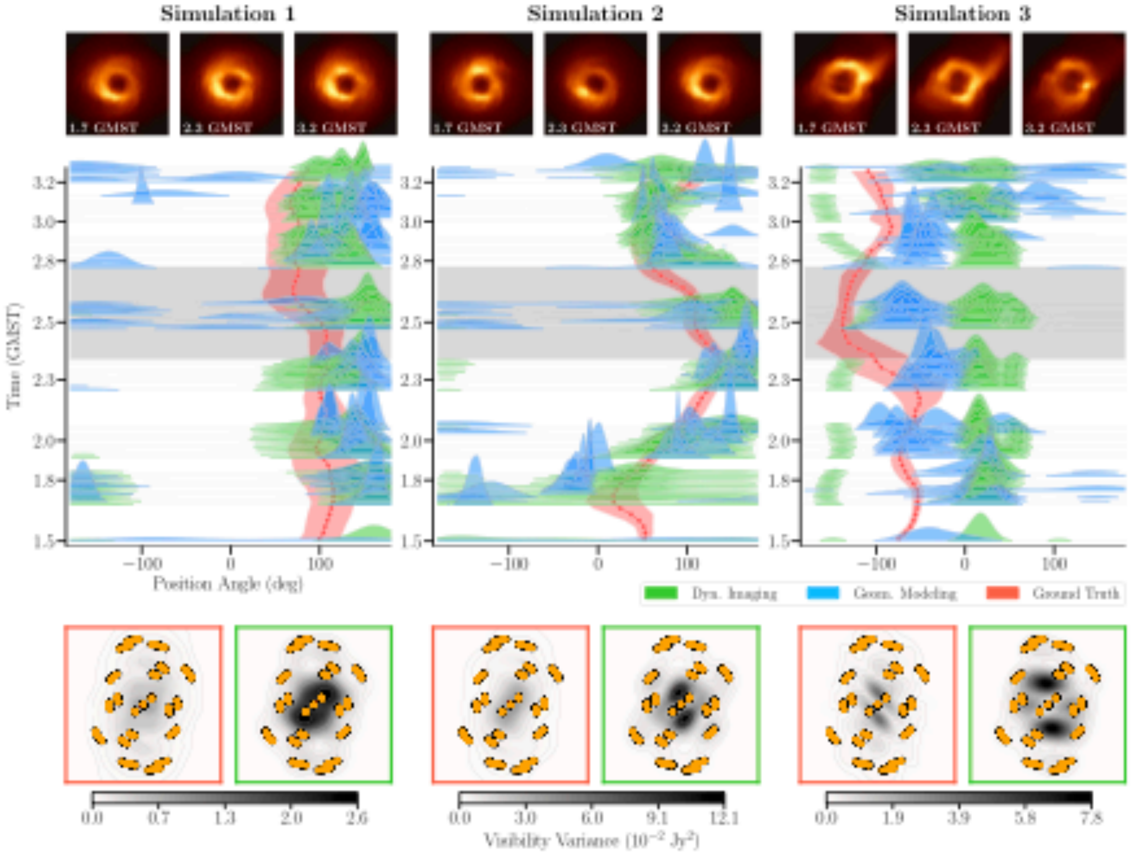

Figure 25. PA recovered from synthetic data from three different GRMHD simulations on April 7 EHT coverage during the dynamic analysis window using both `StarWarps` dynamic imaging and `DPI` snapshot geometric modeling techniques. Top row: ground-truth GRMHD movie snapshots (including interstellar scattering) from each of the three simulations at 1.7, 2.3, and 3.2 GMST. Middle row: plots of PA vs. time for the reconstructions compared with the simulation ground truth (in red). The shaded red region indicates the circular standard deviation of the ground-truth PA computed using `REx` (refer to Section 8 and Chael 2019). Modeling histograms (blue) correspond to actual marginal posterior distributions, whereas for `StarWarps` imaging the histograms represent the distribution of PAs and their associated uncertainties for a collection of movies reconstructed under different parameter settings. The gray band at roughly 2.6 GMST indicates the time period where the LMT dropped out of the observation. Bottom row: visibility variance in the (u, v)-plane over the selected time window for the ground-truth simulation movies (left, red) and the reconstruction (right, green). In Simulations 1 and 2, both dynamic imaging and snapshot geometric modeling methods are often able to correctly identify the PA of evolving GRMHD movies during this time window, but they show significant offsets from the correct PA in Simulation 3. From left to right, the maximum variance of the ground-truth (reconstructed) movie is 0.85 (2.62) × 10^{-2} Jy^2, 4.45 (12.07) × 10^{-2} Jy^2, and 3.94 (7.79) × 10^{-2} Jy^2. Contours start at 90% of the peak variance and decrease by successive factors of 2 until they reach 0.7%.

other hyperparameters. In particular, Figure 26 indicates that we recover two modes of PA evolution on April 7 even with the mean prior image and temporal regularization level fixed. We present representative snapshots and fit to the closure phase data from these two modes in the right panels of Figure 26.

When the ring-like mean image prior is changed or the weak temporal regularization is increased in `StarWarps` dynamic imaging, significantly different PA variations can be recovered from the same data. In Figure 27, we show that when the ring assumption is relaxed and a disk prior is used in reconstruction, `StarWarps` results show drastically different PA trends over time. In particular, in reconstructions initialized with a disk prior, the PA curves on April 6 and 7 appear to be flipped by 180° (i.e., on April 7 the PA transitions from ∼90° to ∼−50°). We further show in Figure 28 that when using stronger temporal regularization in the `StarWarps` dynamic imaging the PA stays constant, eliminating the shift from positive to negative PA trend on April 7. We discuss these tests further in Section 9.4.1 and Appendix J.5.

Note that April 6 and 7 have nearly identical (u, v)-coverage during the selected 100-minute region of time. We can thus compare the results obtained over these 2 days to help disentangle effects of (u, v)-coverage from any effects due to intrinsic evolution. If the PA trends that we recover are due primarily to biases from the (u, v)-coverage, we would expect to recover the same PA trends on both days. However, we consistently see different PA trends with time using the same parameter settings in both dynamic imaging and modeling methods. This implies that differences in the visibilities, not the (u, v)-coverage, drive differences in the PA evolution we see on the two nights in some reconstructions, but it does not help select among any of the different reconstruction modes on either day.

9.4.1. *Effect of Model and Imaging Choices*

The PA evolution recovered with dynamic imaging and modeling methods is sensitive to choices made in the imaging and modeling procedures that enforce constraints on the spatial and temporal structure of the reconstructions. Enforcing strong spatial or temporal priors will suppress any structural variability, while adding too much flexibility in a model with sparse data constraints will lead to overfitting or uninformative posteriors. In Appendix J.5 we present in detail several tests of

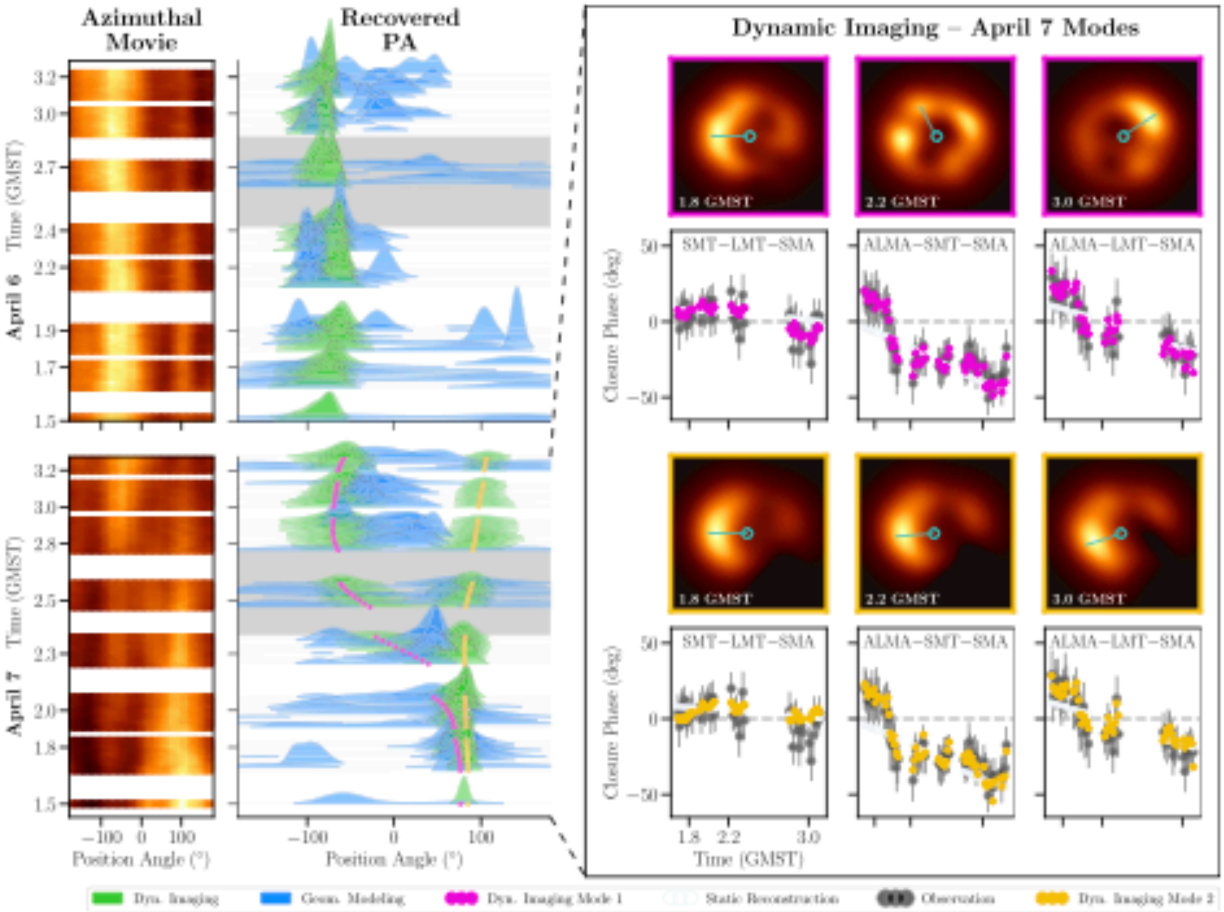

Figure 26. Left: mean azimuthal brightness profiles from the `StarWarps` movie reconstructions, unwrapped around the ring as a function of time, and PA distributions obtained from dynamic imaging and snapshot geometric modeling reconstructions of EHT Sgr A* data on April 6 (top) and 7 (bottom) in the selected time window. Geometric modeling distributions are marginal PA posteriors from `DPI`. Imaging histograms represent the distribution of PAs and their associated uncertainties from a collection of `StarWarps` movies reconstructed under different parameter settings with the spatial prior mean μ and temporal regularization β_Q^{-1} held fixed (refer to Equation (7)). Blank spaces indicate time regions without any data. The gray band at roughly 2.6 GMST indicates the region where the LMT dropped out and data coverage is poor. Both dynamic imaging and modeling appear to identify a nearly constant PA on April 6 but a variable PA over the same time window on April 7. In the reconstructions in this figure, both dynamic imaging and modeling make a prior assumption that the source morphology is ring-like; `StarWarps` imaging uses a prior/initialization image of a uniform ring, while geometric modeling uses a second-order *m*-ring ($m = 2$) model. Both dynamic imaging and modeling recover "descattered" movies using the `J18model1` refractive noise model. Right: focus on the two modes reconstructed by `StarWarps` on April 7. For each mode, the top panels show three reconstructed snapshots at different times, and bottom panels compare the fitting of the corresponding reconstructed movie (magenta or yellow) and a representative static reconstruction from the `eht-imaging` static imaging pipeline (white) to the closure phase data measured by three key triangles. The dynamic reconstruction on the top (magenta) shows an evolving PA shift over the observation window. In contrast, the reconstruction on the bottom has a nearly constant PA of ~100° (yellow). In the selected closure phase plots (bottom rows), the measured data are averaged in 60 s snapshots and the error bars do not include a variability noise model. The static image visibilities (white) capture the general trend of the data, but they do not well fit variability in the closure phases. In contrast, both selected `StarWarps` dynamic reconstructions better fit the data on minute timescales. We find that the fit's behavior on the SMT–LMT–SMA triangle has a large influence on the resulting PA of the movie on April 7. A positive SMT–LMT–SMA closure value tends to result in a southeast PA (~100°), whereas a negative value results in a more northwest PA (~−80°).

these choices for both imaging and modeling methods; here we highlight the most important results.

Spatial Priors.—Constraints on the spatial structure are enforced via the *m*-ring order in geometric model fitting and via the choice of mean image prior in dynamic imaging. To test the effects of different mean prior images in `StarWarps`, we produced reconstructions using uniform ring priors with increasing widths (from convolution of the ring described in Section 5 with circular beams of 11, 15, 20, and 25 μas FWHM; henceforth ring*11μ as, ring*15μas, ring*20μas, and ring*25μas priors, respectively). We also used a tapered disk with diameter ~74 μas (see Figure 7) as a prior that does not feature any central dip after convolution of the disk with a circular beam of 15 μas (henceforth, disk*15μas prior). We discuss the details of these prior choices in Appendix J.5.1. For geometric modeling, we tested ring-like models of increasing complexity in their azimuthal brightness distribution, from crescent models ($m = 1$) to higher-order *m*-rings. When fitting *m*-rings to Sgr A* snapshot data, we explored *m* from 1 to 4 and selected the order to use based on the Bayesian evidence across all data sets—settling on $m = 2$ (see Appendix J.5.2).

Figure 27 shows histograms of the dynamic imaging PA results made using different mean prior images and PA posterior distributions from geometric modeling results from different *m*-ring orders. We also compare modeling results from two different modeling codes in Figure 27. The reconstructed PA trends are fairly consistent on both days among the different *m*-ring orders in geometric model fitting. In

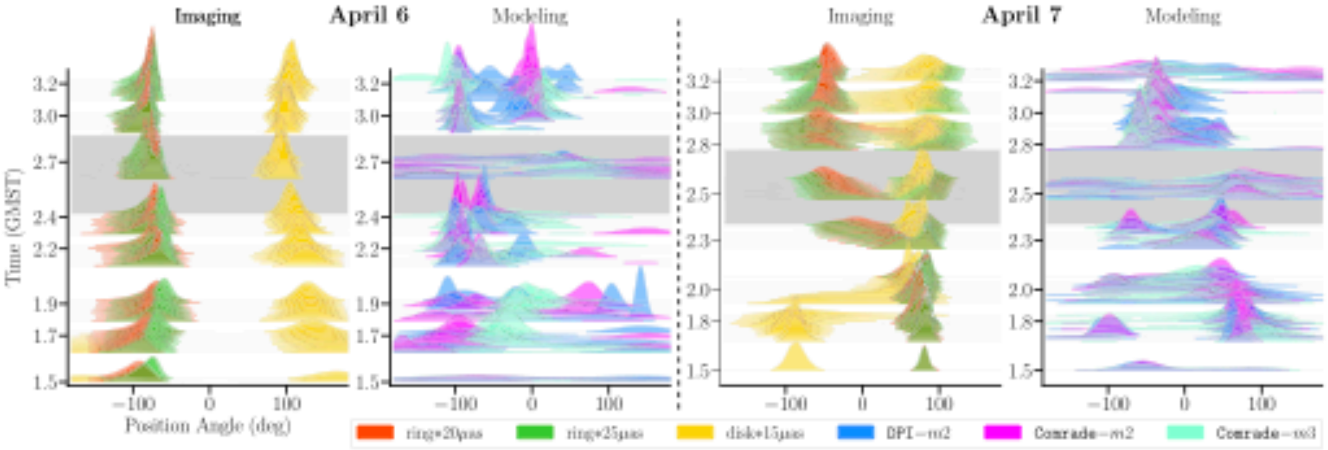

Figure 27. The PA for the 2017 Sgr A* data recovered using dynamic imaging and geometric modeling techniques under different assumptions. `StarWarps` imaging results were obtained using a spatial prior image set to either a uniform ring convolved with a circular Gaussian kernel with FWHM of 20 or 25 μas (see Figure 7) or a uniform disk blurred with a kernel with FWHM of 15 μas. Descattered modeling results were obtained from geometric models with increasing complexity (*m*-ring 2 vs. *m*-ring 3) and different fitting software packages (`DPI` vs. `Comrade`). All results were obtained from low-band data on April 6 and 7 that have been descattered with a `J18model1` refractive noise floor. The gray band at roughly 2.6 GMST indicates the region where the LMT has dropped out and data coverage is poor.

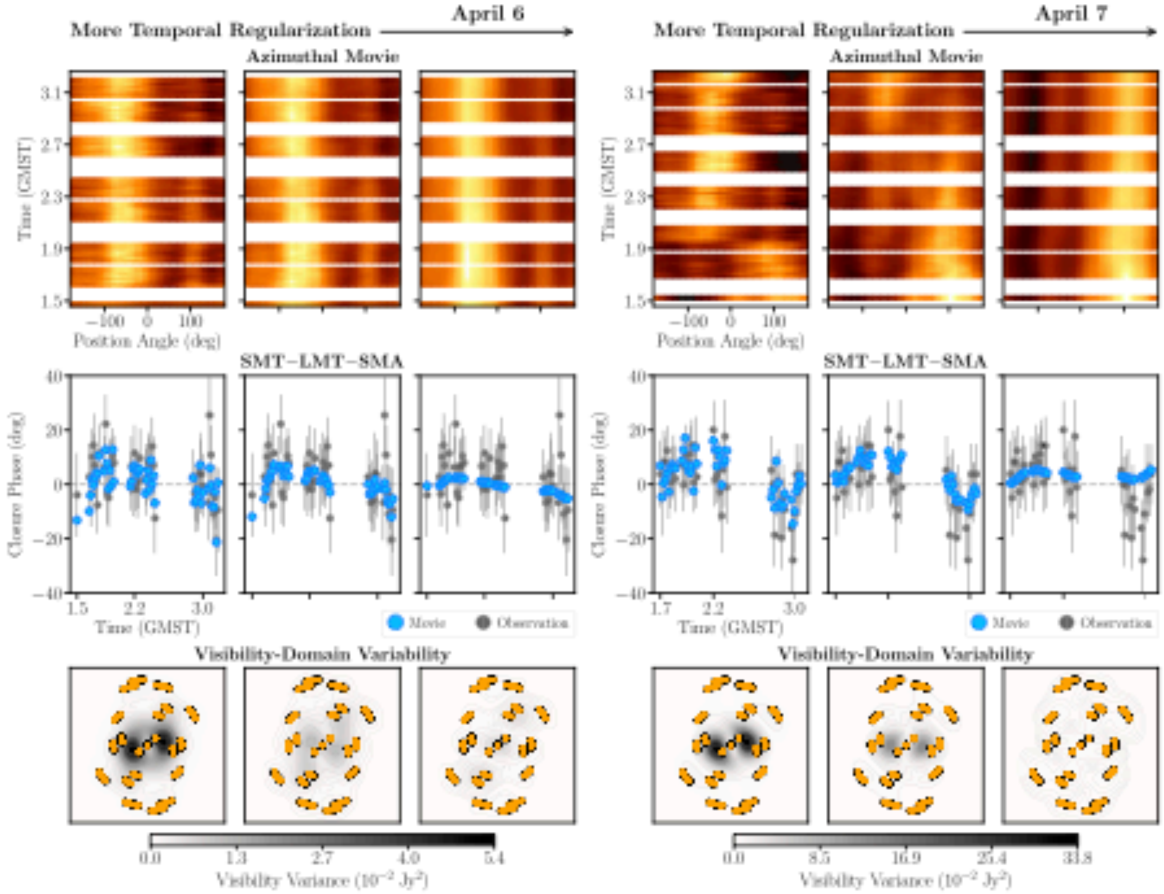

Figure 28. Comparing the effect of temporal regularization on the reconstructed `StarWarps` movies for April 6 and 7. The temporal regularization strength is increased from left to right ($\beta_Q^{-1} = 5 \times 10^{-4}$ (Jy pixel^{-1})^2, 5×10^{-6} (Jy pixel^{-1})^2, and 5×10^{-8} (Jy pixel^{-1})^2). For each value of β_Q^{-1}, we show the mean unwrapped movie around the ring (top), the mean closure phase values on the triangle SMT–LMT–SMA (middle), and the variance of the complex visibilities across the (u, v)-plane (bottom). As temporal regularization is increased, the recovered movies become more static and the degree of (u, v)-plane variability decreases. From weak to strong regularization, the maximum variance of the reconstructed movie is 5.37×10^{-2} Jy^2, 1.11×10^{-2} Jy^2, and 0.73×10^{-2} Jy^2 on April 6 and 33.81×10^{-2} Jy^2, 13.24×10^{-2} Jy^2, and 0.50×10^{-2} Jy^2 on April 7. Contours start at 90% of the peak variance and decrease by successive factors of 2 until they reach 0.7%. For comparison, the variance in the light curve over this interval is $\sim 0.5 \times 10^{-2}$ Jy^2. Thus, the leftmost reconstruction with the weakest temporal regularization produces a movie with visibility variance substantially exceeding the light-curve variance due to overfitting to the thermal noise.

`StarWarps` imaging, reconstructions using ring-like mean prior images of several different thicknesses produce similar trends, with a stable PA on April 6 and a PA transition from positive to negative values on April 7. However, when a disk prior is used in `StarWarps`, the PA trends of both April 6 and 7 change drastically and appear to be flipped by 180°. Figure 44 in Appendix J shows image snapshots and data fits for `StarWarps` reconstructions with both disk and ring mean prior images. Note that although the PA evolution is different from the movie reconstructed using a ring prior, the movie reconstructed with a disk prior still results in a ring-like structure, though with a less prominent central brightness depression.

Temporal Regularization.—Geometric modeling enforces no correlations in between temporal snapshots, while dynamic imaging can enforce correlations via temporal regularization. Figure 28 shows that when using stronger temporal regularization in `StarWarps` (lower values of β_Q^{-1}) the PA becomes constant in time on both April 6 and 7—a result of the method enforcing strong continuity between frames. Note that in the case of high temporal regularization the SMT–LMT–SMA closure triangle fits in the second half of the time window on April 7 appear offset with respect to the data, although still within two standard deviations of most data points.

We also show that reconstructions with low levels of temporal regularization produce prominent variance in the model visibilities plane at (u, v) points that are not sampled by our coverage during this time window.[162] In contrast, reconstructions with more temporal regularization lower the overall variance of model visibilities everywhere in the Fourier plane and place the peaks in the variance maps at (u, v) points sampled by the EHT. We discuss the interpretation of the different temporal regularization values β_Q^{-1} used here in Appendix J.2 and further tests of the `StarWarps` temporal regularization in Appendix J.5.1.

Scattering.—Another choice made in both dynamic imaging and modeling procedures common to both static and dynamic reconstruction methods is the strategy for mitigating the effects of interstellar scattering in Sgr A* data. We investigate the effects of the same five prescriptions for scattering mitigation we use in static imaging on the dynamic reconstructions in Appendix J.4. In general, we find that choices made in the scattering mitigation procedure contribute less to our overall uncertainty than choices related to the spatial prior or temporal regularization.

9.5. Sgr A Dynamic Property Conclusions*

Our aim in this section has been to use the 2017 EHT data to explore spatially resolved dynamics of Sgr A* on minute timescales. First, we identified the time windows with the best (u, v)-coverage during the observation run—a roughly 100-minute window on April 6 and 7. We identify a significant difference between the closure phases on April 6 and 7, signifying that the underlying structure is different on the 2 days. We reconstruct movies from this small slice of the EHT data using dynamic imaging and geometric snapshot modeling methods. We track the average PA in our dynamic imaging and modeling results as a way of following a specific, dynamic, and measurable aspect of the source over time. We find that we are able to recover the PA in synthetic EHT data from some GRMHD simulation movies; however, there are prominent cases when this is not the case and both geometric modeling and dynamic imaging methods recover biased results.

On April 6, most dynamic imaging and modeling results show a stable PA in the Sgr A* images over the selected window. In contrast, the recovered PA evolution on April 7 is more dependent on prior assumptions on the spatial structure and temporal regularization. On April 7, when using a ring image as a spatial prior and weak temporal regularization, dynamic imaging results largely align with geometric modeling results and show an evolution in the PA of ~140° over the ~100-minute window. However, we also see several other PA trends in the dynamic imaging results, including a PA evolution in the opposite direction and modes where the PA is static on both days.

These results, along with our synthetic data tests, show that while the 230 GHz image of Sgr A* may exhibit interesting and measurable dynamics, our current methods cannot conclusively determine the PA evolution of Sgr A*. Dynamic reconstructions of Sgr A* with EHT2017 coverage should thus be interpreted with caution. This analysis provides a promising starting point for further studies of future evolution seen in Sgr A* EHT observations with denser (u, v)-coverage.

10. Summary and Conclusions

We present Sgr A* static and dynamic imaging results for data taken with the EHT in 2017 April. Sgr A* was observed with eight EHT stations at six geographic sites over five observing days, out of which the highly sensitive phased-ALMA array participated in April 6, 7, and 11. April 7 is the only day in which the easternmost station PV participated, providing the best (u, v)-coverage that probes a null at ~3.0 Gλ. On April 11 Sgr A* exhibits the highest variability in the light curve during the 2017 campaign (Wielgus et al. 2022), possibly related to an X-ray flare observed shortly before the start of the EHT observations (Paper II), rendering static imaging for this day particularly challenging. For these reasons, April 7 has been used as the primary data set, while April 6 is considered as a secondary data set. Results from the remaining 2017 EHT observations of Sgr A* will be presented in future publications.

Similar to the 2017 EHT observations of M87* (M87* Papers I–VI), the data sets analyzed in this paper are the first with sufficient sensitivity and (u, v)-coverage to reconstruct images of Sgr A* on event horizon scales with an angular resolution of ~20 μas. Imaging Sgr A* with the EHT is, however, significantly more challenging than M87* owing to the interstellar scattering toward the Galactic center, and most importantly the rapid intraday variability that characterizes Sgr A*, with timescales much shorter than the duration of our typical EHT observing runs.

To mitigate the scattering effects in our Sgr A* reconstructions, we have developed a strategy based on Fish et al. (2014), Psaltis et al. (2018), and Johnson et al. (2018) to account for the angular broadening and substructure induced by diffractive (Section 3.1.1) and refractive (Section 3.1.2) scattering, respectively. Images of Sgr A* have been obtained with and without these scattering mitigation prescriptions to assess their impact in our reconstructions.

---

[162] As shown in the GRMHD synthetic data tests, it is not necessary that the peaks in the (u, v)-plane variability map align with measured data points to correctly identify PA evolution.

It is, however, the rapid intraday intrinsic variability of Sgr A*, coupled with the sparse (u, v)-coverage as compared with regular VLBI observations, that poses the strongest challenge for reconstructing horizon-scale images of Sgr A* with the EHT. With a typical variability timescale of a few minutes, the horizon-scale brightness distribution can change significantly during our typical multihour observing runs, which violates the fundamental assumption for Earth-rotation VLBI aperture synthesis. To overcome this extraordinary challenge, we have included a "variability noise budget" in the observed visibilities (Section 3.2.2) that facilitates the reconstruction of static full-track images capturing the time-averaged structure.

Static full-track imaging of Sgr A* has been conducted through surveys over a wide range of imaging assumptions using the classical CLEAN algorithm (implemented in `DIFMAP`), RML methods (`eht-imaging` and `SMILI`), and a Bayesian posterior sampling method (THEMIS), as described in Section 4. Imaging surveys, exploring $\sim 10^3$–10^5 parameter combinations, were first performed on synthetic data sets designed to be qualitatively consistent with Sgr A* measurements, including its characteristic temporal variability (Section 5). The use of synthetic data sets allows us to assess the capability to accurately reproduce different morphologies with our imaging methods and to select the "Top Sets": imaging parameter combinations for RML and CLEAN methods that successfully reproduce the known ground-truth movies (Section 6.2.2).

Unlike for M87*, where a persistent ring structure is observed across imaging pipelines (M87* Paper IV), our static reconstructions of Sgr A* show structural changes within and across the different imaging methods used. The variety of images can be classified into four main clusters of images corresponding to ring images with three different azimuthal brightness distributions and a cluster that contains a small number of nonring images with multiple morphologies. This classification is resilient to the scattering mitigation prescription used, including no mitigation.

Although the relative fraction of nonring images in the Top Set reconstructions from RML and CLEAN is very small ($\lesssim 5\%$ in the April 7 descattered images), we note that the Top Sets do not sample from the Bayesian posterior likelihood and are instead meant to characterize the range of possible images due to epistemic uncertainty. On the other hand, the full Bayesian imaging approach implemented in the THEMIS pipeline does provide a Bayesian posterior exploration that characterizes aleatoric uncertainty. Scattering-mitigated Sgr A* reconstructions from THEMIS for April 7 only contain ring images with a very similar structure to that found for RML and CLEAN methods, although it also identifies a small number (2%) of on-sky nonring images (Section 7).

The April 6 data set suffers from poorer (u, v)-coverage and likely more unusual intrinsic variability. This results in April 6 reconstructions that contain a less prominent ring structure in the RML and CLEAN pipelines. Nonetheless, the diameters of the ring structures recovered for April 6 are consistent with those of the April 7 ring images. In addition, although descattered THEMIS samples of April 6 primarily show a corrupted ring or nonring structure, THEMIS posterior samples for the combined April 6 and 7 data sets exhibit only clear ring-like images for both the on-sky and scattering-mitigated reconstructions.

Imaging of a synthetic GRMHD data set with data properties similar to those of Sgr A* and characterized by a ring image of $\sim 50\ \mu$as (Section 6.4.2) shows similar imaging results to those found in Sgr A*: RML and CLEAN methods recover ring images with different azimuthal orientations and a small ($\lesssim 5\%$) Top Set fraction of nonring images, while the THEMIS posterior sample only recovers ring images.

We conclude that the Event Horizon Telescope Sgr A* data show compelling evidence for an image that is dominated by a bright ring of emission. This conclusion is based on our extensive analysis of the effects of sparse (u, v)-coverage, source variability, and interstellar scattering, as well as studies of simulated visibility data, which find that nonring images are recovered in the minority by our imaging pipelines for variable sources with an intrinsic ring morphology (Section 7.5). Representative first event-horizon-scale images of Sgr A* are shown in Figure 13, obtained from the April 7 data set by averaging similar Top Set and posterior images together. Despite the different azimuthal brightness distributions observed, all ring images have a ring diameter of $\sim 50\ \mu$as on both April 6 and 7, consistent with the expected "shadow" of a $4 \times 10^6\ M_\odot$ black hole in the Galactic center located at a distance of 8 kpc.

We also present preliminary dynamic imaging and modeling analysis of Sgr A* on horizon scales in an attempt to characterize the azimuthal variations on minute timescales and their uncertainties. We applied dynamical analysis methods to a 100-minute interval of the 2017 Sgr A* data with the best coverage on April 6 and 7. On April 6, most dynamic imaging and modeling methods recover a stable PA. In contrast, on April 7 the recovered PA evolution is more dependent on spatial and temporal regularization; April 7 frequently shows an evolving PA over the 100-minute window when we impose strong priors on the spatial structure but weak temporal regularization. However, when expanding the parameter space available to the imaging and modeling methods, we recover disparate modes in the PA behavior, including some reconstructions that are nearly static. Our initial results show that significant uncertainty exists in any attempt to characterize the spatially resolved dynamics of Sgr A* using sparse EHT 2017 data, but this analysis provides a promising starting point for further dynamical studies of Sgr A* with future EHT observations.

We thank an anonymous referee for helpful suggestions that have improved this paper.

The Event Horizon Telescope Collaboration thanks the following organizations and programs: the Academia Sinica; the Academy of Finland (projects 274477, 284495, 312496, 315721); the Agencia Nacional de Investigación y Desarrollo (ANID), Chile via NCN19_058 (TITANs) and Fondecyt 1221421, the Alexander von Humboldt Stiftung; an Alfred P. Sloan Research Fellowship; Allegro, the European ALMA Regional Centre node in the Netherlands, the NL astronomy research network NOVA and the astronomy institutes of the University of Amsterdam, Leiden University and Radboud University; the ALMA North America Development Fund; the Black Hole Initiative, which is funded by grants from the John Templeton Foundation and the Gordon and Betty Moore Foundation (although the opinions expressed in this work are those of the author(s) and do not necessarily reflect the views of these Foundations); Chandra DD7-18089X and TM6-17006X; the China Scholarship Council; China

Postdoctoral Science Foundation fellowship (2020M671266); Consejo Nacional de Ciencia y Tecnología (CONACYT, Mexico, projects U0004-246083, U0004-259839, F0003-272050, M0037-279006, F0003-281692, 104497, 275201, 263356); the Consejería de Economía, Conocimiento, Empresas y Universidad of the Junta de Andalucía (grant P18-FR-1769), the Consejo Superior de Investigaciones Científicas (grant 2019AEP112); the Delaney Family via the Delaney Family John A. Wheeler Chair at Perimeter Institute; Dirección General de Asuntos del Personal Académico-Universidad Nacional Autónoma de México (DGAPA-UNAM, projects IN112417 and IN112820); the Dutch Organization for Scientific Research (NWO) VICI award (grant 639.043.513) and grant OCENW.KLEIN.113; the Dutch National Supercomputers, Cartesius and Snellius (NWO Grant 2021.013); the EACOA Fellowship awarded by the East Asia Core Observatories Association, which consists of the Academia Sinica Institute of Astronomy and Astrophysics, the National Astronomical Observatory of Japan, Center for Astronomical Mega-Science, Chinese Academy of Sciences, and the Korea Astronomy and Space Science Institute; the European Research Council (ERC) Synergy Grant "BlackHoleCam: Imaging the Event Horizon of Black Holes" (grant 610058); the European Union Horizon 2020 research and innovation programme under grant agreements RadioNet (No 730562) and M2FINDERS (No 101018682); the Generalitat Valenciana postdoctoral grant APOSTD/2018/177 and GenT Program (project CIDEGENT/2018/021); MICINN Research Project PID2019-108995GB-C22; the European Research Council for advanced grant 'JETSET: Launching, propagation and emission of relativistic jets from binary mergers and across mass scales' (Grant No. 884631); the Institute for Advanced Study; the Istituto Nazionale di Fisica Nucleare (INFN) sezione di Napoli, iniziative specifiche TEONGRAV; the International Max Planck Research School for Astronomy and Astrophysics at the Universities of Bonn and Cologne; DFG research grant "Jet physics on horizon scales and beyond" (Grant No. FR 4069/2-1); Joint Princeton/Flatiron and Joint Columbia/Flatiron Postdoctoral Fellowships, research at the Flatiron Institute is supported by the Simons Foundation; the Japan Ministry of Education, Culture, Sports, Science and Technology (MEXT; grant JPMXP1020200109); the Japanese Government (Monbukagakusho: MEXT) Scholarship; the Japan Society for the Promotion of Science (JSPS) Grant-in-Aid for JSPS Research Fellowship (JP17J08829); the Joint Institute for Computational Fundamental Science, Japan; the Key Research Program of Frontier Sciences, Chinese Academy of Sciences (CAS, grants QYZDJ-SSW-SLH057, QYZDJSSW-SYS008, ZDBS-LY-SLH011); the Leverhulme Trust Early Career Research Fellowship; the Max-Planck-Gesellschaft (MPG); the Max Planck Partner Group of the MPG and the CAS; the MEXT/JSPS KAKENHI (grants 18KK0090, JP21H01137, JP18H03721, JP18K13594, 18K03709, JP19K14761, 18H01245, 25120007); the Malaysian Fundamental Research Grant Scheme (FRGS) FRGS/1/2019/STG02/UM/02/6; the MIT International Science and Technology Initiatives (MISTI) Funds; the Ministry of Science and Technology (MOST) of Taiwan (103-2119-M-001-010-MY2, 105-2112-M-001-025-MY3, 105-2119-M-001-042, 106-2112-M-001-011, 106-2119-M-001-013, 106-2119-M-001-027, 106-2923-M-001-005, 107-2119-M-001-017, 107-2119-M-001-020, 107-2119-M-001-041, 107-2119-M-110-005, 107-2923-M-001-009, 108-2112-M-001-048, 108-2112-M-001-051, 108-2923-M-001-002, 109-2112-M-001-025, 109-2124-M-001-005, 109-2923-M-001-001, 110-2112-M-003-007-MY2, 110-2112-M-001-033, 110-2124-M-001-007, and 110-2923-M-001-001); the Ministry of Education (MoE) of Taiwan Yushan Young Scholar Program; the Physics Division, National Center for Theoretical Sciences of Taiwan; the National Aeronautics and Space Administration (NASA, Fermi Guest Investigator grant 80NSSC20K1567, NASA Astrophysics Theory Program grant 80NSSC20K0527, NASA NuSTAR award 80NSSC20K0645); NASA Hubble Fellowship grant HST-HF2-51431.001-A awarded by the Space Telescope Science Institute, which is operated by the Association of Universities for Research in Astronomy, Inc., for NASA, under contract NAS5-26555; the National Institute of Natural Sciences (NINS) of Japan; the National Key Research and Development Program of China (grant 2016YFA0400704, 2017YFA0402703, 2016YFA0400702); the National Science Foundation (NSF, grants AST-0096454, AST-0352953, AST-0521233, AST-0705062, AST-0905844, AST-0922984, AST-1126433, AST-1140030, DGE-1144085, AST-1207704, AST-1207730, AST-1207752, MRI-1228509, OPP-1248097, AST-1310896, AST-1440254, AST-1555365, AST-1614868, AST-1615796, AST-1715061, AST-1716327, AST-1716536, OISE-1743747, AST-1816420, AST-1935980, AST-2034306); NSF Astronomy and Astrophysics Postdoctoral Fellowship (AST-1903847); the Natural Science Foundation of China (grants 11650110427, 10625314, 11721303, 11725312, 11873028, 11933007, 11991052, 11991053, 12192220, 12192223); the Natural Sciences and Engineering Research Council of Canada (NSERC, including a Discovery Grant and the NSERC Alexander Graham Bell Canada Graduate Scholarships-Doctoral Program); the National Youth Thousand Talents Program of China; the National Research Foundation of Korea (the Global PhD Fellowship Grant: grants NRF-2015H1A2A1033752, the Korea Research Fellowship Program: NRF-2015H1D3A1066561, Brain Pool Program: 2019H1D3A1A01102564, Basic Research Support Grant 2019R1F1A1059721, 2021R1A6A3A01086420, 2022R1C1C1005255); Netherlands Research School for Astronomy (NOVA) Virtual Institute of Accretion (VIA) postdoctoral fellowships; Onsala Space Observatory (OSO) national infrastructure, for the provisioning of its facilities/observational support (OSO receives funding through the Swedish Research Council under grant 2017-00648); the Perimeter Institute for Theoretical Physics (research at Perimeter Institute is supported by the Government of Canada through the Department of Innovation, Science and Economic Development and by the Province of Ontario through the Ministry of Research, Innovation and Science); the Spanish Ministerio de Ciencia e Innovación (grants PGC2018-098915-B-C21, AYA2016-80889-P, PID2019-108995GB-C21, PID2020-117404GB-C21); the University of Pretoria for financial aid in the provision of the new Cluster Server nodes and SuperMicro (USA) for a SEEDING GRANT approved towards these nodes in 2020; the Shanghai Pilot Program for Basic Research, Chinese Academy of Science, Shanghai Branch (JCYJ-SHFY-2021-013); the State Agency for Research of the Spanish MCIU through the "Center of Excellence Severo Ochoa" award for the Instituto de Astrofísica de Andalucía (SEV-2017-0709); the Spinoza Prize SPI 78-409; the South African Research Chairs Initiative, through the South African Radio Astronomy Observatory (SARAO, grant ID 77948), which is a facility of the National Research Foundation (NRF), an agency of the Department of Science and Innovation (DSI) of South Africa; the Toray Science Foundation; Swedish Research Council (VR); the US Department of Energy (USDOE) through the Los Alamos National Laboratory (operated by Triad National Security, LLC, for the National Nuclear Security Administration of the USDOE (Contract 89233218CNA000001); and the YCAA Prize Postdoctoral Fellowship.

We thank the staff at the participating observatories, correlation centers, and institutions for their enthusiastic support. This paper makes use of the following ALMA data: ADS/JAO.ALMA#2016.1.01154.V. ALMA is a partnership of the European Southern Observatory (ESO; Europe, representing its member states), NSF, and National Institutes of Natural Sciences of Japan, together with National Research Council (Canada), Ministry of Science and Technology (MOST; Taiwan), Academia Sinica Institute of Astronomy and Astrophysics (ASIAA; Taiwan), and Korea Astronomy and Space Science Institute (KASI; Republic of Korea), in cooperation with the Republic of Chile. The Joint ALMA Observatory is operated by ESO, Associated Universities, Inc. (AUI)/NRAO, and the National Astronomical Observatory of Japan (NAOJ). The NRAO is a facility of the NSF operated under cooperative agreement by AUI. This research used resources of the Oak Ridge Leadership Computing Facility at the Oak Ridge National Laboratory, which is supported by the Office of Science of the U.S. Department of Energy under Contract No. DE-AC05-00OR22725. We also thank the Center for Computational Astrophysics, National Astronomical Observatory of Japan. The computing cluster of Shanghai VLBI correlator supported by the Special Fund for Astronomy from the Ministry of Finance in China is acknowledged.

APEX is a collaboration between the Max-Planck-Institut für Radioastronomie (Germany), ESO, and the Onsala Space Observatory (Sweden). The SMA is a joint project between the SAO and ASIAA and is funded by the Smithsonian Institution and the Academia Sinica. The JCMT is operated by the East Asian Observatory on behalf of the NAOJ, ASIAA, and KASI, as well as the Ministry of Finance of China, Chinese Academy of Sciences, and the National Key Research and Development Program (No. 2017YFA0402700) of China and Natural Science Foundation of China grant 11873028. Additional funding support for the JCMT is provided by the Science and Technologies Facility Council (UK) and participating universities in the UK and Canada. The LMT is a project operated by the Instituto Nacional de Astrófisica, Óptica, y Electrónica (Mexico) and the University of Massachusetts at Amherst (USA). The IRAM 30-m telescope on Pico Veleta, Spain is operated by IRAM and supported by CNRS (Centre National de la Recherche Scientifique, France), MPG (Max-Planck-Gesellschaft, Germany) and IGN (Instituto Geográfico Nacional, Spain). The SMT is operated by the Arizona Radio Observatory, a part of the Steward Observatory of the University of Arizona, with financial support of operations from the State of Arizona and financial support for instrumentation development from the NSF. Support for SPT participation in the EHT is provided by the National Science Foundation through award OPP-1852617 to the University of Chicago. Partial support is also provided by the Kavli Institute of Cosmological Physics at the University of Chicago. The SPT hydrogen maser was provided on loan from the GLT, courtesy of ASIAA.

This work used the Extreme Science and Engineering Discovery Environment (XSEDE), supported by NSF grant ACI-1548562, and CyVerse, supported by NSF grants DBI-0735191, DBI-1265383, and DBI-1743442. XSEDE Stampede2 resource at TACC was allocated through TG-AST170024 and TG-AST080026N. XSEDE JetStream resource at PTI and TACC was allocated through AST170028. This research is part of the Frontera computing project at the Texas Advanced Computing Center through the Frontera Large-Scale Community Partnerships allocation AST20023. Frontera is made possible by National Science Foundation award OAC-1818253. This research was carried out using resources provided by the Open Science Grid, which is supported by the National Science Foundation and the U.S. Department of Energy Office of Science. Additional work used ABACUS2.0, which is part of the eScience center at Southern Denmark University. Simulations were also performed on the SuperMUC cluster at the LRZ in Garching, on the LOEWE cluster in CSC in Frankfurt, on the HazelHen cluster at the HLRS in Stuttgart, and on the Pi2.0 and Siyuan Mark-I at Shanghai Jiao Tong University. The computer resources of the Finnish IT Center for Science (CSC) and the Finnish Computing Competence Infrastructure (FCCI) project are acknowledged. This research was enabled in part by support provided by Compute Ontario (http://computeontario.ca), Calcul Quebec (http://www.calculquebec.ca) and Compute Canada (http://www.computecanada.ca).

The EHTC has received generous donations of FPGA chips from Xilinx Inc., under the Xilinx University Program. The EHTC has benefited from technology shared under open-source license by the Collaboration for Astronomy Signal Processing and Electronics Research (CASPER). The EHT project is grateful to T4Science and Microsemi for their assistance with Hydrogen Masers. This research has made use of NASA's Astrophysics Data System. We gratefully acknowledge the support provided by the extended staff of the ALMA, both from the inception of the ALMA Phasing Project through the observational campaigns of 2017 and 2018. We would like to thank A. Deller and W. Brisken for EHT-specific support with the use of DiFX. We thank Martin Shepherd for the addition of extra features in the Difmap software that were used for the CLEAN imaging results presented in this paper. We acknowledge the significance that Maunakea, where the SMA and JCMT EHT stations are located, has for the indigenous Hawaiian people. IMV acknowledges the use of LLuis Vives HPC resources of the University of Valencia.

Facility: EHT.

Software: `DIFMAP` (Shepherd et al. 1995; Shepherd 1997, 2011), `eht-imaging` (Chael et al. 2016, 2018, 2022), ehtplot, `SMILI` (Akiyama et al. 2017a, 2017b; Moriyama et al. 2022), THEMIS (Broderick et al. 2020a), `VIDA` (Tiede et al. 2022), numpy (Harris et al. 2020), scipy (Virtanen et al. 2020), matplotlib (Hunter 2007), pandas (McKinney 2010; The pandas development team 2020), astropy (Astropy Collaboration et al. 2013, 2018).

Appendix A
Estimating Static Image Posteriors with THEMIS

A.1. The THEMIS Image Model

THEMIS is a general sampling-based parameter estimation framework developed for comparing parameterized models with the VLBI data produced by the EHT (Broderick et al. 2020a). Implemented within THEMIS are a wide variety of image models, ranging from phenomenological geometric models (Gaussians, rings, etc.) to physically motivated ray-traced radiative transfer models (e.g., semianalytic accretion flow models). Of relevance here is a set of splined raster models, described in detail in Broderick et al. (2020b) and applied to polarized reconstructions in M87* Paper VII. In these, the image reconstruction process is replaced with a model reconstruction problem in which the intensities at control points on a rectilinear raster grid are varied, with the final image produced at arbitrary locations via a cubic spline.

The image model presented in Broderick et al. (2020b) has a fixed FOV in the two cardinal directions. As described in M87* Paper VII, this restriction has been subsequently relaxed, with a more general set of models, adaptive splined rasters, that permit a rotation of the raster and a resizing of the FOV among its principal axes. In this way, not only can the brightness at each control point vary, but the locations of the control points themselves can also evolve. This results in a very flexible image model even when the dimension of the raster is small. The splined raster and adaptive splined raster models may be combined with any other THEMIS models, and typically large-scale features will be absorbed by a large-scale Gaussian component. The dimension of the underlying image model is, then, the sum of the number of control points, $N_x \times N_y$, two fields of view and the orientation of the raster, and the number of parameters associated with a potential geometric addition.

The THEMIS model has been fit to a variety of EHT data types. The bulk of the THEMIS-based analyses presented here employed the light-curve-normalized, LMT-calibrated complex visibilities directly. The residual complex station gains are reconstructed during each model evaluation and marginalized over via the Laplace approximation (see Section 6.8 of Broderick et al. 2020a). Lognormal priors are imposed on the station gain amplitudes with uncertainties that depend on the a priori calibration estimates (see Section 2.2). Network-calibrated sites (ALMA, APEX, JCMT, SMA) are assumed to have a lognormal 1σ uncertainty of 1%; following the LMT gain amplitude correction, it is assumed to have a residual lognormal 1σ uncertainty of 20%; and the remaining sites (PV, SMT, SPT) are assigned a lognormal 1σ uncertainty of 10%. In this way THEMIS fully explores the potential station gain space during its exploration of the underlying image space. Some early analyses made use of visibility amplitudes and closure phases. For these the station gain amplitudes were reconstructed in a similar fashion to that described above, though with a larger lognormal prior on LMT gain of 100% and 20% on all other stations.

A.2. Scattering and Variability Mitigation

Application of THEMIS-based imaging methods to Sgr A* is complicated by the presence of the confounding factors described in Section 3. Unless otherwise stated, diffractive scattering is mitigated via the scattering model from Johnson et al. (2018) directly to the model visibilities, i.e., instead of deblurring the data, the model is blurred. Refractive scattering and variability are mitigated via a scheme similar to that described in Section 3.1.2. Unlike the description there, for the THEMIS analyses, the additional noise terms are treated as parameterized contributions to the visibility uncertainties as described in detail in Georgiev et al. (2022).

Explicitly, the THEMIS analyses assume that the visibility uncertainties are described by

$$\sigma_j^2(\sigma_{\rm ref}, f, a, b, c, u_0) \\ = \sigma_{j,\rm th}^2 + \sigma_{\rm ref}^2 + f^2|V|^2 + \sigma_{\rm var}^2(a, b, c, u_0), \qquad \text{(A1)}$$

where $\sigma_{j,\rm th}$ is the intrinsic thermal uncertainty, $|V|$ is the measured visibility amplitude, and $\sigma_{\rm var}$ is given in Equation (2). Within this prescription, the $\sigma_{\rm ref}$ is conceptually identical to the `Const` approach to refractive scattering mitigation described in Section 3.1.2, with the exception that it is not fixed. Similarly, the fractional contribution $f|V|$ is conceptually identical to the systematic noise term, again with the sole distinction being to treat f as a free parameter.

A.3. Likelihood and Parameter Priors

For analyses that fit the visibility amplitudes and closure phases, the THEMIS log-likelihood is given by the appropriate combination of log-likelihoods from Sections 6.3 and 6.8 of Broderick et al. (2020a). For analyses that fit the full complex visibilities with the noise modeling, the log-likelihood is

$$\mathcal{L}(\boldsymbol{p}, \boldsymbol{q}) \\ = -\sum\nolimits_{\rm data}\left\{\frac{|\hat{V}_j - \hat{V}(\boldsymbol{u}_j; \boldsymbol{p})|^2}{2\sigma_j^2(\boldsymbol{q})} + \frac{1}{2}\ln[2\pi\sigma_j^2(\boldsymbol{q})]\right\}, \qquad \text{(A2)}$$

where $\{\hat{V}_j\}$ are the light-curve-normalized visibility data, $\boldsymbol{p}$ are the image-model parameters, and $\boldsymbol{q} = \{\sigma_{\rm ref}, f, a, b, c, u_0\}$ are the noise model parameters. The novel terms on the right-hand side are simply the σ-dependent normalization; while normally constant, in this instance they induce a penalty term that constrains the $\boldsymbol{q}$. When descattered, the diffractive scattering kernel is applied *to the model*, as opposed to deblurring the data, which maintains a consistent treatment of the "noise" model among the descattered and on-sky analyses.

Priors on each of the image-model parameters are listed in Table 6. In summary, uninformative logarithmic priors are assumed on the brightness at the control points, the raster size and orientation, and a potential shift from the correlation phase center. Similarly uninformative priors are imposed on the refractive scattering mitigation and systematic uncertainty terms of the noise model. In contrast, informed priors are imposed on the remaining parameters of the noise model, set by the pre-modeling considerations from Georgiev et al. (2022) and applied to Sgr A* in Paper IV. The relevant interquartile ranges are data set specific and are listed for the THEMIS analyses reported here in Table 2 for Sgr A* and the various synthetic data sets in Section 5.

A.4. Reconstructing the Posterior with THEMIS

THEMIS provides a number of sampling schemes with which to explore the likelihood surface. The bulk of the THEMIS-based analyses presented here employ a set of Markov Chain Monte Carlo (MCMC) samplers to explore the large-dimensional parameter space, $\{\boldsymbol{p}, \boldsymbol{q}\}$. To efficiently traverse the prior, identify multiple modes, and rapidly locate the global maximum, THEMIS makes use of parallel tempering, in which multiple, tempered copies of the likelihood, $\mathcal{L}_\beta = \beta\mathcal{L}$, are simultaneously explored; higher-"temperature" copies ($\beta \rightarrow 0$) become the reference distribution, which we take to be uniform in the prior bounds, while the bottom "temperature" ($\beta = 1$) is the posterior to be sampled. These are coupled via the deterministic even–odd swap tempering scheme (Syed et al. 2019), which efficiently moves information through the multiple, tempered levels. Periodically, the β are optimized to efficiently move information from the prior to the posterior following the scheme from Syed et al. (2019). Each individual tempering level is sampled via the Hamiltonian Monte Carlo sampling kernel from the Stan package (Carpenter et al. 2017).

Convergence is assessed via chain statistics, such as integrated autocorrelation time, approximate split-$\hat{R}$ tests, parameter rank distributions, and visual inspection. Reconstruction quality is determined by inspection of the best-fit sample's residuals and "reasonableness" of the associated image and gain reconstructions. Pathological solutions are uncommon and are typically indicative of poor sampler initialization and/or errors in the input. The number of tempering levels is chosen to exceed the global communication barrier Λ (Syed et al. 2019), typically near 20, and is run for 5×10^4–10^5 MCMC steps per tempering level.

Appendix B
Refractive Noise Levels Anticipated for EHT Data

To assess the effects of refractive scattering on our EHT measurements, we use the `stochastic optics` module implemented in the `eht-imaging` library (Chael et al. 2016; Johnson 2016). The `stochastic optics` allows the simulation of scattering realizations for a given intrinsic image and generation of the corresponding synthetic data sets. Here, we focus only on the refractive noise that would affect our imaging, i.e., the substructures on the scattered image. The other effects—centroid shift due to the position wander or total flux modulation—do not affect the image reconstruction of data calibrated by self-calibration and obtained from a single on-sky realization of scattering (Johnson et al. 2018).

The refractive noise level at each (u, v)-coordinate is determined by the standard deviation of the flux-normalized visibilities for all realizations, where the centroid of each realization is shifted to the phase center to mitigate the effects of position wander. We adopt a dipole model for the magnetic field wandering in the scattering screen (Johnson et al. 2018). Note that the refractive noise does not depend strongly on the choice of the model for field wander (Psaltis et al. 2018) for the source size anticipated from EHT data and scattering parameters constrained by Johnson et al. (2018).

We first compare the refractive effects for different combinations of the power-law spectral index α of the density fluctuation of the ionized plasma (see Section 3.1.1) and the inner scale of turbulence $r_{\rm in}$. Our refractive noise prescriptions `J18model1` and `J18model2` are derived with $\alpha = 1.38$ and $r_{\rm in} = 800$ km, which are the best-fit values in Johnson et al. (2018). These measurements have the uncertainties of $1.3 < \alpha < 1.5$ and $600\ {\rm km} < r_{\rm in} < 1500$ km (Johnson et al. 2018). Figure 29 shows an example gallery of scattered images and corresponding noise levels in the visibility domain for each combination of α and $r_{\rm in}$ in these ranges. The level of refractive substructure and the kernel size of diffractive angular broadening increase with α and $r_{\rm in}$ (Psaltis et al. 2018). Based on the results shown in Figure 29, we adopt a scaling factor of up to 2 to cover the cases of highest refractive noise level in the possible ranges of these two parameters.

Refractive noise is expected to also be dependent on the intrinsic source structure (e.g., Johnson & Narayan 2016). To assess this dependence, we estimate the refractive noise levels based on a circular Gaussian and the time-averaged images of the seven geometric models introduced in Section 5.1, for $\alpha = 1.38$ and $r_{\rm in} = 800$ km. As described in Section 5.1, these geometric models provide a broad consistency with the visibility amplitude profile of Sgr A* data. The size of the circular Gaussian is adjusted to have an FWHM of 45 μas, consistent with the effective FWHMs of the other seven geometric models estimated from their second moments. In Figure 30, we show the refractive noise levels for the different intrinsic source models. The refractive noise level is only a few percent of the total flux density regardless of the intrinsic source structures. The standard deviations across different geometric models are typically $\lesssim$0.4% of the total flux density.

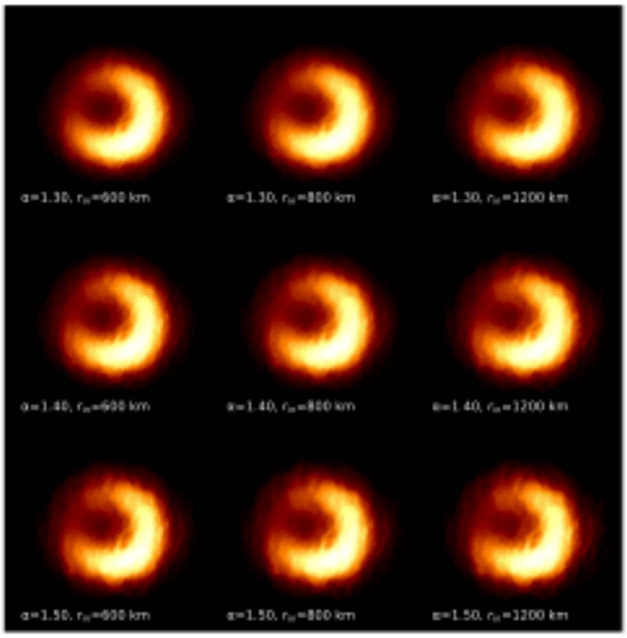

(a) On-sky images

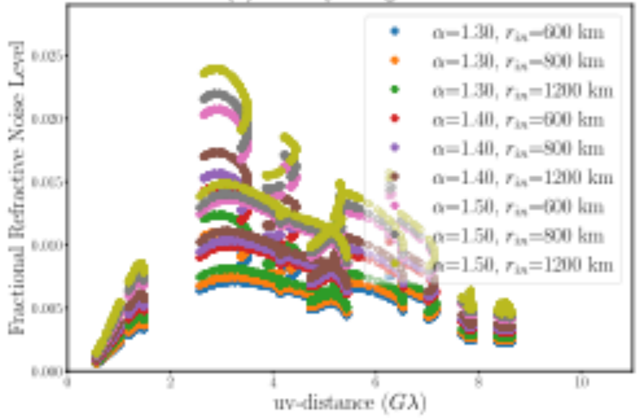

(b) Refractive noise levels

Figure 29. Dependence of refractive substructures on the power-law index α and inner scale of the turbulence $r_{\rm in}$. (a) Example realizations of the on-sky (i.e., scattered) images of the crescent model in Section 5. Each row shows a realization for a different power-law index α (1.3, 1.4, and 1.5), while each column shows a different $r_{\rm in}$ (600, 800, and 1200 km). (b) The corresponding levels of the flux-normalized refractive noise anticipated for (u, v)-coverage of April 7 Sgr A* data. The corresponding normalized visibility amplitudes are shown in Figure 3.

`J18model2` was derived by taking the mean of the refractive noise levels of seven geometric models. `J18model1`, on the other hand, is based on the refractive noise level of the circular Gaussian model. However, the circular Gaussian model has the lowest refractive noise level in most of the (u, v)-coverage of Sgr A* data, indicating that the

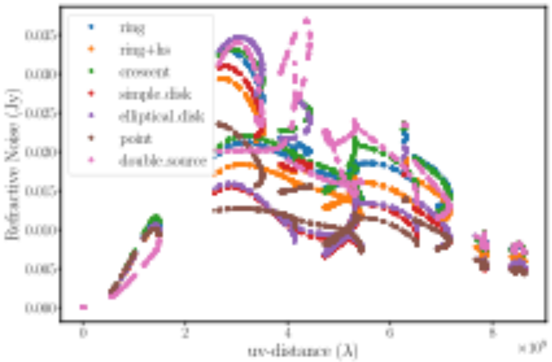

Figure 30. The levels of the flux-normalized refractive noises as a function of (u, v)-distance for different intrinsic structures. The refractive noise level is computed on (u, v)-coverage of April 7 Sgr A* data. The corresponding normalized visibility amplitudes are shown in Figure 3.

refractive noise level from the circular Gaussian model, if not scaled properly, may underestimate that of Sgr A* data. We derived a scaling factor to make the median of the χ^2 of all seven geometric models unity to minimize the effects of its systematically low refractive noise level.

Appendix C
First Sgr A* Images from Blind Imaging

Independently performed comparison between synthetic and real observational data can help to identify which image features are likely intrinsic and which are most likely spurious (see this approach in Bouman 2017 for synthetic data and in M87* Paper IV for observed EHT data of M87*).

To initiate the exploration of possible Sgr A* images while minimizing influence from collective bias, in our first stage of analysis we reconstructed images of Sgr A* in five independent teams. The teams were blind to each others' work and prohibited from discussing their imaging results. This procedure was similar to that done in M87* Paper IV for first images of M87*, with two notable differences. First, since the participants in all teams were already aware of problematic data from previous EHT imaging work, the team activities were not blind to previously identified problems in the data that could be affecting results. Second, as teams approached the date to submit results, it was made known to the organizers that teams would not be comfortable submitting only a single image or movie, and the instructions were changed to submit three representative images or movies per team.

No restrictions were imposed on the data preprocessing or imaging procedures used by each team. Teams 1 and 2 focused primarily on RML methods. Teams 3 and 4 focused primarily on CLEAN methods. Team 5 used a Bayesian method. All teams used an early-release engineering data set. While the reduction procedures and metadata corresponded to a preliminary version of the calibration pipeline, the data products were deemed mature enough for the blind imaging consistency test. The April 7 data set was selected for the first comparison, as it had the best (u, v)-coverage and a very stable light curve over the full observation (Wielgus et al. 2022).

Figure 31 shows images of the three representative submissions made by each team for Sgr A*. In cases where dynamic movie reconstructions of Sgr A* were submitted, we show the time-averaged image and indicate that the original submission was a movie. Although most submissions contain flux with a ∼50 μas separation, not all submissions contain a clear ring feature. Additionally, of the submissions that do contain a ring feature, the azimuthal flux distribution varies drastically. For example, Team 1 submitted three movies: one containing a ring with a PA of ∼30°, another containing a ring with a PA of ∼−70°, and the third containing no ring at all.

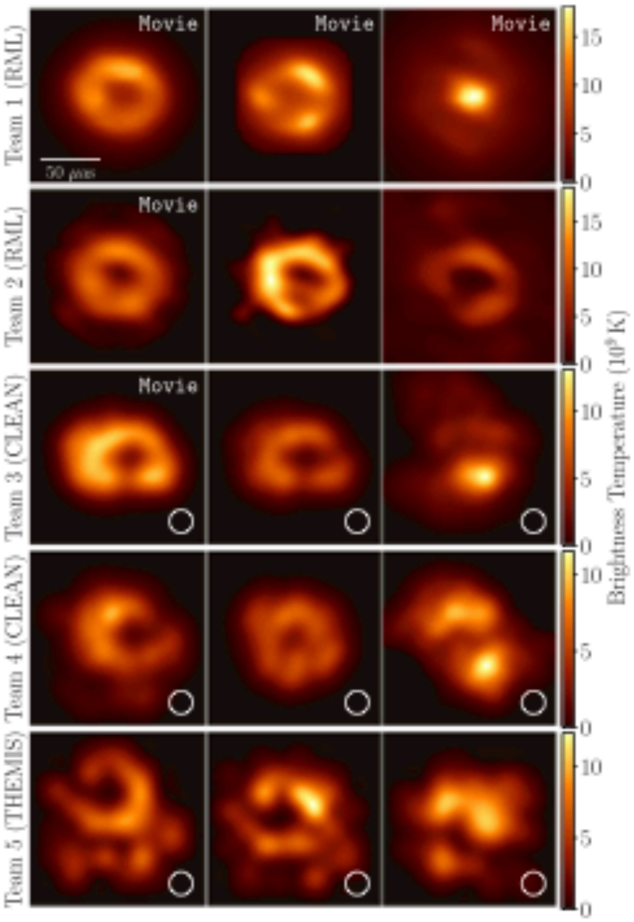

Figure 31. The first EHT images of Sgr A*, blindly reconstructed by five independent imaging teams using an early, engineering release of Stokes I data from the April 7 observations. Images from Teams 1 and 2 used RML methods (no restoring beam); images from Teams 3 and 4 used CLEAN (restored with a circular 20 μas beam, shown in the lower right corner); images from Team 5 used THEMIS. Each team shows three representative images from their reconstructions. Some images with the label "Movie" are time-averaged images of movie reconstructions. Many images show ring-like morphology with the diameter of ∼50 μas, while some reconstructions show non-ring-like morphology. The significant differences in brightness temperature between images are caused primarily by different assumptions regarding the total compact flux density (see Table 8) and also restoring beams applied only to CLEAN and THEMIS images.

This initial imaging stage indicated that a ∼50 μas feature was likely to exist in the image, but there is significant uncertainty in the presence of a ring structure, as well as the flux distribution around a possible ring structure. In Table 8, we show χ^2 values to closure phases ($\chi^2_{\rm CP}$) and log closure amplitudes ($\chi^2_{\rm logCA}$) for both engineering data used for imaging and science release data described in Section 2, as well as the compact total flux densities ($F_{\rm cpct}$). There are no significant differences seen in χ^2 values of images regardless of the presence of a ring structure and between different azimuthal

Table 8
Image Properties and Data Consistency Metrics for the First Sgr A* Images

		Team 1	Team 2	Team 3	Team 4	Team 5
Image Properties						
Method	Image ID	RML	RML	CLEAN	CLEAN	THEMIS
$F_{\rm cpct}$ (Jy)	1	2.37	2.07	1.90	1.64	1.59
	2	2.38	2.24	1.29	1.18	1.61
	3	2.38	1.99	1.25	0.69	1.73
Engineering Data (10 s avg., Stokes *I*, 0% sys. error)						
$\chi^2_{\rm CP}$	1	2.27 (1.85)	2.35 (1.75)	4.52 (4.20)	2.21	7.78
	2	2.30 (1.81)	2.08	2.51	3.31	6.79
	3	2.81 (1.80)	2.08	2.30	13.80	13.58
$\chi^2_{\rm log\,CA}$	1	3.44 (1.77)	4.67 (2.19)	2.76 (2.98)	2.06	5.90
	2	2.44 (2.07)	2.00	2.49	2.84	4.88
	3	4.73 (2.08)	6.44	2.93	1.91	4.95
Science Release (60 s avg., Stokes *I*, 0% sys. error)						
$\chi^2_{\rm CP}$	1	5.55 (2.53)	6.09 (1.96)	25.05 (21.77)	4.58	54.11
	2	6.08 (2.32)	3.89	7.27	12.11	45.09
	3	8.78 (2.31)	4.11	5.73	108.88	109.10
$\chi^2_{\rm log\,CA}$	1	7.12 (1.52)	10.75 (1.69)	8.31 (5.92)	2.79	24.22
	2	4.02 (1.46)	2.81	5.43	9.66	19.94
	3	6.47 (1.79)	16.95	8.21	7.45	10.01
Science Release (60 s avg., Stokes *I*, 10% sys. error)						
$\chi^2_{\rm CP}$	1	2.42 (1.33)	2.62 (1.18)	7.80 (6.92)	2.32	10.24
	2	2.41 (1.25)	2.09	2.85	5.93	8.02
	3	4.24 (1.17)	2.07	2.56	13.59	16.69
$\chi^2_{\rm log\,CA}$	1	3.36 (0.74)	4.73 (0.89)	3.98 (2.86)	1.32	10.70
	2	1.89 (0.76)	1.26	2.49	3.88	7.55
	3	3.57 (0.88)	6.88	3.72	3.59	4.66

Note. † $F_{\rm cpct}$, $\chi^2_{\rm CP}$, and $\chi^2_{\rm log\,CA}$ mean the compact total flux density of the VLBI scale images, χ^2 to closure phases, and log closure amplitudes, respectively. For movies, the values in the parentheses show χ^2 to the original movies, while the values outside of them show χ^2 to the time-averaged images.

intensity distributions of the ring structure. These ambiguous results motivated a series of systematic tests to identify whether source evolution (similar to that expected to be present in Sgr A*) could explain the multiple solutions recovered.

Appendix D
Imaging Pipelines

D.1. `DIFMAP` Pipeline

For this second stage of the imaging process we developed a scripted version of CLEAN in `DIFMAP` (version higher than `2.5k`), together with a Python wrapper used over the script, for carrying out an extensive parameter search. The initial manual CLEAN analysis (see Appendix C), together with the pre-imaging considerations (see Section 3), provided the set and range of parameters to be explored on both the synthetic data sets (described in Section 5) and the actual April 6 and 7 Sgr A* data, processed with both fringe-fitting pipelines HOPS and CASA, with high and low bands combined.

Prior to CLEAN imaging, the EHT data was preprocessed using the pre-imaging pipeline discussed previously. This includes intrasite normalization to the Sgr A* light curve; coherent averaging of the visibilities using 10 and 60 s; the inclusion of an additional systematic error by a factor of 0%, 2%, and 5%; and the scattering and noise mitigation prescriptions with the common parameters listed in Section 6.1 (see also Table 3).

The first step in the `DIFMAP` imaging process is the gridding of the visibilities in the (u, v)-plane, which was done by using two different approaches: uniform and natural weighting. The next step is to down-weight the data on all baselines to phased ALMA in the self-calibration process. As found for the case of M87 (M87* Paper IV), this prevents the ALMA baselines from dominating the phase and amplitude self-calibration process due to their significantly higher S/N. We have tested scaling factors for ALMA baseline weights during self-calibration of 0.1 and 0.5.

Atmospheric fluctuations at the short wavelength of 1.3 mm severely limit the S/N and the capability to reliably measure the visibility phases. We therefore rely on the closure phase measurements and the reconstruction of station phases using the Cornwell Wilkinson hybrid phase self-calibration approach. However, the self-calibration with the CLEAN model solely relies on the visibility phases and amplitudes, which forces an initial self-calibration of the phases (visibility amplitudes are much better constrained; Paper II), a process that is anchored on the more robustly measured closure phases.

To mitigate any possible bias in our choice for the initial model to self-calibrate the phases, and therefore to minimize the chances of reaching a local minimum in our manifold of image models, we have explored different initial models for the first phase self-calibration. The "fiducial" initial model has been chosen, based on the reduced-χ^2 of closure phases with the first reconstructed CLEAN model after the phase self-calibration with the initial model among three different types: a Gaussian with an FWHM of 15 μas (i.e., unresolved symmetric model), a uniform disk with a size ranging between 56 and 84

μas (in steps of 4 μas), and a uniform ring with sizes ranging between 36 and 68 μas (also in steps of 4 μas, no width).

A distinctive feature of CLEAN imaging is the use of masks (also known as cleaning windows) to define the area of the image to be cleaned. For this purpose we used a set of centered circular-disk-shaped CLEAN windows (i.e., with no hole in the middle to avoid any biasing).

The size of the cleaning windows should match the expected emission extent of the imaged source. To avoid introducing any prior bias, we have surveyed for a relatively large range of mask sizes, from 80 to 110 μas, which covers our prior Sgr A* image size constrains (Paper II). We note that, due to the limited (u, v)-coverage, larger masks ($\geqslant$100 μas) may pick up some emission from the main sidelobe of the interferometer, which may be particularly problematic for the point-source model given its diffuse emission, more difficult to recover with the CLEAN algorithm.

Contrary to the case of M87 (M87* Paper IV), we do not expect a large extended missing flux in Sgr A* (Paper II); hence, our CLEAN stopping criterion is based on setting a minimum threshold for the relative decrease in the rms of the residual image over the image noise estimated from the visibilities.

As a result, the total number of surveyed parameters has been 1680 for the on-sky data set and 6720 for descattered data. Note that the descattered results are based on a 4 times larger number of parameters owing to the scattering mitigation (i.e., refractive noise floor).

D.2. `eht-imaging` Pipeline

The `eht-imaging` software library implements the RML imaging technique described in Section 4.2. As an RML method, a successful image reconstruction is achieved when the proper hyperparameters balance the contribution of the selected data products and regularizers to the minimization of Equation (4). Thus, we designed a framework around our imaging pipeline to explore an extensive range of imaging and data pre-calibration parameters.

The pipeline preprocesses the input data following the procedure described in Section 6.1 as a first step. Only low- and high-band light-curve-normalized data sets were used for static imaging to minimize the effects of the source variability. We opted for an integration time of 60 s and explored all the nonclosing systematic error, scattering, and intraday variability noise budgets tabulated in Table 4. The algorithm is then initialized using a symmetric flat-disk image contained in a square-shaped grid of 80 × 80 pixels, which corresponds to an FOV of 150 μas. The disk diameter is surveyed as a parameter with values of 70, 80, and 90 μas. Note that, among the different imaging regularizers used in the pipeline, the maximum entropy regularizer (MEM) rewards similarity to a prior image, which in this case is assumed to be equal to the initialization image.

Full closure quantities and visibility amplitudes are used as data products. Contrary to M87*, the relative weighting of the visibility amplitudes adopted ranges from a smaller to an equally important contribution as closure quantities, since complex station gains were derived from calibrator sources beforehand (see Section 5.1.3 of Paper II). Several imaging regularizers and their relative weighting are employed to constrain the image properties, such as MEM, total variation (TV), and total squared variation (TSV), which enforce similarity to a prior image and/or smoothness over neighboring pixels, respectively.

Convergence to an optimal image that minimizes Equation (4) is then carried out in an iterative process in which the reconstructed image is blurred using a Gaussian kernel with the FWHM of the array nominal resolution (~24 μas), and then used as initialization for the next one to prevent the algorithm from being caught in local minima. In contrast to the M87* pipeline, no self-calibration was performed on the data, since the χ^2 statistics obtained for the output images of just one cycle of this iterative procedure were already good enough.

D.3. `SMILI` Pipeline

The `SMILI` imaging pipeline was designed to reconstruct images with RML imaging techniques utilizing three imaging regularizers: weighted-ℓ_1 (ℓ_1^w), TV, and TSV, similar to M87* Paper IV. Before the imaging process, both low- and high-band EHT data are preprocessed as described in Section 6.1. First, data are normalized by the time-dependent intrasite flux density and coherently time-averaged at an integration time of 120 s. The intrascan fluctuations in LMT baselines are corrected by self-calibrating the shortest VLBI baseline between SMT and LMT to a circular Gaussian with a total flux density of 1 Jy and an FWHM size of 60 μas. Finally, the pipeline applies the parameterized mitigation schemes for the nonclosing errors, scattering effects, and intraday variations as described in Section 6.1.

The pipeline reconstructs an image from preprocessed data at both low and high bands jointly with the FOV of 150 μas discretized by 2 μas pixels. Throughout the imaging, the pipeline adopts a prior image of a circular Gaussian with an FWHM size of 140, 160, or 180 μas for the ℓ_1 prior. The imaging process consists of a total of nine imaging cycles, including a single self-calibration of complex visibilities. Each imaging cycle performs 5000 iterations of the L-BFGS-B algorithm used for the gradient-descent optimization in the `SMILI`'s image solver.

In the first eight cycles of imaging, the images are reconstructed from visibility amplitudes, closure phases, and log closure amplitudes. To account for residual errors in the amplitude calibration, the fractional 5% and 30% uncertainties are added in quadrature to the errors of visibility amplitudes on non-LMT and LMT baselines, respectively. The first cycle starts with a circular disk image with a 70 μas diameter and a total flux of 1 Jy, while the later cycles subsequently adopt the image from the previous cycle as the initial image after recentering its center of mass and blurring with a 5 μas circular Gaussian.

After the eight cycles of imaging, complex visibilities are self-calibrated with its output image. Since the budgets of scattering and intraday variations are not fractional to visibility amplitudes, these two budgets will not be properly scaled with gains solved with a self-calibration. Therefore, to reflect these two budgets accurately on self-calibrated data, the `SMILI` pipeline updates these two budgets added to complex visibilities and closure quantities after self-calibration. Finally, the final image is reconstructed by a single imaging cycle using visibility amplitudes and closure quantities.

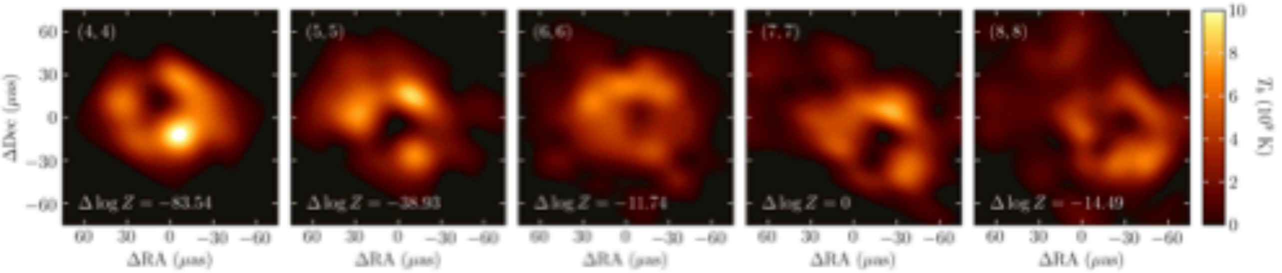

Figure 32. Mean images from the THEMIS posteriors for $(N_x, N_y) = (4, 4)$, (5, 5), (6, 6), (7, 7), and (8, 8) from left to right. In each panel the difference in the logarithm of the Bayesian evidence, $\Delta \log Z$, relative to the (7,7) model is listed in the lower left corner.

D.4. *THEMIS Raster Dimension Survey*

The sole hyperparameters in the THEMIS analyses not self-consistently explored during the construction of the posterior are the raster dimensions, N_x and N_y. While reasonable initial guesses may be made based on the diffraction limit, in practice we employ a data-driven method: comparing the Bayesian evidence (or appropriate proxies) of different dimensions (Broderick et al. 2020b).

Due to the computational expense of performing THEMIS posterior reconstructions, we limit the number of raster surveys performed to three: for the Sgr A* April 6 data, the Sgr A* April 7 data, and the GRMHD synthetic data set presented in Section 6.4.2. Of these, we present only that on the Sgr A* April 7 data here for brevity; surveys on the other data sets were conducted similarly. Furthermore, while we did experiment with $N_x \neq N_y$, given the apparent symmetry of the Sgr A* image, and not wishing to introduce any potential biases away from symmetry in the model specification, we restrict ourselves here to square rasters, i.e., $N_x = N_y$.

Five individual analyses were performed on the April 7, combined high- and low-band complex visibility data[163] as described in Appendix A, differing in the raster dimensions: $(N_x, N_y) = (4, 4)$, (5, 5), (6, 6), (7, 7), and (8, 8). For each, after convergence, the Bayesian evidence, Z, was computed via thermodynamic integration across tempering levels (Lartillot & Philippe 2006). Mean images from each analysis and the relative Bayesian evidence are shown in Figure 32.

For raster resolutions that are too small, the fit quality is poor. For raster resolutions that are too large, the added model complexity is not justified by the fit improvement. Importantly, by selecting on $\log Z$, we avoid potential complications associated with the modifications of the likelihood due to noise modeling, correlations between the high- and low-band gains, and non-Gaussianity of the posterior.

As roughly anticipated by the diffraction limit, the preferred raster size is (7, 7), which we adopt henceforth. This is accompanied by a convergence of the image structure for raster dimensions of (5, 5) and larger. Smaller and larger raster dimensions are overwhelmingly disfavored. Nevertheless, by (4, 4) the locations of the knots are identified, though the model misspecification prevents a faithful recovery of their relative brightness.

An identical procedure applied to the Sgr A* April 6 data finds that a smaller (6, 6) raster is preferred, ostensibly due to the smaller data volume. Similarly, when applied to the GRMHD synthetic data set in Section 6.4.2, a raster dimension of (6, 6) is again preferred, possibly due to the competition between the simplicity of the ring structure.

Appendix E
Top Set Selection

E.1. *The Effect of Relaxation in ρ_{NX} Criteria*

As discussed in Section 6.2, we relaxed the normalized cross-correlation criteria for each image by multiplying the value of $\rho_{\rm NX}$ obtained for $\alpha = 24$ μas beam by a relaxation factor of 0.95. This relaxation factor allows us to recover a large enough number of Top Set parameters for evolving synthetic data with Sgr A* (u, v)-coverage. This contrasts with the Top Set selection for M87 (M87* Paper IV), where no relaxation factor was considered. The necessity of the relaxation factor originates from the fact that temporal variations of the source structure cause a loss in the image fidelity of the reconstructions.

To ensure that this relaxed criterion is still able to distinguish different morphologies, we show the Top Set images with the worst (i.e., lowest) $\rho_{\rm NX}$ for each geometric model in Figure 33. Each descattered or on-sky reconstruction in Figure 33 shows the image that has the worst $\rho_{\rm NX}$ among the Top Set images for April 7. These images still retain resemblance to the ground-truth morphology, demonstrating that Top Set selection with a relaxation factor of 0.95 is still capable of reconstructing the basic structures of synthetic images with varied morphologies.

E.2. *χ^2 Distribution of Sgr A* Images*

Although the Top Set selection described in Section 6.4.1 is sorely based on the image fidelity of the reconstructions from the synthetic data sets, Top Set images of Sgr A* provide reasonable fits to EHT measurements. In Figure 34, we show χ^2 distributions of all the Sgr A* images passing the $\rho_{\rm NX}$ criterion using synthetic data reconstructions. χ^2 values were computed for closure phases and log closure amplitudes formed from data after being averaged at 1 minute, based on the same definition as in M87* Paper IV. To account for nonclosing effects, refractive scattering, and time variability, we include 1% of the fractional errors and the representative budgets for scattering and temporal variability (see Sections 3.1 and 3.2), respectively—in particular, the `J18model1` refractive noise model and a variability model with parameters a=0.02, $u_0 = 2$, b=2.5, and $c = 2$ are used. As shown in Figure 34, most of the images have χ^2 less than unity, and all the images provide $\chi^2 < 2$, demonstrating that all Top Set images provide reasonable fits to the Sgr A* data within the anticipated deviations of time-variable on-sky images from its intrinsic time-averaged structure. Therefore, we adopt all the parameter

---

[163] A similar study was performed using only the low-band data with similar results.

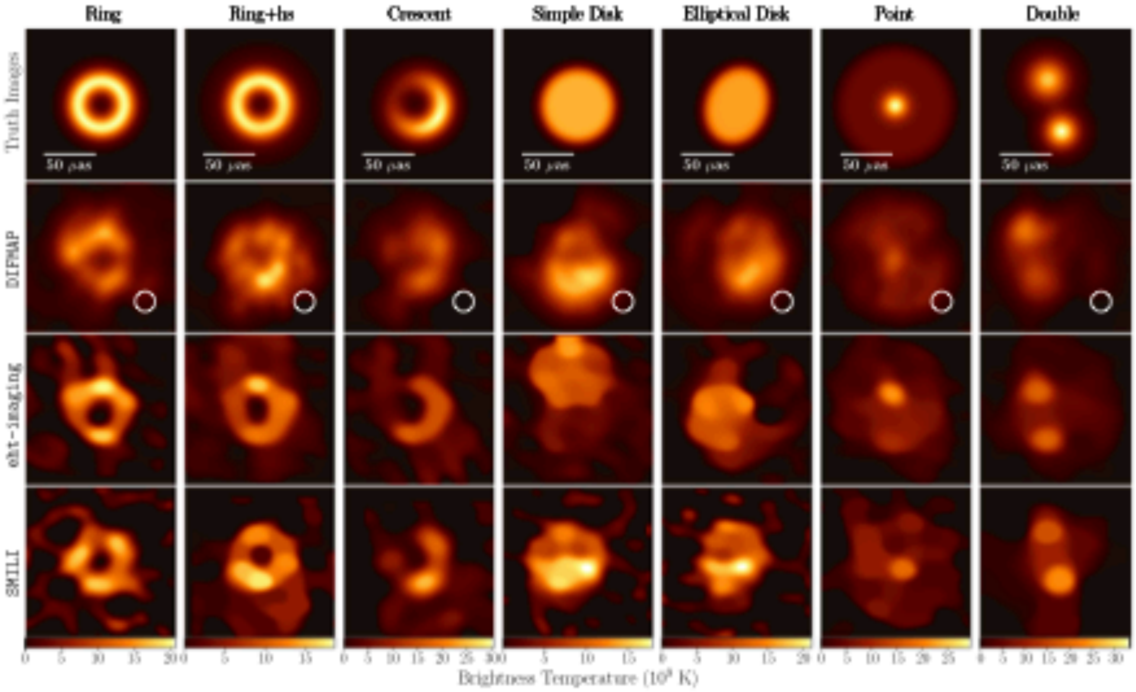

(a) Descattered reconstructions

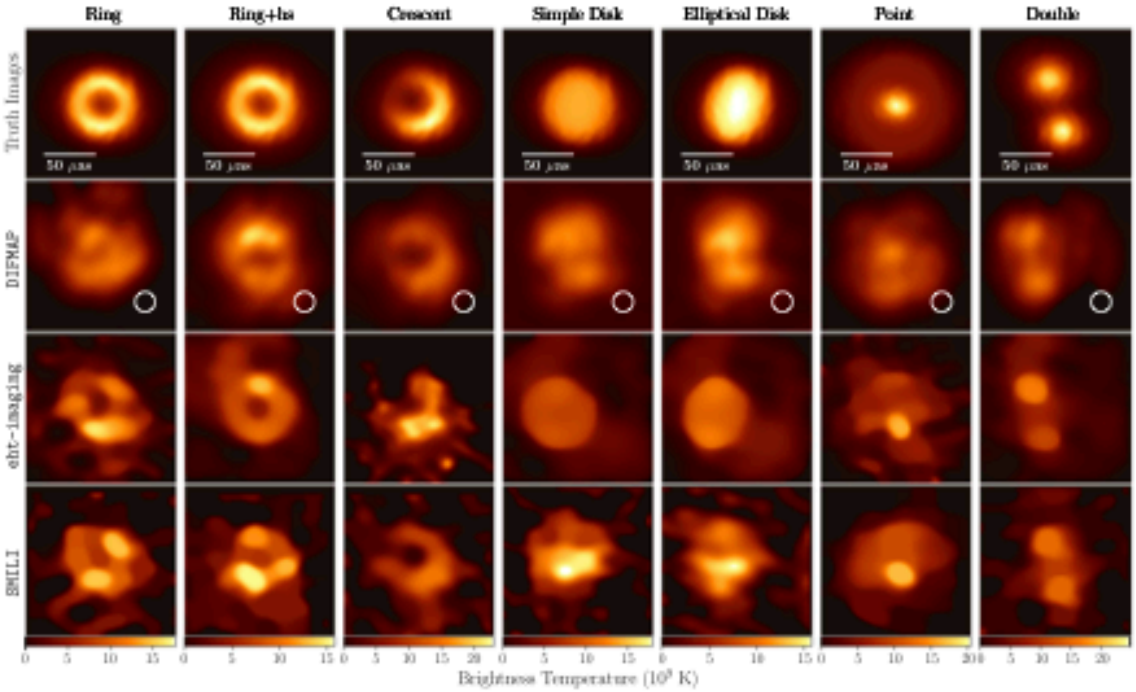

(b) On-sky reconstructions

Figure 33. The worst (i.e., lowest) $\rho_{\rm NX}$ images of synthetic geometric models among those reconstructed from the Top Sets of imaging parameters (a) with and (b) without scattering mitigation.

sets satisfying the $\rho_{\rm NX}$ criteria as the Top Sets without any cut by χ^2.

E.3. Top Sets of Imaging Parameters for April 6

In Section 6.2.2, we show the results of the Top Set selection for April 7 data. Here, we show the summary of Top Set parameters of each pipeline for April 6 data in Tables 9, 10, and 11, which are selected based on a method identical to that of April 7 data. Although the number of Top Set parameters for April 6 exceeds 100, this number is significantly smaller than the Top Set size identified for April 7 data. In particular, the number of Top Set parameters is reduced to 22% (`DIFMAP`), 25% (`eht-imaging`), and 11% (`SMILI`) of the April 7 Top Set size, as shown in Tables 3, 4, and 5. This significant reduction is most likely due to poor (u, v)-coverage on April 6.

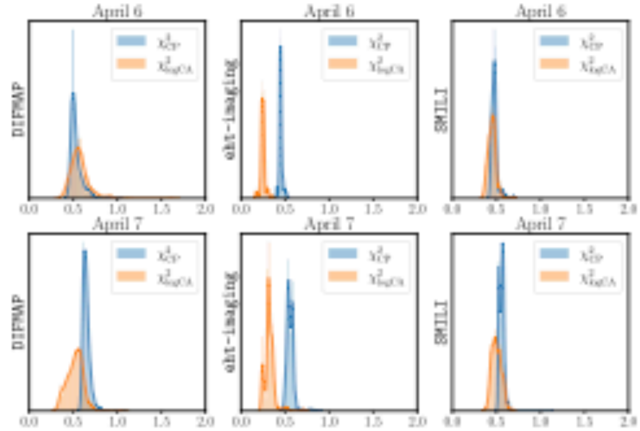

Figure 34. χ^2 distributions of the images from each pipeline and epoch that passed the $\rho_{\rm NX}$ criteria. χ^2 of closure phases and log closure amplitudes are shown in blue and orange, respectively. We assumed 1% systematic noise and representative variability noise for scattered images, and we also added refractive noise when calculating χ^2 of deblurred images.

Table 9
Parameters in the `DIFMAP` Pipeline Top Set on April 6

Apr. 6 (8,400 Param. Combinations; 365 in Top Set)							
Systematic error	0	0.02	0.05				
	15.6%	17.3%	67.1%				
Ref type	No	Const	2×Const	J18	2×J18		
	18.1%	23.0%	14.2%	24.1%	20.5%		
$a_{\rm psd}$	No	0.015	0.02	0.025			
	21.9%	26.8%	25.8%	25.5%			
$b_{\rm psd}$	No	1	3	5			
	21.9%	17.3%	24.4%	36.4%			
$\|u\|_0$	No	2					
	21.9%	78.1%					
Time average (s)	10	60					
	49.9%	50.1%					
ALMA weight	0.1	0.5					
	39.5%	60.5%					
UV weight	0	2					
	72.6%	27.4%					
Mask diameter (μas)	80	85	90	95	100	105	110
	10.7%	19.2%	36.2%	17.0%	6.0%	7.9%	3.0%

Note. In each row, the upper line shows the surveyed parameter value corresponding to the parameter of the left column, while the lower line shows the number fraction of each value in the Top Set. The total number of surveyed parameter combinations and Top Set are shown in the first row.

Table 10
Parameters in the `eht-imaging` Pipeline Top Set on April 6

Apr. 6 (112,320 Param. Combinations; 1,415 in Top Set)					
Systematic error	0	0.02	0.05		
	19.0%	39.7%	41.3%		
Ref type	No	Const	2×Const	J18	2×J18
	7.8%	29.2%	26.4%	17.0%	19.6%
$a_{\rm psd}$	No	0.015	0.02	0.025	
	13.0%	34.2%	29.4%	23.4%	
$b_{\rm psd}$	No	1	2	3	5
	13.0%	16.3%	25.4%	22.1%	23.1%
$\|u\|_0$	No	2			
	13.0%	87.0%			
TV	0	0.01	0.1	1	
	12.4%	27.8%	51.8%	8.0%	
TSV	0	0.01	0.1	1	
	29.0%	34.8%	35.8%	0.4%	
Prior size (μas)	70	80	90		
	15.3%	27.1%	57.6%		
MEM	0	0.01	0.1	1	
	3.4%	15.3%	77.9%	3.5%	
Amplitude weight	0	0.1	1		
	0%	4.2%	95.8%		

Note. Same as Table 9.

Table 11
Parameters in the `SMILI` Pipeline Top Set on April 6

April 6 (54,000 Param. Combinations; 292 in Top Set)					
Systematic error	0	0.02	0.05		
	34.2%	31.8%	33.9%		
Ref type	No	Const	2×Const	J18	2×J18
	7.9%	14.0%	18.8%	24.3%	34.9%
$a_{\rm psd}$	No	0.015	0.02	0.025	
	0.3%	23.3%	46.2%	30.1%	
$b_{\rm psd}$	No	1	2	3	5
	0.3%	28.8%	37.0%	28.1%	5.8%
$\|u\|_0$	No	1	2		
	0.3%	44.5%	55.1%		
TV	10^2	10^3	10^4	10^5	
	7.2%	92.5%	0.3%	0.0%	
TSV	10^2	10^3	10^4	10^5	
	41.4%	58.6%	0.0%	0.0%	
Prior size (μas)	140	160	180		
	31.5%	41.1%	27.4%		
ℓ_1	0.1	1	10		
	99.7%	0.3%	0.0%		

Note. Same as Table 9.

Appendix F
Classification of Ring Images

As described in Sections 5.2 and 7.2, we categorize GRMHD and Sgr A* images into clusters of images that share similar morphologies. Clustering of images is performed separately for on-sky and descattered reconstructions from each pipeline.

Prior to clustering, the images are aligned with an iterative method described below. We first derive the averaged image of all images. Each image is then aligned to maximize the cross-correlation with the averaged image. After aligning all images, the averaged image is recomputed with the aligned ones and used to align each image again. We repeat this procedure to align each image for a total of three times, providing the convergence of the alignment. After the above relative alignments between images, all images are centered using the average image; the images are uniformly shifted with the same amount of positional offset to maximize the cross-correlation between the average image and the time-averaged image of `Simple Disk` model.

The clustering of images has two major steps: the identification of ring images and nonring images, and the clustering of the ring images by the peak PAs. The ranges of the peak PAs are described in Section 5.2 for the GRMHD model and in Section 7.2 for the Sgr A* reconstructions. The separation of ring and nonring images is based on two morphological criteria as described below.

First, we identify nonring images by the degree of the central depression seen in the image. We measure a typical brightness of the central region by taking the median of the intensity within a radius of 10 μas, defined by

$$I_c \equiv \underset{r<10, \theta\in[-\pi,\pi)}{\mathrm{median}} I(r, \theta), \tag{F1}$$

where $I(r, \theta)$ denotes the intensity at the radius of r in μas and the PA of θ in radians. To measure the degree of the central depression, we compare the measured central brightness I_c with the maximum of the azimuthally averaged intensity at the outer area within a radius of 10–40 μas, given by

$$I_o \equiv \max_{r\in[10,40]} \left(\frac{1}{2\pi}\int_{-\pi}^{\pi} I(r, \theta) d\theta\right). \tag{F2}$$

We define the degree of the central depression by $f_{\rm cd} \equiv 1 - I_c/I_o$ and classify as nonring images those with $f_{\rm cd} < 0.2$ and $f_{\rm cd} < 0.15$ for descattered and on-sky reconstructions, respectively. The slightly lower threshold for on-sky images takes account of the angular broadening effects due to scattering, causing a systematic decrease in the central depression of a ring emission. This criterion can effectively distinguish point-like images from ring images.

The second criterion identifies nonring images by the smoothness of the azimuthal intensity distributions. To extract the azimuthal profile of the ridge intensity for the outer emission, we take the maximum intensity of the outer area within the radius of 10–40 μas for each PA, given by

$$I_p(\theta) \equiv \max_{r\in[10,40]} I(r, \theta). \tag{F3}$$

For each PA θ, we evaluate the difference between the ridge brightness $I_p(\theta)$ and the central brightness I_c normalized by the maximum intensity of the outer area defined by

$$f_p(\theta) \equiv \frac{I_p(\theta) - I_c}{\max_{\theta\in[-\pi,\pi)} I_p(\theta)}. \tag{F4}$$

Here $f_p(\theta)$ allows us to assess whether the azimuthal distribution of the outer area has a dark gap area comparable to or lower than the central depression. We identify a continuous dark area with $f_p(\theta) < 0.2$ and $f_p(\theta) < 0.15$ over a range of PAs broader than 70° as a gap in the azimuthal intensity distribution of descattered and on-sky reconstructions, respectively. If an image has more than two distinct gaps separated by >70°, we classify it as a nonring image with two or more distinct blobs not smoothly connected with each other. We also classify an image as a nonring one with an incomplete ring if it does not have a continuous bright area without any gaps over the range of PAs less than 180° (i.e., not completing more than a half circle). The above criteria effectively exclude multiple blob or highly corrupted ring-like images.

The morphological criteria discussed above provide a classification of ring and nonring images that is broadly consistent with human perception. However, as noted in Section 6.4.2, the classification of images that are borderline between ring and nonring classification is sensitive to the exact criteria used. Therefore, ring definitions that make use of slightly different criteria can lead to classification that still largely aligns with human perception but varies in the ring classification percentages quoted in this paper. In this work, motivated by method interpretability, we chose to make use of the simplest classification criteria that still largely aligned with human perception.

Appendix G
Validation of Static Imaging Results with Full-track Dynamic Imaging

As described in Section 3.2, the temporal variation of Sgr A* is anticipated to cause significant deviations of visibilities from those of the time-averaged morphology, of which levels can be well characterized by a broken power-law model. As described in Section 7.5.3, the variability noise model allows us to enhance the overall fidelity of synthetic data reconstructions and enable more sets of the imaging parameter combinations to be selected as Top Sets. However, the prescription for the temporal variability in Section 3.2 includes some simplifications of its characteristic properties: for instance, the circular symmetry assumed for the levels of the variability amplitudes in Fourier space and no inclusion of the correlated variations considered in data metrics as covariant components. Here, to assess the dependence of the mitigation scheme for temporal variability, we show the time-averaged images identified by full-track dynamic imaging not relying on the variability noise model. We emphasize that the goal of this section is not to characterize the dynamic evolution of Sgr A* on short timescales, which is the primary focus of Section 9.

As shown in Figure 35, we find the primary three ring morphologies identified in Section 7 with similar azimuthal variations in most of the Top Set images, while nonring structures are also reconstructed in a small fraction of Top Sets. The results are broadly consistent with those from the imaging survey presented in Section 7 and strongly indicate that our results described in Section 7 are resilient to the methods to

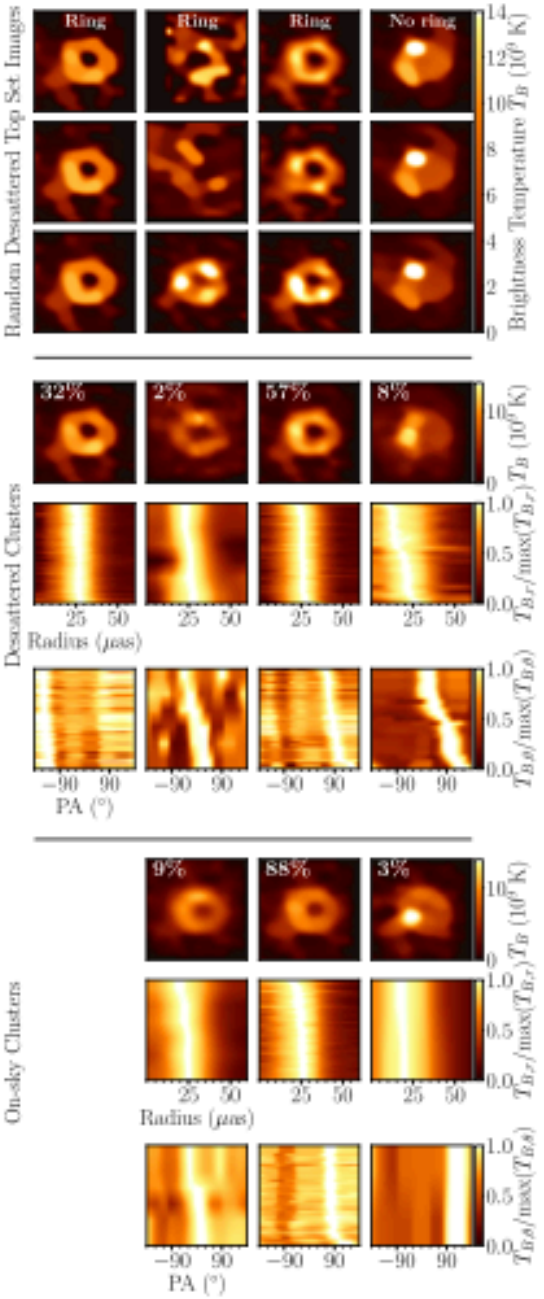

Figure 35. The distribution of Sgr A* Top Set images on April 7 reconstructed with the `SMILI` dynamic imaging pipeline. We show the distribution of images for each cluster in the same convention as in Figure 14 with three horizontal panels separated by horizontal lines. The top panel shows individual images randomly sampled from different clusters. The middle and bottom panels visualize the distributions of reconstructed descattered and on-sky Sgr A* images for each cluster, respectively. In each panel, from top to bottom, we show the average of each cluster, the distributions of the radial profiles, and the distributions of azimuthal intensity profiles.

recover the time-averaged morphology. We briefly describe the imaging process in Appendix G.1 and the results in Appendix G.2.

G.1. `SMILI` Dynamic Imaging Pipeline and Top Set Selections

Similar to the RML and CLEAN parameter surveys described in Section 6.2, we conducted a large imaging survey with RML dynamic imaging methods (see Section 4.4) implemented in a scripted pipeline using `SMILI`. The survey was performed on all seven geometric models and Sgr A* data.

Table 12
Parameters in the `SMILI` Dynamic Pipeline Top Set on April 7

Apr. 7 (7,776 Param. Combinations; 345 in Top Set)				
Systematic error	0 32.8%	0.02 35.4%		0.05 31.9%
Ref type	No 18.8%			J18model1 81.2%
TV	10^2 9.0%	10^3 22.0%	10^4 69.0%	10^5 0%
TSV	10^2 32.2%	10^3 44.6%	10^4 23.2%	10^5 0%
ℓ_1	0.1 11.9%	1 88.1%		10 0%
Prior size (μas)	140 29.6%	160 36.5%		180 33.9%
R_t	10^4 39.7%	10^5 24.1%		10^6 36.2%
R_i	10^4 14.2%	10^5 40.9%		10^6 44.9%

Note. In each row, the upper line shows the surveyed parameter value corresponding to the parameter of the left column, while the lower line shows the number fraction of each value in the Top Set. The total number of surveyed parameter combinations and Top Set are shown in the first row.

After completing the common pre-imaging process of data (Section 6.1), the pipeline reconstructs the time-averaged images on ∼8000 sets of the imaging parameter combinations across a broad parameter space, as outlined in Table 12. With the exactly same criteria as described in Section 6.2, Top Sets of the imaging parameters are then selected based on the fidelity of the synthetic data reconstructions.

The `SMILI` dynamic imaging pipeline shares the same procedures with the `SMILI` static imaging pipeline described in Appendix D.3, except for a major difference. Instead of the variability noise model used in Section 6.2, we allow temporal variations on timescales of typical scan intervals—for each set of parameters, the pipeline reconstructs a movie with the frame interval of 1 hour and then time-averages the movie to obtain the resultant reconstruction of the time-averaged morphology. We utilize two temporal regularizers, denoted by R_t and R_i, enforcing the continuity of the frame-to-frame intensity variations and the continuity between each frame and time-averaged intensity distributions, respectively, based on the Euclidean distance between images (see Johnson et al. 2017, for details). We note that here we only explore `J18model1` for the scattering mitigation, given consistency among the different scattering mitigation schemes (Section 7.5.2).

G.2. Results

As shown in Figure 35, Top Set images from the `SMILI` dynamic imaging pipeline can be categorized into four clusters shown in Section 7.2. Similar to the RML, CLEAN, and THEMIS static imaging pipelines, the ring morphology with the diameter of ∼50 μas was found as the dominant feature, while the nonring images were found in a small (∼5%) fraction of Top Sets. The differences in the image appearance between on-sky and descattered reconstructions are also consistent with Section 7.5.2; the on-sky reconstructions are blurrier than the descattered ones. We note that similar to Top Sets presented in Sections 5 and 7, here Top Set images from the `SMILI` dynamic imaging pipeline do not constitute a likelihood, and therefore the fractions should not represent our degree of certainty.

Appendix H
Reconstructions of a Best-bet GRMHD Model in Paper V

In Section 6, we utilize synthetic data based on a GRMHD model selected from a library of time-dependent GRMHD models presented in Paper V (see Section 5.2) to assess the performance

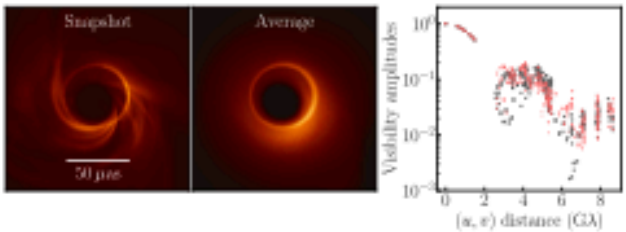

Figure 36. Image and visibility characteristics of the best-bet GRMHD models in Paper V (MAD, $a_* = 0.5$, $i = 30°$, $R_{\rm high} = 160$). The left two panels are the snapshot and averaged images of the ground-truth movie. The right panel shows the simulated visibility amplitudes (red) and real Sgr A* measurements (black) as a function of projected baseline length.

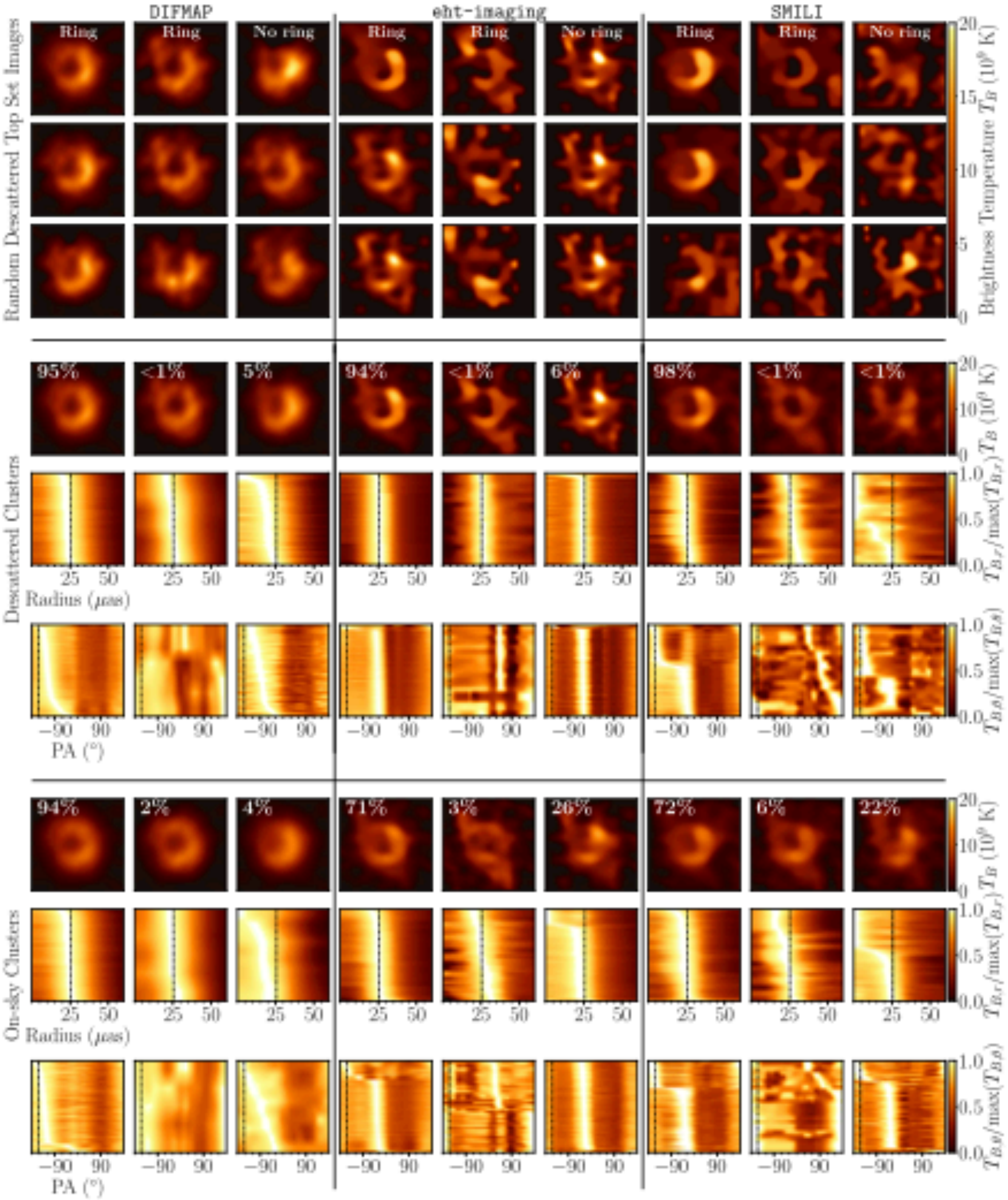

Figure 37. The distribution of reconstructed images with a best-bet GRMHD model identified in Paper V. The distribution of images from each pipeline for each cluster is shown with the same convention as in Figure 12.

of our imaging procedures on a physically motivated evolving source. While this GRMHD model is broadly consistent with our criteria in Section 5 based on 1.3 mm EHT data and light curves, it is not identified as a "best-bet" model in Paper V; "best-bet" models satisfy heterogeneous constraints derived from 1.3 mm EHT data, 86 GHz VLBI observations with the GMVA, 2.2 μm flux density, and X-ray luminosity. Paper V identifies three GRMHD models that lay in a "best-bet" region of strongly magnetized (MAD) models at low inclination with prograde spin.

Here we present example reconstructions of synthetic data derived from the "best-bet" model shown in Figure 16 of Paper V, with positive spin of $a_* = 0.5$ and electron temperature of $R_{\rm high} = 160$ viewed at $i = 30°$. In Figure 36, we show a snapshot and time-averaged images of this GRMHD model, as well as the amplitude versus (u, v)-distance corresponding to synthetic data generated with April 7 coverage (generated in the same manner as in Section 5). As shown in Figure 36, visibility amplitudes are broadly consistent with EHT Sgr A* data. Figure 37 shows descattered and on-sky images, which are reconstructed with `DIFMAP`, `eht-imaging`, and `SMILI` pipelines using their Top Set parameters and then further categorized by the same clustering method presented in Appendix F.

As shown in Figure 37, the distributions of the Top Set images share key results from those of the GRMHD reconstructions described in Section 6.4.2 (see also Figure 12). The vast majority of the reconstructions identify a ring morphology with a diameter of $\sim$50 μas, consistent with the ground-truth model. However, a small fraction of images have a nonring morphology. Furthermore, ring reconstructions have multiple azimuthal intensity modes. In particular, ring images that have a peak PA of $\sim -154°$ consistent with the ground-truth image do not appear as the most popular modes in `eht-imaging` and `SMILI` reconstructions. The broad consistency with the results in Section 6.4.2 suggests that our main results (e.g., that for the RML and CLEAN pipelines our methods produce a small fraction of nonring modes for an underlying ring model, and that the most popular mode reconstructed is not always that true mode) likely generalize across GRMHD models that are in a broad agreement with 1.3 mm EHT data.

Appendix I
Ring Fitting Parameters

In Tables 13 and 14 we list the diameter d, width w, PA η, asymmetry A, and fractional central brightness f_c measured from Top Set Sgr A* images for each identified cluster (see Section 8) corresponding to the descattered and on-sky images, respectively.

Table 13
Mean and Standard Deviation of Ring Parameters, Diameter d, width w, PA η, Asymmetry A, and Fractional Central Brightness f_c Measured from Top Set or Posterior Descattered Sgr A* Images for Each Cluster

		d (μas)	w (μas)	η (deg)	A	f_c
`DIFMAP`						
Apr. 6 Ring	`REx`	46 ± 4.1	33 ± 3.5	−100.6 ± 73.4	0.15 ± 0.08	0.47 ± 0.14
	`VIDA`	51 ± 3.1	33 ± 3.1	−108.3 ± 79.2	0.26 ± 0.12	0.46 ± 0.11
Apr. 7 Ring 1		50 ± 1.9	31 ± 2.7	−92.0 ± 42.0	0.06 ± 0.04	0.40 ± 0.08
		51 ± 1.3	33 ± 1.4	−82.7 ± 40.5	0.07 ± 0.07	0.37 ± 0.08
Apr. 7 Ring 2		49 ± 3.2	32 ± 2.9	−22.5 ± 54.4	0.08 ± 0.06	0.45 ± 0.12
		50 ± 1.7	32 ± 1.4	−27.0 ± 47.4	0.12 ± 0.11	0.42 ± 0.11
Apr. 7 Ring 3		49 ± 1.8	32 ± 2.9	20.5 ± 47.2	0.08 ± 0.05	0.44 ± 0.09
		51 ± 1.6	33 ± 1.8	5.3 ± 38.9	0.12 ± 0.10	0.41 ± 0.10
`eht-imaging`						
Apr. 6 Ring	`REx`	56 ± 4.5	24 ± 2.4	32.3 ± 86.4	0.17 ± 0.05	0.16 ± 0.14
	`VIDA`	59 ± 11.3	30 ± 10.4	70.0 ± 88.3	0.24 ± 0.14	0.23 ± 0.19
Apr. 7 Ring 1		55 ± 1.9	26 ± 2.3	−140.6 ± 62.9	0.11 ± 0.04	0.18 ± 0.08
		56 ± 5.4	27 ± 2.5	−156.0 ± 60.6	0.15 ± 0.13	0.18 ± 0.09
Apr. 7 Ring 2		53 ± 1.8	27 ± 2.7	−60.1 ± 35.8	0.12 ± 0.05	0.23 ± 0.10
		53 ± 3.6	27 ± 4.0	−71.7 ± 33.1	0.15 ± 0.11	0.22 ± 0.10
Apr. 7 Ring 3		55 ± 1.5	27 ± 3.0	170.4 ± 101.4	0.12 ± 0.07	0.31 ± 0.17
		57 ± 6.4	26 ± 4.5	179.7 ± 67.1	0.18 ± 0.21	0.27 ± 0.11
`SMILI`						
Apr. 6 Ring	`REx`	57 ± 3.4	24 ± 1.9	−27.7 ± 43.8	0.23 ± 0.09	0.03 ± 0.10
	`VIDA`	46 ± 12.0	50 ± 16.6	−71.6 ± 123.8	0.18 ± 0.12	0.59 ± 0.33
Apr. 7 Ring 1		52 ± 5.0	26 ± 2.0	151.9 ± 75.8	0.12 ± 0.04	0.22 ± 0.10
		52 ± 3.8	27 ± 3.9	175.9 ± 77.6	0.10 ± 0.08	0.22 ± 0.09
Apr. 7 Ring 2		53 ± 4.0	25 ± 2.9	−39.3 ± 51.2	0.13 ± 0.06	0.23 ± 0.11
		52 ± 6.2	29 ± 8.4	−59.2 ± 64.9	0.15 ± 0.12	0.27 ± 0.18
Apr. 7 Ring 3		51 ± 4.0	26 ± 1.9	109.1 ± 55.2	0.13 ± 0.04	0.19 ± 0.09
		51 ± 3.0	27 ± 3.8	116.2 ± 65.0	0.10 ± 0.08	0.19 ± 0.08
THEMIS						
April 6 Ring	`REx`	51 ± 3.9	25 ± 1.2	−128.6 ± 10.0	0.20 ± 0.04	0.27 ± 0.10
	`VIDA`	54 ± 0.9	24 ± 0.9	−121.0 ± 21.7	0.27 ± 0.06	0.34 ± 0.08
Apr. 7 Ring 1		53 ± 0.5	23 ± 1.4	−37.5 ± 11.3	0.14 ± 0.01	0.09 ± 0.07
		56 ± 1.4	27 ± 0.9	−37.6 ± 7.6	0.30 ± 0.05	0.19 ± 0.07
Apr. 7 Ring 2		53 ± 0.7	22 ± 0.5	−12.5 ± 8.3	0.21 ± 0.02	0.05 ± 0.05
		56 ± 1.2	27 ± 0.7	−20.6 ± 6.1	0.36 ± 0.04	0.15 ± 0.03
Apr. 7 Ring 3		⋯	⋯	⋯	⋯	⋯
		⋯	⋯	⋯	⋯	⋯

Table 14
Mean and Standard Deviation of Ring Parameters, Diameter d, width w, PA η, Asymmetry A, and Fractional Central Brightness f_c Measured from Top Set and Posterior On-sky Sgr A* Images for Each Cluster

		d (μas)	w (μas)	η (deg)	A	f_c
`DIFMAP`						
Apr. 6 Ring	`REx`	46 ± 3.0	34 ± 4.3	97.9 ± 88.9	0.11 ± 0.05	0.50 ± 0.15
	`VIDA`	47 ± 1.9	39 ± 3.4	94.8 ± 87.0	0.14 ± 0.07	0.56 ± 0.10
Apr. 7 Ring 1		47 ± 3.0	38 ± 2.7	-111.6 ± 39.7	0.06 ± 0.03	0.59 ± 0.07
		49 ± 2.2	37 ± 1.9	-99.9 ± 40.2	0.09 ± 0.06	0.58 ± 0.08
Apr. 7 Ring 2		48 ± 2.4	38 ± 2.6	31.3 ± 81.2	0.06 ± 0.04	0.58 ± 0.07
		49 ± 2.0	37 ± 2.1	16.0 ± 75.7	0.10 ± 0.06	0.56 ± 0.07
Apr. 7 Ring 3		48 ± 2.7	37 ± 2.9	40.4 ± 63.5	0.05 ± 0.03	0.57 ± 0.08
		50 ± 2.1	38 ± 1.9	27.6 ± 60.9	0.08 ± 0.06	0.55 ± 0.08
`eht-imaging`						
Apr. 6 Ring	`REx`	49 ± 3.9	28 ± 3.6	13.8 ± 123.8	0.15 ± 0.05	0.33 ± 0.15
	`VIDA`	50 ± 5.6	41 ± 6.7	110.8 ± 133.2	0.20 ± 0.10	0.55 ± 0.13
Apr. 7 Ring 1		51 ± 2.4	32 ± 2.7	-165.9 ± 45.0	0.08 ± 0.03	0.42 ± 0.10
		52 ± 4.5	35 ± 3.5	-170.7 ± 41.1	0.11 ± 0.10	0.41 ± 0.08
Apr. 7 Ring 2		50 ± 2.3	32 ± 2.7	-30.4 ± 68.1	0.07 ± 0.03	0.44 ± 0.07
		49 ± 2.6	35 ± 4.0	-71.6 ± 53.5	0.06 ± 0.08	0.42 ± 0.08
Apr. 7 Ring 3		49 ± 2.4	33 ± 3.3	161.6 ± 67.3	0.10 ± 0.02	0.50 ± 0.08
		53 ± 6.6	35 ± 7.5	173.3 ± 70.8	0.19 ± 0.14	0.52 ± 0.10
`SMILI`						
Apr. 6 Ring	`REx`	43 ± 0.4	28 ± 3.1	163.1 ± 10.1	0.10 ± 0.04	0.57 ± 0.01
	`VIDA`	39 ± 3.9	46 ± 8.8	-98.6 ± 93.3	0.17 ± 0.14	0.67 ± 0.16
Apr. 7 Ring 1		43 ± 4.9	33 ± 1.7	127.7 ± 29.9	0.09 ± 0.08	0.51 ± 0.07
		45 ± 1.8	34 ± 3.1	136.8 ± 36.8	0.07 ± 0.06	0.48 ± 0.07
Apr. 7 Ring 2		47 ± 4.5	33 ± 2.8	58.4 ± 57.5	0.10 ± 0.05	0.48 ± 0.11
		46 ± 5.2	37 ± 7.4	59.8 ± 81.7	0.08 ± 0.08	0.50 ± 0.13
Apr. 7 Ring 3		48 ± 4.3	32 ± 2.9	89.6 ± 34.9	0.11 ± 0.04	0.45 ± 0.14
		47 ± 3.5	35 ± 4.3	84.8 ± 48.2	0.11 ± 0.08	0.46 ± 0.11
THEMIS						
Apr. 6 Ring	`REx`	46 ± 2.1	30 ± 1.6	-139.4 ± 52.9	0.15 ± 0.05	0.34 ± 0.11
	`VIDA`	47 ± 3.1	33 ± 2.0	-127.4 ± 53.0	0.17 ± 0.08	0.42 ± 0.07
Apr. 7 Ring 1		51 ± 0.8	28 ± 1.3	-37.8 ± 53.6	0.15 ± 0.01	0.21 ± 0.10
		55 ± 1.6	32 ± 2.4	-41.4 ± 52.6	0.25 ± 0.05	0.30 ± 0.07
Apr. 7 Ring 2		50 ± 1.5	26 ± 1.1	-16.0 ± 8.9	0.21 ± 0.03	0.20 ± 0.08
		56 ± 2.6	32 ± 0.9	-25.2 ± 7.3	0.35 ± 0.03	0.29 ± 0.06
Apr. 7 Ring 3		...	...	...	...	...
		...	...	...	...	...

Appendix J
Dynamic Imaging and Snapshot Model Fitting Tests

J.1. Selection of Time Windows with the Best (u, v)-coverage

Farah et al. (2022) demonstrate that the changing (u, v)-coverage created by Earth's rotation during the aperture synthesis process leads to regions of time that produce dynamic reconstructions of varying quality. The quality of a short-timescale reconstruction is partially determined by the snapshot (u, v)-coverage geometry, which introduces certain artifacts during the imaging process.

The scale and severity of these artifacts can be predicted by quantitatively scoring the (u, v)-coverage as a function of time, which can be done in a number of ways. Some metrics examine how much of the Fourier plane is covered by an interferometer (e.g., Palumbo et al. 2019), while others look at gaps created by the sparse coverage (e.g., Wielgus et al. 2020). In addition to these metrics, Farah et al. (2022) derive a novel metric that probes both the anisotropy and radial homogeneity of the coverage.

By applying these metrics to the April 6 and 7 EHT (u, v)-coverage on Sgr A*, we can assess the scan-by-scan performance and identify regions of time that are likely to produce the best reconstructions, independent of the underlying source structure. The result of such an analysis for April 7 is shown in Figure 38, and two candidate regions are highlighted. The metrics predict that dynamic imaging reconstructions will have the highest quality in the region from 1.5 to 3.2 GMST (Region II); the reconstructions will produce substantially worse results in the region from 19.4 to 21 GMST (Region I). We validate this prediction by testing on high-S/N data in Farah et al. (2022) and show that Region II indeed allows for significantly better recovery of the source variability than Region I. Therefore, based only on the EHT's (u, v)-coverage, we focus on dynamic imaging/modeling Region II throughout Section 9.

J.2. StarWarps Temporal Regularizer Normalization

Temporal regularization in `StarWarps` is controlled by a parameter β_Q^{-1}. This parameter corresponds to the variance of the conditional distribution of pixel intensities for a given

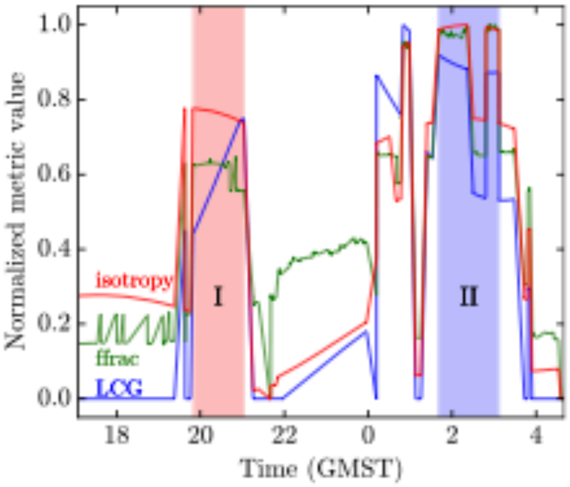

Figure 38. Normalized metric computations for every scan of the 2017 April 7 EHT coverage of Sgr A*. 0:00 GMST marks the day change from April 7 to April 8. Though the metrics have different considerations, all highlight the region (labeled "II") from ∼1:30 GMST to ∼3:10 GMST as a candidate region for dynamic imaging.

snapshot holding the previous snapshot fixed: $p(I_k|I_{k-1}) = \mathcal{N}(I_{k-1}, \beta_Q^{-1}\mathbf{I})$. The units of β_Q^{-1} are (Jy pixel^{-1})^2. In the main text, we consider values $\beta_Q^{-1} \in \{5 \times 10^{-4}, 5 \times 10^{-6}, 5 \times 10^{-8}\}$. Larger values of β_Q^{-1} correspond to less temporal regularization, as the conditional distribution $p(I_k|I_{k-1})$ becomes wider.

We can also interpret the values of β_Q^{-1} in visibility space. The Fourier transform of the image I_k is given by an $N_{\rm pix} \times N_{\rm pix}$ matrix $\boldsymbol{F}$:

$$V_k = \boldsymbol{F} I_k. \tag{J1}$$

In our convention, the pixel values in I_k have units Jy pixel^{-1}, so the entries of $\boldsymbol{F}$ are pure phase terms without a $1/\sqrt{N}$ normalization (so that, e.g., the zero-baseline visibility in Jy is just the sum of the pixel intensities). As a result, $\boldsymbol{F}\boldsymbol{F}^\dagger = N_{\rm pix}\mathbf{1}$. Because Equation (J1) is a linear transformation, $p(V_k|I_{k-1})$ is also a normal distribution, with a mean V_{k-1} and a covariance:

$$\boldsymbol{\Sigma} = \boldsymbol{F}[\beta_Q^{-1}\mathbf{I}]\boldsymbol{F}^\dagger = \beta_Q^{-1} N_{\rm pix}\mathbf{1}. \tag{J2}$$

Thus, $\sigma_{\rm vis} \equiv \sqrt{\beta_Q^{-1} N_{\rm pix}}$ is the standard deviation of a snapshot visibility measurement in `StarWarps`, holding the previous frame fixed.

In Figure 39, we compare this quantity to the measured EHT visibility amplitudes in the selected dynamic imaging window on April 11. The `StarWarps` movie reconstructions in the main text have $N_{\rm pix} = 40 \times 40 = 1600$. GRMHD simulations (see Paper IV and Georgiev et al. 2022) and the light curve of Sgr A* (see Wielgus et al. 2022) suggest that the variations on minute timescales should have a zero-baseline standard deviation of $\sigma_{\rm vis} \sim 10$ mJy. Thus, reconstructions with $\beta_Q^{-1} \sim 10^{-7}$(Jy pixel^{-1})^2 are expected to give variability that is consistent with what is measured in Sgr A*.

Larger values of β_Q^{-1} correspond to lower temporal regularization and allow for larger variations in the visibility amplitudes. For instance, our reconstructions in Section 9 with $\beta_Q^{-1} = 5 \times 10^{-6}$ permit somewhat more variability than is seen in simulations and observations of Sgr A*. Nevertheless, we have also found that allowing excess variability helps to trace evolution in tests on synthetic data from GRMHD simulations.

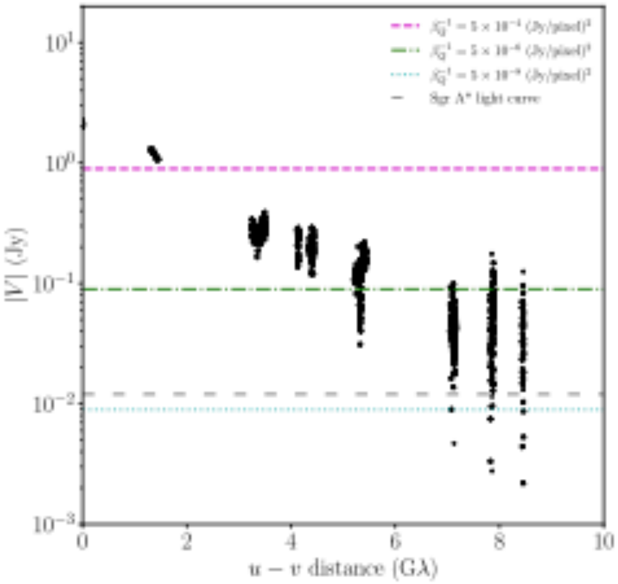

Figure 39. April 7 EHT visibility amplitudes over the selected window for dynamic imaging and modeling (black points). The horizontal lines show the expected standard deviation of the visibility amplitudes in `StarWarps` reconstructions for different values of β_Q^{-1} in units of (Jy pixel^{-1})^2: 5×10^{-4} (magenta), 5×10^{-6} (green), and 5×10^{-8} (cyan).

J.3. Testing (u, v)-coverage Effects

As discussed in Section 9.2, the geometry of the (*u*, *v*)-coverage can have an effect on the recovered image structure, especially in cases where the coverage is extremely sparse. To study the effects of (*u*, *v*)-coverage on dynamic fits to Sgr A* data, we perform a number of tests on synthetic data sets and study the effect of different (*u*, *v*) baselines on fits to the real data.

J3.1. Recovering the Position Angle of a Static Crescent

As most of our analysis of the dynamic structure of Sgr A* revolves around tracking the PA of brightness around the ring, it is important to assess our ability to recover the PA accurately in realistic synthetic data. To that end, we constructed synthetic EHT data sets from four static crescent models with peak brightness points rotated at 60° increments around the ring. The brightness ratio of each crescent model was chosen to roughly match the 1.5:1 ratio recovered from geometric model fitting to Sgr A* data. Figure 40 shows the imaging and geometric modeling results obtained by fitting to these synthetic data sets in the selected 1.7 hr region. Note that, for both approaches, the true PA is recovered as the primary mode for most of the crescents. The imaging methods contain temporal regularization, which likely makes it easier to recover a static underlying structure; however, the geometric modeling results do not assume any temporal regularization.

J3.2. Uniform Ring Synthetic Data

The interplay between the source size and sidelobes in the dirty beam pattern from sparse coverage can cause imaging artifacts that appear in the form of bright "knots" around ring sources. Computing the dirty image of an underlying uniform ring source reveals the location of these knots when using

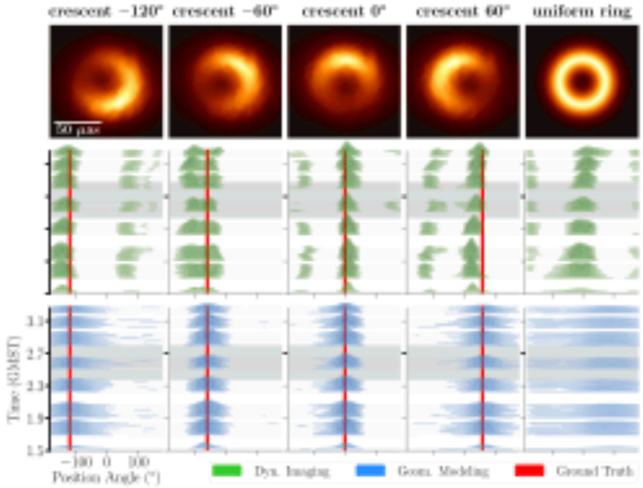

Figure 40. PA recovered from differently oriented static crescent synthetic data sets and a uniform ring synthetic data set, using both dynamic imaging (green) and geometric modeling (blue) techniques. The crescents' ground-truth PA is shown as a vertical red line. Imaging uses a prior image μ of a uniform ring convolved with a 25 μas beam.

calibrated visibilities. To assess the impact of these knot artifacts on our analysis, we performed imaging and geometric model fitting on data generated from a uniform ring (with no brightness changes in azimuth) with a diameter of 49 μas (refer to the uniform ring in Figure 7). As can be seen in Figure 40, both the imaging and modeling results indicate an image structure with a preferred PA—$\sim 0^\circ$ or $\sim 90^\circ$ for imaging and $\sim 100^\circ$ for modeling. However, the associated asymmetry of the recovered uniform ring is very low, a brightness ratio of less than 1.1:1 compared to 1.5:1 for Sgr A*. Thus, in combination with the results of Appendix J.3.1, we conclude that although the (u, v)-coverage will bias the PA in the limit of low image asymmetry, for the level of image asymmetry recovered in Sgr A* this bias should have a small effect.

J3.3. Baseline Test

In order to evaluate the contribution of each baseline to the recovered evolution in Sgr A*, we compared results obtained on data sets modified to remove a particular baseline. In particular, we compared the PA posteriors obtained using geometric modeling on 11 different data sets—10 data sets each with a single baseline removed and one complete data set. As can be seen in Figure 41, we find that most baselines do not heavily affect the trends we see on April 7. However, there are two baselines that appear to have a significant effect on the results: Chile–Hawai'i and LMT–Hawai'i. Without the Chile–Hawai'i baseline we are not able to discriminate between the northwest and southeast PA; without the LMT–Hawai'i baseline we do not recover as significant of a PA shift. Upon inspecting the (u, v)-coverage of these baselines, it becomes apparent that these two baselines probe the northwest–southeast orientations that we are interested in, and thus without them we are unable to properly discriminate between these two PA orientations. It is also worth noting that removal of the Chile-SPT baseline appears to "clean up" the modeling results, suggesting that small-scale features probed by this baseline may not be properly captured in our geometric model fits.

J.4. Testing Scattering Mitigation Strategies

In producing dynamic reconstructions and model fits of the Sgr A* data, the choice of scattering mitigation strategy is a potential source of uncertainty. We have explored the sensitivity of our dynamic imaging and snapshot model fitting results to the same five scattering mitigation strategies we consider in the static image surveys in Sections 6 and 7.5.2. Namely, we produce reconstructions and model fits to the unmodified data (i.e., on-sky with no descattering), as well as with visibilities deblurred by the Sgr A* diffractive scattering kernel and with the thermal noise error bars inflated by four models of the refractive noise: the `Const` model, the `J18model1` model, and then double the additional error tolerance from each of these models (2×`Const`, 2×`J18model1`). Based on the analysis done in Section 3.1, this selection is conservative and spans our uncertainty in Sgr A*'s refractive noise.

Figure 42 presents comparisons of the `StarWarps` reconstructions and snapshot model fitting results on the April 6 and 7 Sgr A* data with all five scattering mitigation strategies. We find that the general trends in the ring PA we discuss in Section 9.4 are not significantly changed by any of the five scattering mitigation strategies we explore for geometric modeling, although the PA posteriors are significantly broader (sometimes spanning a full 360°) when using the larger refractive noise budgets of 2×`Const` and 2×`J18model1`. In contrast, for imaging, on April 7 we observe a transition from positive to negative PA to be the most commonly recovered trend with all of the on-sky, `Const` and `J18model1` scattering mitigation strategies when using a ring prior. However, when we add a very large amount of refractive noise tolerance to the error bars in the 2×`Const` and 2×`J18model1` models, the PA becomes more stable over the observation window. This is due to the interplay of temporal regularization with an increased flexibility in fitting the data with a static model due to the expanded noise budget. In this figure, imaging with `StarWarps` makes use of the ring*25μas ring prior/initialization, and modeling with `DPI` uses a second-order m-ring ($m = 2$) model with a parameterized central Gaussian floor.

J.5. Testing the Effects of Different Imaging Priors and Model Specifications

As overviewed in Section 9.4.1, the recovered PA of the azimuthal brightness distribution in the ring-like morphology of Sgr A* is sensitive to the modeling choices made in both imaging and geometric modeling. In this section we go into further detail on some of the effects seen.

J5.1. Imaging

Temporal Regularization.—The level of continuity enforced between recovered frames is controlled by temporal regularization. In particular, `StarWarps` encourages frames to be similar by probabilistically modeling each frame I_k as being a sample from a normal distribution with mean I_{k-1} and covariance $\beta_Q^{-1}\mathbf{1}$ (see Equation (7)). Thus, decreasing the multiplier β_Q^{-1} will increase recovered continuity between frames. This is seen, as expected, in the recovered movies of Sgr A* visualized in Figure 28; recovered movies with low temporal regularization experience fast and drastic variability on large-scale features, while movies with high temporal regularization experience slow yet steady variability on large-scale features and absorb the remaining variability in the data with small-scale fluctuations. Due to the extreme sparsity of data on each snapshot, although these

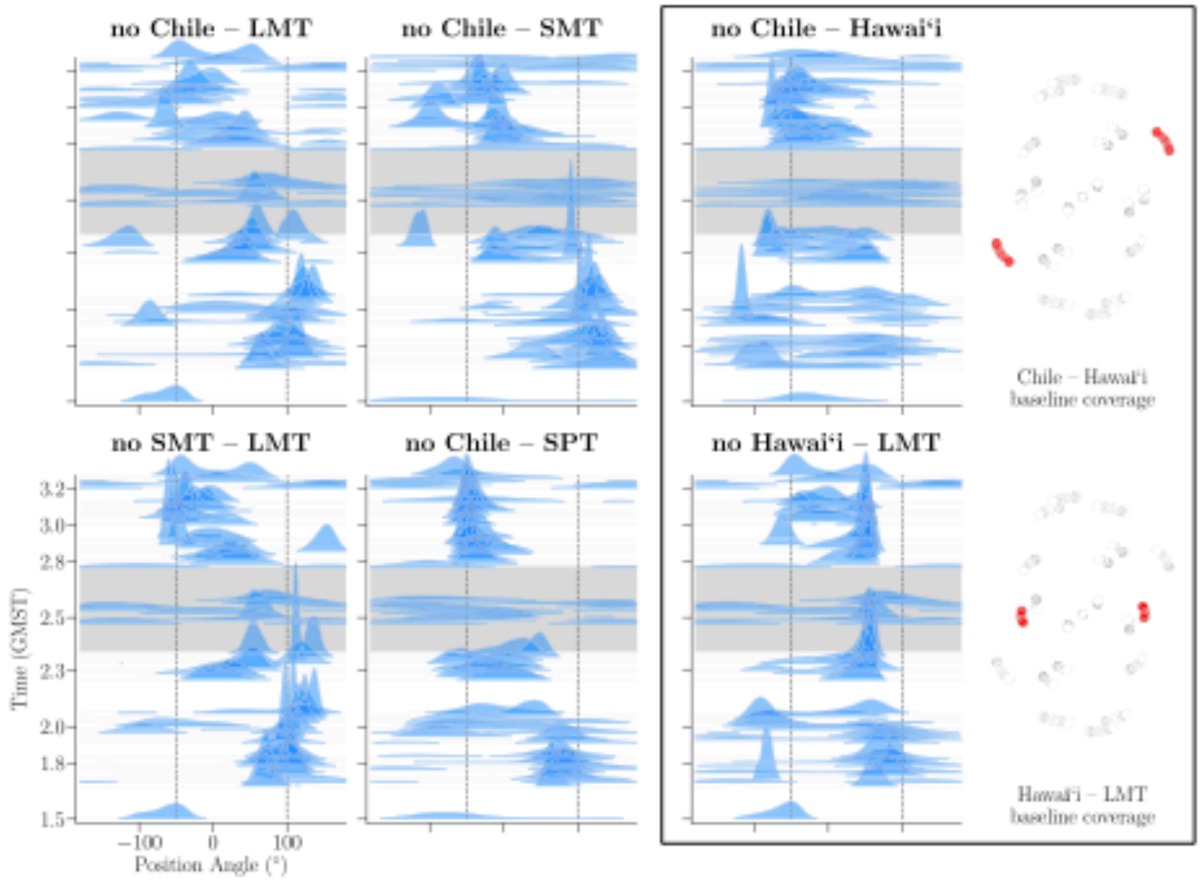

Figure 41. PA recovered using `DPI` geometric modeling after removal of a particular baseline from Sgr A* data on April 7. The flagged baseline appears in the title of each panel. The Chile–Hawai'i and Hawai'i-LMT baselines are highlighted, and their location in the (u, v)-plane is shown. These two baselines probe the east–west and southeast–northwest orientations.

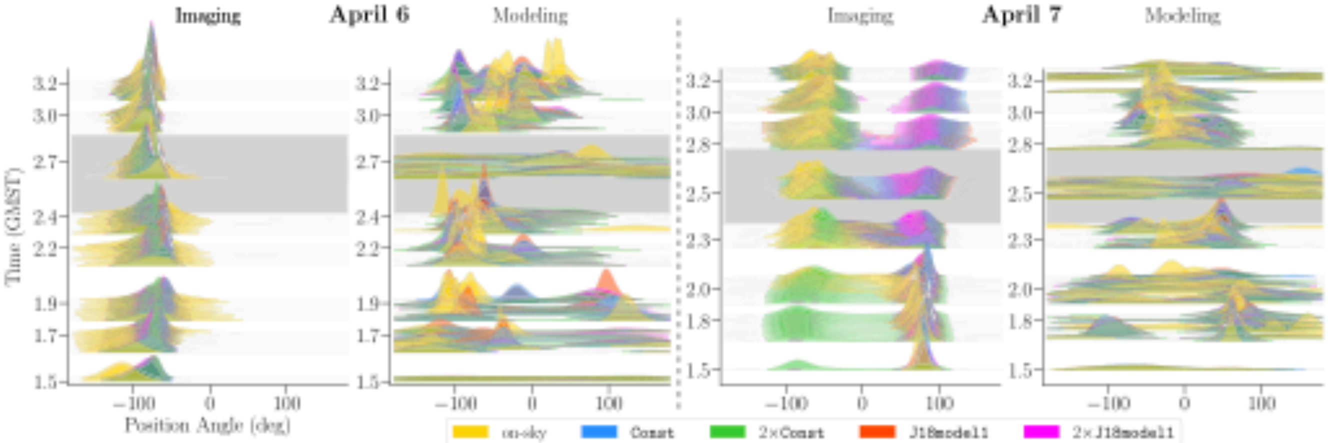

Figure 42. The PA recovered using dynamic imaging and geometric modeling techniques under different scattering mitigation assumptions. These range from no scattering mitigation whatsoever (yellow) to different amounts of refractive noise added to the deblurred data: a constant noise floor (blue), the refractive noise model `J18model1` (red), and these two scaled by a factor of two (green and magenta, respectively). Imaging results were obtained using an initialization/prior image of a uniform ring blurred with a Gaussian kernel with FWHM of 25 μas. Modeling results were obtained from the `DPI` pipeline using the *m*-ring 2 geometric model. The gray band at roughly 2.6 GMST indicates the region where the LMT has dropped out and data coverage is poorer.

movies contain significantly different levels of recovered variability, they all fit the data in terms of χ^2 fairly well. The only substantial difference between data fits can be seen when inspecting the SMT–LMT–Hawai'i closure triangle. It is worth noting that the positive-to-negative flip on the April 7 closure triangle is not reproduced by the recovered video with high temporal regularization. Nonetheless, since all movies still match all remaining baselines indistinguishably well, it is difficult to form any solid conclusions on the type of variability in Sgr A* based on this one closure triangle.

`StarWarps` *Spatial Prior Images*.—To explore the sensitivity of results to the ring features encouraged during imaging,

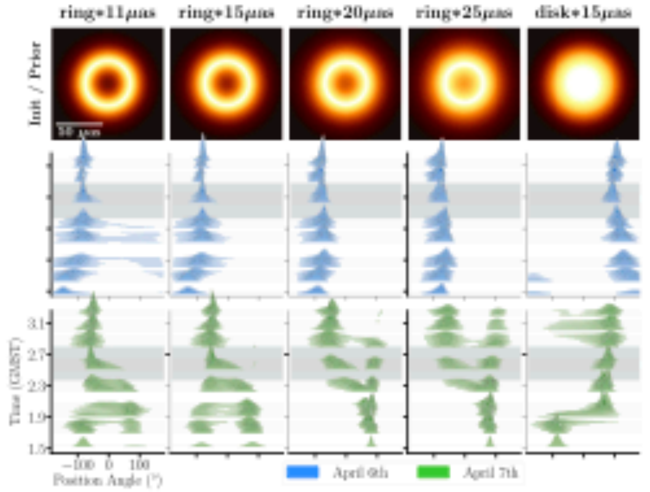

Figure 43. PA reconstructed using `StarWarps` under different init/prior assumptions for both April 6 (blue) and 7 (green). These include uniform rings with increasing Gaussian blurring and a uniform disk with no central brightness depression.

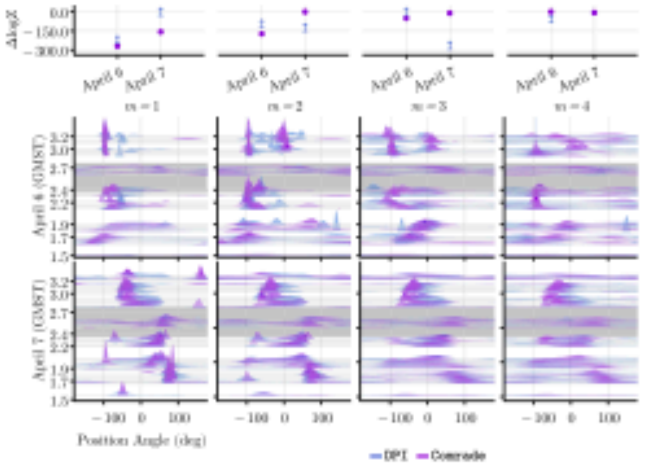

Figure 45. Comparing the *m*-ring results across orders 1, 2, 3, and 4 in both `Comrade` (magenta) and `DPI` (blue). The impact of the different *m*-ring orders on the PA evolution for April 6 and is shown in the middle and bottom rows. The top row is the change in the log-evidence across *m*-ring orders and days. The evidence lower bound produced by `DPI` is shown as a blue upward-pointing arrow.

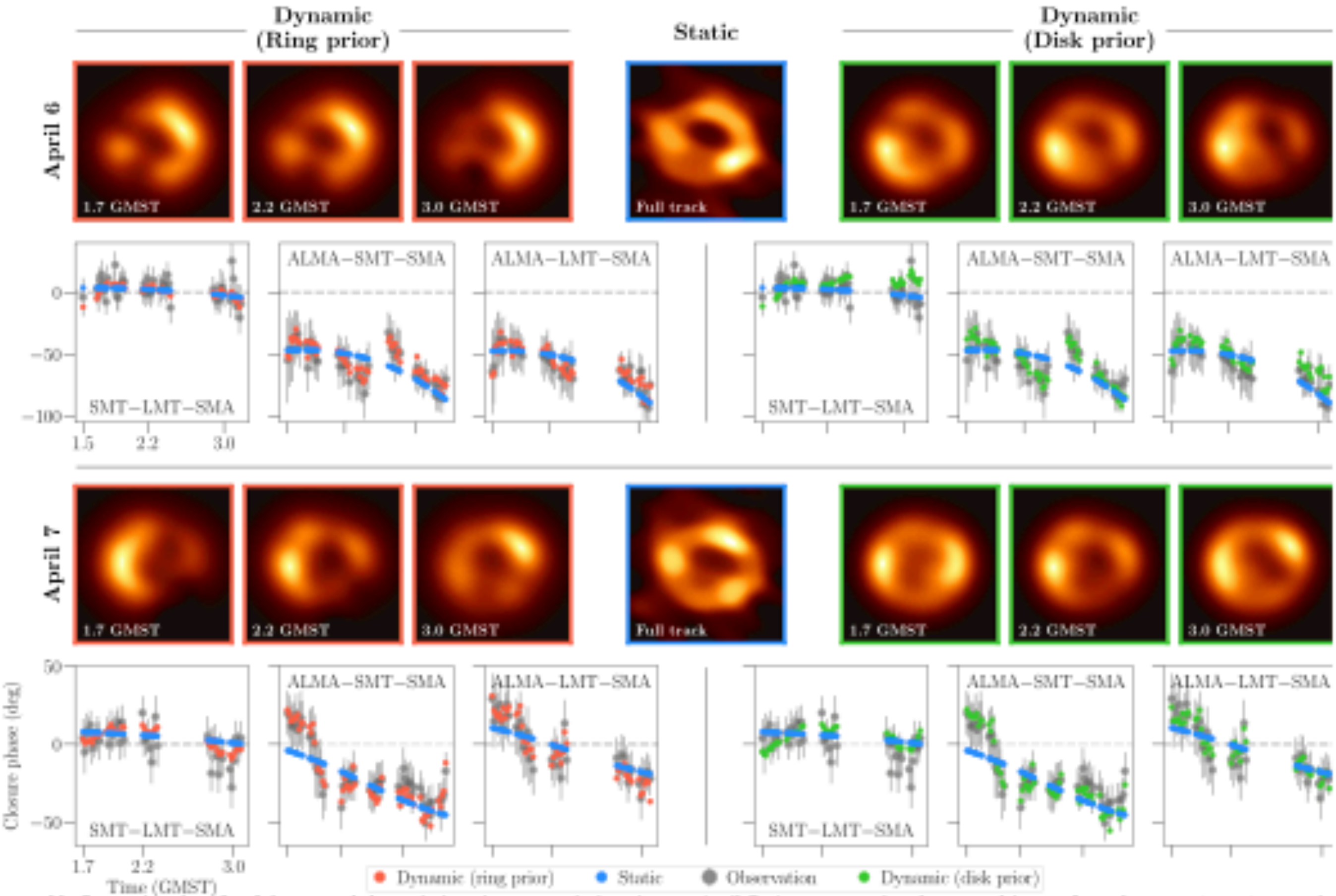

Figure 44. Comparing data fit of descattered dynamic imaging vs. static imaging on April 7. A representative descattered image from the `eht-imaging` static imaging pipeline is shown. In the selected closure plots below the measured data (60 s avg. without a variability noise budget) are shown overlaid with the corresponding closure phases.

we introduce five different images used as both the initialization and mean prior image μ in `StarWarps`. Figure 43 shows the mean prior images explored for imaging the original data and deblurred data. Note that recovered flux is constrained to evolve within the regions that have flux in the prior image; therefore, the puffier rings and the tapered disk with more extended flux are less constraining during imaging. As expected, movies recovered with the less constraining puffier prior images result in recovered movies with less clear underlying ring structures. Nonetheless, in all these cases (with a ring init/prior), the same general trend in PA is recovered in one of the modes, even when the central indent is very weak. When a disk prior is used with no central indent whatsoever, the same PA trend is not recovered; instead, the PA trend appears to be reversed in sign (as discussed in Figure 27). Figure 44 shows more detailed comparisons of `StarWarps` movies reconstructed with ring and disk mean prior images on April 6 and 7, including data fits to representative closure phases.

J5.2. Geometric Modeling

For snapshot geometric modeling, we have two competing effects. One is that we require a geometric model that can adequately explain the on-sky image. However, given the sparseness of the (u, v)-coverage for each snapshot, the risk of overfitting the data is considerable and potentially leads to artificially uninformative posteriors. However, underfitting the data can lead to large biases in the recovered parameters and artificially narrow posteriors. To find the preferred model, we use relative measures. That is, we do not compare the absolute fit quality using a metric like the χ^2 statistic, but rather how well a model does compared to the others considered. For this purpose we use the Bayesian evidence (also referred to as evidence),

$$Z(\text{data}|M) = \int \mathcal{L}(\text{data}|\theta, M)p(\theta|M)d\theta. \tag{J3}$$

The evidence measures the marginal probability of the data, after averaging over all possible parameter values of the model. The preferred model is then the one that maximizes the evidence of the model. For snapshot modeling we select the preferred model by computing the log-evidence in each snapshot and then sum the log-evidence across all snapshots. Note that we are only able to estimate the evidence for the `Comrade` pipeline. `DPI`/variational inference cannot estimate the evidence, but instead can compute an effective lower bound to use as a proxy.

M-ring Order.—To assess the impact of different model choices on the posterior samples, we considered an m-ring model with one to four modes. The results for the m-ring model from the `Comrade` pipeline are shown in Figure 45. We find that the trend for the dipole moment phase is consistent across model specifications, although the posteriors become more uncertain for the higher-order m-ring models. The recovered total evidence for each model is shown in Figure 45. For April 6 $m = 4$ is the preferred model with a log-evidence of 1499. On April 7, the $m = 2$ m-ring is preferred with a log-evidence of 1667. On both days the overall trend of the PA remains stable for $m = 1$, 2, 3, but the distributions become noticeably wider.

For the `DPI` pipeline we find similar PA trends for April 6 and 7. Using the evidence lower bound that is calculated as part of variational methods, $m = 3$ is preferred on April 6 and $m = 1$ on April 7. Furthermore, on April 7 the PA posterior for $m = 3$, 4 is very broad, becoming essentially unconstrained.

Comparing the `DPI` results to `Comrade`, we find that $m = 1$ is preferred on April 7 and $m = 3$ on April 6 according to the evidence lower bound. `DPI` fits closure products that are equivalent to placing uniform priors on gains, meaning that the data are less constraining. Therefore, it is not surprising that `DPI` prefers simpler models compared to `Comrade`. To select a fiducial model across days and bands, we considered the evidence, the relative impact on the posterior, and the impact on each pipeline. For these reasons we take $m = 2$ for `DPI` and $m = 2$ and sometimes $m = 3$ for `Comrade`. The $m = 2$ model is preferred for `Comrade` on April 7, and the $m = 2$ distribution for `DPI` is similar to but broader than the $m = 1$ distribution.

ORCID iDs

Kazunori Akiyama https://orcid.org/0000-0002-9475-4254
Antxon Alberdi https://orcid.org/0000-0002-9371-1033
Juan Carlos Algaba https://orcid.org/0000-0001-6993-1696
Richard Anantua https://orcid.org/0000-0003-3457-7660
Keiichi Asada https://orcid.org/0000-0001-6988-8763
Rebecca Azulay https://orcid.org/0000-0002-2200-5393
Uwe Bach https://orcid.org/0000-0002-7722-8412
Anne-Kathrin Baczko https://orcid.org/0000-0003-3090-3975
Mislav Baloković https://orcid.org/0000-0003-0476-6647
John Barrett https://orcid.org/0000-0002-9290-0764
Michi Bauböck https://orcid.org/0000-0002-5518-2812
Bradford A. Benson https://orcid.org/0000-0002-5108-6823
Lindy Blackburn https://orcid.org/0000-0002-9030-642X
Raymond Blundell https://orcid.org/0000-0002-5929-5857
Katherine L. Bouman https://orcid.org/0000-0003-0077-4367
Geoffrey C. Bower https://orcid.org/0000-0003-4056-9982
Hope Boyce https://orcid.org/0000-0002-6530-5783
Christiaan D. Brinkerink https://orcid.org/0000-0002-2322-0749
Roger Brissenden https://orcid.org/0000-0002-2556-0894
Silke Britzen https://orcid.org/0000-0001-9240-6734
Avery E. Broderick https://orcid.org/0000-0002-3351-760X
Dominique Broguiere https://orcid.org/0000-0001-9151-6683
Thomas Bronzwaer https://orcid.org/0000-0003-1151-3971
Sandra Bustamante https://orcid.org/0000-0001-6169-1894
Do-Young Byun https://orcid.org/0000-0003-1157-4109
John E. Carlstrom https://orcid.org/0000-0002-2044-7665
Chiara Ceccobello https://orcid.org/0000-0002-4767-9925
Andrew Chael https://orcid.org/0000-0003-2966-6220
Chi-kwan Chan https://orcid.org/0000-0001-6337-6126
Koushik Chatterjee https://orcid.org/0000-0002-2825-3590
Shami Chatterjee https://orcid.org/0000-0002-2878-1502
Ming-Tang Chen https://orcid.org/0000-0001-6573-3318
Yongjun Chen (陈永军) https://orcid.org/0000-0001-5650-6770
Xiaopeng Cheng https://orcid.org/0000-0003-4407-9868
Ilje Cho https://orcid.org/0000-0001-6083-7521
Pierre Christian https://orcid.org/0000-0001-6820-9941
Nicholas S. Conroy https://orcid.org/0000-0003-2886-2377
John E. Conway https://orcid.org/0000-0003-2448-9181
James M. Cordes https://orcid.org/0000-0002-4049-1882

Thomas M. Crawford https://orcid.org/0000-0001-9000-5013
Geoffrey B. Crew https://orcid.org/0000-0002-2079-3189
Alejandro Cruz-Osorio https://orcid.org/0000-0002-3945-6342
Yuzhu Cui (崔玉竹) https://orcid.org/0000-0001-6311-4345
Jordy Davelaar https://orcid.org/0000-0002-2685-2434
Mariafelicia De Laurentis https://orcid.org/0000-0002-9945-682X
Roger Deane https://orcid.org/0000-0003-1027-5043
Jessica Dempsey https://orcid.org/0000-0003-1269-9667
Gregory Desvignes https://orcid.org/0000-0003-3922-4055
Jason Dexter https://orcid.org/0000-0003-3903-0373
Vedant Dhruv https://orcid.org/0000-0001-6765-877X
Sheperd S. Doeleman https://orcid.org/0000-0002-9031-0904
Sean Dougal https://orcid.org/0000-0002-3769-1314
Sergio A. Dzib https://orcid.org/0000-0001-6010-6200
Ralph P. Eatough https://orcid.org/0000-0001-6196-4135
Razieh Emami https://orcid.org/0000-0002-2791-5011
Heino Falcke https://orcid.org/0000-0002-2526-6724
Joseph Farah https://orcid.org/0000-0003-4914-5625
Vincent L. Fish https://orcid.org/0000-0002-7128-9345
Ed Fomalont https://orcid.org/0000-0002-9036-2747
H. Alyson Ford https://orcid.org/0000-0002-9797-0972
Raquel Fraga-Encinas https://orcid.org/0000-0002-5222-1361
Per Friberg https://orcid.org/0000-0002-8010-8454
Christian M. Fromm https://orcid.org/0000-0002-1827-1656
Antonio Fuentes https://orcid.org/0000-0002-8773-4933
Peter Galison https://orcid.org/0000-0002-6429-3872
Charles F. Gammie https://orcid.org/0000-0001-7451-8935
Roberto García https://orcid.org/0000-0002-6584-7443
Olivier Gentaz https://orcid.org/0000-0002-0115-4605
Boris Georgiev https://orcid.org/0000-0002-3586-6424
Ciriaco Goddi https://orcid.org/0000-0002-2542-7743
Roman Gold https://orcid.org/0000-0003-2492-1966
Arturo I. Gómez-Ruiz https://orcid.org/0000-0001-9395-1670
José L. Gómez https://orcid.org/0000-0003-4190-7613
Minfeng Gu (顾敏峰) https://orcid.org/0000-0002-4455-6946
Mark Gurwell https://orcid.org/0000-0003-0685-3621
Kazuhiro Hada https://orcid.org/0000-0001-6906-772X
Daryl Haggard https://orcid.org/0000-0001-6803-2138
Michael H. Hecht https://orcid.org/0000-0002-4114-4583
Ronald Hesper https://orcid.org/0000-0003-1918-6098
Dirk Heumann https://orcid.org/0000-0002-7671-0047
Luis C. Ho (何子山) https://orcid.org/0000-0001-6947-5846
Paul Ho https://orcid.org/0000-0002-3412-4306
Mareki Honma https://orcid.org/0000-0003-4058-9000
Chih-Wei L. Huang https://orcid.org/0000-0001-5641-3953
Lei Huang (黄磊) https://orcid.org/0000-0002-1923-227X
Shiro Ikeda https://orcid.org/0000-0002-2462-1448
C. M. Violette Impellizzeri https://orcid.org/0000-0002-3443-2472
Makoto Inoue https://orcid.org/0000-0001-5037-3989
Sara Issaoun https://orcid.org/0000-0002-5297-921X
David J. James https://orcid.org/0000-0001-5160-4486
Buell T. Jannuzi https://orcid.org/0000-0002-1578-6582
Michael Janssen https://orcid.org/0000-0001-8685-6544
Britton Jeter https://orcid.org/0000-0003-2847-1712
Wu Jiang (江悟) https://orcid.org/0000-0001-7369-3539
Alejandra Jiménez-Rosales https://orcid.org/0000-0002-2662-3754
Michael D. Johnson https://orcid.org/0000-0002-4120-3029
Svetlana Jorstad https://orcid.org/0000-0001-6158-1708
Abhishek V. Joshi https://orcid.org/0000-0002-2514-5965
Taehyun Jung https://orcid.org/0000-0001-7003-8643
Mansour Karami https://orcid.org/0000-0001-7387-9333
Ramesh Karuppusamy https://orcid.org/0000-0002-5307-2919
Tomohisa Kawashima https://orcid.org/0000-0001-8527-0496
Garrett K. Keating https://orcid.org/0000-0002-3490-146X
Mark Kettenis https://orcid.org/0000-0002-6156-5617
Dong-Jin Kim https://orcid.org/0000-0002-7038-2118
Jae-Young Kim https://orcid.org/0000-0001-8229-7183
Jongsoo Kim https://orcid.org/0000-0002-1229-0426
Junhan Kim https://orcid.org/0000-0002-4274-9373
Motoki Kino https://orcid.org/0000-0002-2709-7338
Jun Yi Koay https://orcid.org/0000-0002-7029-6658
Prashant Kocherlakota https://orcid.org/0000-0001-7386-7439
Patrick M. Koch https://orcid.org/0000-0003-2777-5861
Shoko Koyama https://orcid.org/0000-0002-3723-3372
Carsten Kramer https://orcid.org/0000-0002-4908-4925
Michael Kramer https://orcid.org/0000-0002-4175-2271
Thomas P. Krichbaum https://orcid.org/0000-0002-4892-9586
Cheng-Yu Kuo https://orcid.org/0000-0001-6211-5581
Noemi La Bella https://orcid.org/0000-0002-8116-9427
Tod R. Lauer https://orcid.org/0000-0003-3234-7247
Daeyoung Lee https://orcid.org/0000-0002-3350-5588
Sang-Sung Lee https://orcid.org/0000-0002-6269-594X
Po Kin Leung https://orcid.org/0000-0002-8802-8256
Aviad Levis https://orcid.org/0000-0001-7307-632X
Zhiyuan Li (李志远) https://orcid.org/0000-0003-0355-6437
Rocco Lico https://orcid.org/0000-0001-7361-2460
Greg Lindahl https://orcid.org/0000-0002-6100-4772
Michael Lindqvist https://orcid.org/0000-0002-3669-0715
Mikhail Lisakov https://orcid.org/0000-0001-6088-3819
Jun Liu (刘俊) https://orcid.org/0000-0002-7615-7499
Kuo Liu https://orcid.org/0000-0002-2953-7376
Elisabetta Liuzzo https://orcid.org/0000-0003-0995-5201
Wen-Ping Lo https://orcid.org/0000-0003-1869-2503
Andrei P. Lobanov https://orcid.org/0000-0003-1622-1484
Laurent Loinard https://orcid.org/0000-0002-5635-3345
Colin J. Lonsdale https://orcid.org/0000-0003-4062-4654
Ru-Sen Lu (路如森) https://orcid.org/0000-0002-7692-7967
Jirong Mao (毛基荣) https://orcid.org/0000-0002-7077-7195
Nicola Marchili https://orcid.org/0000-0002-5523-7588
Sera Markoff https://orcid.org/0000-0001-9564-0876
Daniel P. Marrone https://orcid.org/0000-0002-2367-1080
Alan P. Marscher https://orcid.org/0000-0001-7396-3332
Iván Martí-Vidal https://orcid.org/0000-0003-3708-9611
Satoki Matsushita https://orcid.org/0000-0002-2127-7880
Lynn D. Matthews https://orcid.org/0000-0002-3728-8082

Lia Medeiros https://orcid.org/0000-0003-2342-6728
Karl M. Menten https://orcid.org/0000-0001-6459-0669
Daniel Michalik https://orcid.org/0000-0002-7618-6556
Izumi Mizuno https://orcid.org/0000-0002-7210-6264
Yosuke Mizuno https://orcid.org/0000-0002-8131-6730
James M. Moran https://orcid.org/0000-0002-3882-4414
Kotaro Moriyama https://orcid.org/0000-0003-1364-3761
Monika Moscibrodzka https://orcid.org/0000-0002-4661-6332
Cornelia Müller https://orcid.org/0000-0002-2739-2994
Alejandro Mus https://orcid.org/0000-0003-0329-6874
Gibwa Musoke https://orcid.org/0000-0003-1984-189X
Ioannis Myserlis https://orcid.org/0000-0003-3025-9497
Andrew Nadolski https://orcid.org/0000-0001-9479-9957
Hiroshi Nagai https://orcid.org/0000-0003-0292-3645
Neil M. Nagar https://orcid.org/0000-0001-6920-662X
Masanori Nakamura https://orcid.org/0000-0001-6081-2420
Ramesh Narayan https://orcid.org/0000-0002-1919-2730
Gopal Narayanan https://orcid.org/0000-0002-4723-6569
Iniyan Natarajan https://orcid.org/0000-0001-8242-4373
Joey Neilsen https://orcid.org/0000-0002-8247-786X
Roberto Neri https://orcid.org/0000-0002-7176-4046
Chunchong Ni https://orcid.org/0000-0003-1361-5699
Aristeidis Noutsos https://orcid.org/0000-0002-4151-3860
Michael A. Nowak https://orcid.org/0000-0001-6923-1315
Junghwan Oh https://orcid.org/0000-0002-4991-9638
Hiroki Okino https://orcid.org/0000-0003-3779-2016
Héctor Olivares https://orcid.org/0000-0001-6833-7580
Gisela N. Ortiz-León https://orcid.org/0000-0002-2863-676X
Tomoaki Oyama https://orcid.org/0000-0003-4046-2923
Feryal Özel https://orcid.org/0000-0003-4413-1523
Daniel C. M. Palumbo https://orcid.org/0000-0002-7179-3816
Georgios Filippos Paraschos https://orcid.org/0000-0001-6757-3098
Jongho Park https://orcid.org/0000-0001-6558-9053
Harriet Parsons https://orcid.org/0000-0002-6327-3423
Nimesh Patel https://orcid.org/0000-0002-6021-9421
Ue-Li Pen https://orcid.org/0000-0003-2155-9578
Dominic W. Pesce https://orcid.org/0000-0002-5278-9221
Richard Plambeck https://orcid.org/0000-0001-6765-9609
Oliver Porth https://orcid.org/0000-0002-4584-2557
Felix M. Pötzl https://orcid.org/0000-0002-6579-8311
Ben Prather https://orcid.org/0000-0002-0393-7734
Jorge A. Preciado-López https://orcid.org/0000-0002-4146-0113
Dimitrios Psaltis https://orcid.org/0000-0003-1035-3240
Hung-Yi Pu https://orcid.org/0000-0001-9270-8812
Venkatessh Ramakrishnan https://orcid.org/0000-0002-9248-086X
Ramprasad Rao https://orcid.org/0000-0002-1407-7944
Mark G. Rawlings https://orcid.org/0000-0002-6529-202X
Alexander W. Raymond https://orcid.org/0000-0002-5779-4767
Luciano Rezzolla https://orcid.org/0000-0002-1330-7103
Angelo Ricarte https://orcid.org/0000-0001-5287-0452
Bart Ripperda https://orcid.org/0000-0002-7301-3908
Freek Roelofs https://orcid.org/0000-0001-5461-3687
Alan Rogers https://orcid.org/0000-0003-1941-7458
Eduardo Ros https://orcid.org/0000-0001-9503-4892
Cristina Romero-Cañizales https://orcid.org/0000-0001-6301-9073
Arash Roshanineshat https://orcid.org/0000-0002-8280-9238
Alan L. Roy https://orcid.org/0000-0002-1931-0135
Ignacio Ruiz https://orcid.org/0000-0002-0965-5463
Chet Ruszczyk https://orcid.org/0000-0001-7278-9707
Kazi L. J. Rygl https://orcid.org/0000-0003-4146-9043
Salvador Sánchez https://orcid.org/0000-0002-8042-5951
David Sánchez-Argüelles https://orcid.org/0000-0002-7344-9920
Miguel Sánchez-Portal https://orcid.org/0000-0003-0981-9664
Mahito Sasada https://orcid.org/0000-0001-5946-9960
Kaushik Satapathy https://orcid.org/0000-0003-0433-3585
Tuomas Savolainen https://orcid.org/0000-0001-6214-1085
Jonathan Schonfeld https://orcid.org/0000-0002-8909-2401
Karl-Friedrich Schuster https://orcid.org/0000-0003-2890-9454
Lijing Shao https://orcid.org/0000-0002-1334-8853
Zhiqiang Shen (沈志强) https://orcid.org/0000-0003-3540-8746
Des Small https://orcid.org/0000-0003-3723-5404
Bong Won Sohn https://orcid.org/0000-0002-4148-8378
Jason SooHoo https://orcid.org/0000-0003-1938-0720
Kamal Souccar https://orcid.org/0000-0001-7915-5272
He Sun (孙赫) https://orcid.org/0000-0003-1526-6787
Fumie Tazaki https://orcid.org/0000-0003-0236-0600
Alexandra J. Tetarenko https://orcid.org/0000-0003-3906-4354
Paul Tiede https://orcid.org/0000-0003-3826-5648
Remo P. J. Tilanus https://orcid.org/0000-0002-6514-553X
Michael Titus https://orcid.org/0000-0001-9001-3275
Pablo Torne https://orcid.org/0000-0001-8700-6058
Efthalia Traianou https://orcid.org/0000-0002-1209-6500
Sascha Trippe https://orcid.org/0000-0003-0465-1559
Matthew Turk https://orcid.org/0000-0002-5294-0198
Ilse van Bemmel https://orcid.org/0000-0001-5473-2950
Huib Jan van Langevelde https://orcid.org/0000-0002-0230-5946
Daniel R. van Rossum https://orcid.org/0000-0001-7772-6131
Jesse Vos https://orcid.org/0000-0003-3349-7394
Jan Wagner https://orcid.org/0000-0003-1105-6109
Derek Ward-Thompson https://orcid.org/0000-0003-1140-2761
John Wardle https://orcid.org/0000-0002-8960-2942
Jonathan Weintroub https://orcid.org/0000-0002-4603-5204
Norbert Wex https://orcid.org/0000-0003-4058-2837
Robert Wharton https://orcid.org/0000-0002-7416-5209
Maciek Wielgus https://orcid.org/0000-0002-8635-4242
Kaj Wiik https://orcid.org/0000-0002-0862-3398
Gunther Witzel https://orcid.org/0000-0003-2618-797X
Michael F. Wondrak https://orcid.org/0000-0002-6894-1072
George N. Wong https://orcid.org/0000-0001-6952-2147
Qingwen Wu (吴庆文) https://orcid.org/0000-0003-4773-4987
Paul Yamaguchi https://orcid.org/0000-0002-6017-8199
Doosoo Yoon https://orcid.org/0000-0001-8694-8166

André Young https://orcid.org/0000-0003-0000-2682
Ken Young https://orcid.org/0000-0002-3666-4920
Ziri Younsi https://orcid.org/0000-0001-9283-1191
Feng Yuan (袁峰) https://orcid.org/0000-0003-3564-6437
Ye-Fei Yuan (袁业飞) https://orcid.org/0000-0002-7330-4756
J. Anton Zensus https://orcid.org/0000-0001-7470-3321
Shuo Zhang https://orcid.org/0000-0002-2967-790X
Guang-Yao Zhao https://orcid.org/0000-0002-4417-1659
Shan-Shan Zhao (赵杉杉) https://orcid.org/0000-0002-9774-3606

References

Akiyama, K., Ikeda, S., Pleau, M., et al. 2017a, AJ, 153, 159
Akiyama, K., Kuramochi, K., Ikeda, S., et al. 2017b, ApJ, 838, 1
Akiyama, K., Takahashi, R., Honma, M., Oyama, T., & Kobayashi, H. 2013, PASJ, 65, 91
Alberdi, A., Lara, L., Marcaide, J. M., et al. 1993, A&A, 277, L1
Arras, P., Frank, P., Leike, R., Westermann, R., & Enßlin, T. A. 2019, A&A, 627, A134
Astropy Collaboration, Price-Whelan, A. M., Sipőcz, B. M., et al. 2018, AJ, 156, 123
Astropy Collaboration, Robitaille, T. P., Tollerud, E., et al. 2013, A&A, 558, A33
Baganoff, F. K., Maeda, Y., Morris, M., et al. 2003, ApJ, 591, 891
Balick, B., & Brown, R. L. 1974, ApJ, 194, 265
Bardeen, J. M. 1973, in Black holes (Les astres occlus), ed. C. DeWitt & B. S. DeWitt (New York: Gordon & Breach), 215
Blackburn, L., Chan, C.-k., Crew, G. B., et al. 2019, ApJ, 882, 23
Blackburn, L., Pesce, D. W., Johnson, M. D., et al. 2020, ApJ, 894, 31
Bouman, K. L. 2017, PhD thesis, Massachusetts Institute of Technology
Bouman, K. L., Johnson, M. D., Dalca, A. V., et al. 2018, IEEE Trans Comput Imaging, 4, 512
Bouman, K. L., Johnson, M. D., Zoran, D., et al. 2016, IEEE Conf. on Computer Vision and Pattern Recognition (CVPR), Computational Imaging for VLBI Image Reconstruction (Piscataway, NJ: IEEE), 913
Bower, G. C., & Backer, D. C. 1998, ApJL, 507, L117
Bower, G. C., Falcke, H., Herrnstein, R. M., et al. 2004, Sci, 304, 704
Bower, G. C., Markoff, S., Brunthaler, A., et al. 2014, ApJ, 790, 1
Bower, G. C., Markoff, S., Dexter, J., et al. 2015, ApJ, 802, 69
Bower, G. C., Broderick, A., Dexter, J., et al. 2018, ApJ, 868, 101
Bower, G. C., Dexter, J., Asada, K., et al. 2019, ApJL, 881, L2
Boyce, H., Haggard, D., Witzel, G., et al. 2019, ApJ, 871, 161
Brinkerink, C. D., Müller, C., Falcke, H., et al. 2016, MNRAS, 462, 1382
Broderick, A. E., Fish, V. L., Johnson, M. D., et al. 2016, ApJ, 820, 137
Broderick, A. E., Gold, R., Georgiev, B., et al. 2022, ApJL, 930, L21
Broderick, A. E., Gold, R., Karami, M., et al. 2020a, ApJ, 897, 139
Broderick, A. E., Pesce, D. W., Tiede, P., Pu, H.-Y., & Gold, R. 2020b, ApJ, 898, 9
Carpenter, B., Gelman, A., Hoffman, M. D., et al. 2017, JSS, 76, 1
Chael, A. A. 2019, PhD thesis, Harvard University, Graduate School of Arts & Sciences
Chael, A. A., Johnson, M. D., Bouman, K. L., et al. 2018, ApJ, 857, 23
Chael, A. A., Johnson, M. D., Narayan, R., et al. 2016, ApJ, 829, 11
Chael, A. A., Chan, C. K., Bouman, K. L., et al. 2022, achael/eht-imaging: v1.2.4, Zenodo, doi:10.5281/zenodo.6519440
Cho, I., Zhao, G.-Y., Kawashima, T., et al. 2022, ApJ, 926, 108
Clark, B. G. 1980, A&A, 89, 377
Cornwell, T., Braun, R., & Briggs, D. S. 1999, in ASP Conf. Ser. 180, Synthesis Imaging in Radio Astronomy II, ed. G. B. Taylor, C. L. Carilli, & R. A. Perley (San Francisco, CA: ASP), 151
Cornwell, T. J. 2008, ISTSP, 2, 793
Davies, R. D., Walsh, D., & Booth, R. S. 1976, MNRAS, 177, 319
Dexter, J., Kelly, B., Bower, G. C., et al. 2014, MNRAS, 442, 2797
Do, T., Hees, A., Ghez, A., et al. 2019, Sci, 365, 664
Doeleman, S., Agol, E., Backer, D., et al. 2009, in Astro2010: The Astronomy and Astrophysics Decadal Survey, Science White Papers, Imaging an Event Horizon: submm-VLBI of a Super Massive Black Hole, 68 (Charlottesville, Va: NRAO)
Doeleman, S. S., Weintroub, J., Rogers, A. E. E., et al. 2008, Natur, 455, 78
Eckart, A., & Genzel, R. 1997, MNRAS, 284, 576
Event Horizon Telescope Collaboration, Akiyama, K., Alberdi, A., et al. 2019a, ApJL, 875, L1, (M87* Paper I)
Event Horizon Telescope Collaboration, Akiyama, K., Alberdi, A., et al. 2019b, ApJL, 875, L2, (M87* Paper II)
Event Horizon Telescope Collaboration, Akiyama, K., Alberdi, A., et al. 2019c, ApJL, 875, L3, (M87* Paper III)
Event Horizon Telescope Collaboration, Akiyama, K., Alberdi, A., et al. 2019d, ApJL, 875, L4, (M87* Paper IV)
Event Horizon Telescope Collaboration, Akiyama, K., Alberdi, A., et al. 2019e, ApJL, 875, L5, (M87* Paper V)
Event Horizon Telescope Collaboration, Akiyama, K., Alberdi, A., et al. 2019f, ApJL, 875, L6, (M87* Paper VI)
Event Horizon Telescope Collaboration, Akiyama, K., Alberdi, A., et al. 2021a, ApJL, 910, L12, (M87* Paper VII)
Event Horizon Telescope Collaboration, Akiyama, K., Alberdi, A., et al. 2021b, ApJL, 910, L13, (M87* Paper VIII)
Event Horizon Telescope Collaboration, Akiyama, K., Alberdi, A., et al. 2022a, ApJL, 930, L12, (Paper I)
Event Horizon Telescope Collaboration, Akiyama, K., Alberdi, A., et al. 2022b, ApJL, 930, L13, (Paper II)
Event Horizon Telescope Collaboration, Akiyama, K., Alberdi, A., et al. 2022c, ApJL, 930, L15, (Paper IV)
Event Horizon Telescope Collaboration, Akiyama, K., Alberdi, A., et al. 2022d, ApJL, 930, L16, (Paper V)
Event Horizon Telescope Collaboration, Akiyama, K., Alberdi, A., et al. 2022e, ApJL, 930, L17, (Paper VI)
Falcke, H., Goss, W. M., Matsuo, H., et al. 1998, ApJ, 499, 731
Falcke, H., Markoff, S., & Bower, G. C. 2009, A&A, 496, 77
Falcke, H., Melia, F., & Agol, E. 2000, ApJL, 528, L13
Farah, J. R., Galison, P. L., Akiyama, K., et al. 2022, ApJL, 930, L18
Fish, V. L., Doeleman, S. S., Beaudoin, C., et al. 2011, ApJL, 727, L36
Fish, V. L., Johnson, M. D., Doeleman, S. S., et al. 2016, ApJ, 820, 90
Fish, V. L., Johnson, M. D., Lu, R.-S., et al. 2014, ApJ, 795, 134
Frail, D. A., Diamond, P. J., Cordes, J. M., & van Langevelde, H. J. 1994, ApJL, 427, L43
Gebhardt, K., Adams, J., Richstone, D., et al. 2011, ApJ, 729, 119
Genzel, R., Eisenhauer, F., & Gillessen, S. 2010, RvMP, 82, 3121
Genzel, R., Schödel, R., Ott, T., et al. 2003, Natur, 425, 934
Georgiev, B., Pesce, D. W., Broderick, A. E., et al. 2022, ApJL, 930, L20
Ghez, A. M., Klein, B. L., Morris, M., & Becklin, E. E. 1998, ApJ, 509, 678
Ghez, A. M., Salim, S., Weinberg, N. N., et al. 2008, ApJ, 689, 1044
Ghez, A. M., Wright, S. A., Matthews, K., et al. 2004, ApJL, 601, L159
Gillessen, S., Eisenhauer, F., Fritz, T. K., et al. 2009, ApJL, 707, L114
Gillessen, S., Plewa, P. M., Eisenhauer, F., et al. 2017, ApJ, 837, 30
Goddi, C., Martí-Vidal, I., Messias, H., et al. 2019, PASP, 131, 075003
Goddi, C., Martí-Vidal, I., Messias, H., et al. 2021, ApJL, 910, L14
Goldreich, P., & Sridhar, S. 1995, ApJ, 438, 763
Goodman, J., & Narayan, R. 1989, MNRAS, 238, 995
Gravity Collaboration, Abuter, R., Amorim, A., et al. 2018a, A&A, 615, L15
Gravity Collaboration, Abuter, R., Amorim, A., et al. 2018b, A&A, 618, L10
Gravity Collaboration, Abuter, R., Amorim, A., et al. 2019, A&A, 625, L10
Gravity Collaboration, Bauböck, M., Dexter, J., et al. 2020, A&A, 635, A143
Gwinn, C. R., Kovalev, Y. Y., Johnson, M. D., & Soglasnov, V. A. 2014, ApJL, 794, L14
Harris, C. R., Millman, K. J., van der Walt, S. J., et al. 2020, Natur, 585, 357
Hilbert, D. 1917, Nachrichten von der Königlichen Gesellschaft der Wissenschaften zu Göttingen—Mathematisch-physikalische Klasse (Berlin: Weidmannsche Buchhandlung)
Högbom, J. A. 1974, A&AS, 15, 417
Honma, M., Akiyama, K., Uemura, M., & Ikeda, S. 2014, PASJ, 66, 95
Hora, J. L., Witzel, G., Ashby, M. L. N., et al. 2014, ApJ, 793, 120
Hunter, J. D. 2007, CSE, 9, 90
Issaoun, S., Johnson, M. D., Blackburn, L., et al. 2019, ApJ, 871, 30
Issaoun, S., Johnson, M. D., Blackburn, L., et al. 2021, ApJ, 915, 99
Issaoun, S., Wielgus, M., Jorstad, S., et al. 2022, ApJ, submitted
Janssen, M., Goddi, C., van Bemmel, I. M., et al. 2019, A&A, 626, A75
Johnson, M. D. 2016, ApJ, 833, 74
Johnson, M. D., Bouman, K. L., Blackburn, L., et al. 2017, ApJ, 850, 172
Johnson, M. D., Fish, V. L., Doeleman, S. S., et al. 2015, Sci, 350, 1242
Johnson, M. D., & Gwinn, C. R. 2015, ApJ, 805, 180
Johnson, M. D., Lupsasca, A., Strominger, A., et al. 2020, SciA, 6, eaaz1310
Johnson, M. D., & Narayan, R. 2016, ApJ, 826, 170
Johnson, M. D., Narayan, R., Psaltis, D., et al. 2018, ApJ, 865, 104
Kim, J.-Y., Krichbaum, T. P., Broderick, A. E., et al. 2020, A&A, 640, A69
Krichbaum, T. P., Graham, D. A., Witzel, A., et al. 1998, A&A, 335, L106
Krichbaum, T. P., Zensus, J. A., Witzel, A., et al. 1993, A&A, 274, L37

Lartillot, N., & Philippe, H. 2006, Syst. Biol., 55, 195
Lee, D., & Gammie, C. F. 2021, ApJ, 906, 39
Levis, A., Lee, D., Tropp, J. A., Gammie, C. F., & Bouman, K. L. 2021, in Proc. of the IEEE/CVF Int.Conf. on Computer Vision, Inference of Black Hole Fluid-Dynamics From Sparse Interferometric Measurements (Piscataway, NJ: IEEE), 2340
Lo, K. Y., Backer, D. C., Ekers, R. D., et al. 1985, Natur, 315, 124
Lo, K. Y., Shen, Z.-Q., Zhao, J.-H., & Ho, P. T. P. 1998, ApJL, 508, L61
Lu, R.-S., Krichbaum, T. P., Eckart, A., et al. 2011, A&A, 525, A76
Lu, R.-S., Krichbaum, T. P., Roy, A. L., et al. 2018, ApJ, 859, 60
Luminet, J.-P. 1979, A&A, 75, 228
Macquart, J.-P., & Bower, G. C. 2006, ApJ, 641, 302
Marcaide, J. M., Alberdi, A., Lara, L., Pérez-Torres, M. A., & Diamond, P. J. 1999, A&A, 343, 801
Marrone, D. P., Moran, J. M., Zhao, J.-H., & Rao, R. 2006, ApJ, 640, 308
Martí-Vidal, I., Vlemmings, W. H. T., & Muller, S. 2016, A&A, 593, A61
Matthews, L. D., Crew, G. B., Doeleman, S. S., et al. 2018, PASP, 130, 015002
McKinney, W. 2010, in Proc. of the 9th Python in Science Conf., Data Structures for Statistical Computing in Python, ed. S. van der Walt & J. Millman (SciPy), 56
McMullin, J. P., Waters, B., Schiebel, D., Young, W., & Golap, K. 2007, in ASP Conf. Ser. 376, Astronomical Data Analysis Software and Systems XVI, ed. R. A. Shaw, F. Hill, & D. J. Bell (San Francisco, CA: ASP), 127
Menten, K. M., Reid, M. J., Eckart, A., & Genzel, R. 1997, ApJL, 475, L111
Meyer, L., Do, T., Ghez, A., et al. 2008, ApJL, 688, L17
Miller-Jones, J. C., Tetarenko, A. J., Sivakoff, G. R., et al. 2019, Natur, 569, 374
Moriyama, K., Akiyama, K., Cho, I., et al. 2022, SMILI v0.2.0, Zenodo, doi:10.5281/zenodo.6522933
Muñoz, D. J., Marrone, D. P., Moran, J. M., & Rao, R. 2012, ApJ, 745, 115
Narayan, R. 1992, RSPTA, 341, 151
Narayan, R., & Goodman, J. 1989, MNRAS, 238, 963
Narayan, R., & Nityananda, R. 1986, ARA&A, 24, 127
Neilsen, J., Markoff, S., Nowak, M. A., et al. 2015, ApJ, 799, 199
Neilsen, J., Nowak, M. A., Gammie, C., et al. 2013, ApJ, 774, 42
Ortiz-León, G. N., Johnson, M. D., Doeleman, S. S., et al. 2016, ApJ, 824, 40
Palumbo, D. C., Doeleman, S. S., Johnson, M. D., Bouman, K. L., & Chael, A. A. 2019, ApJ, 881, 62
Pesce, D. W. 2021, AJ, 161, 178
Psaltis, D., Johnson, M., Narayan, R., et al. 2018, arXiv:1805.01242
Rau, U. 2012, Proc. SPIE, 8500, 85000N
Rauch, C., Ros, E., Krichbaum, T. P., et al. 2016, A&A, 587, A37
Reid, M. J. 2009, IJMPD, 18, 889
Reid, M. J., & Brunthaler, A. 2004, ApJ, 616, 872
Rickett, B. J. 1990, ARA&A, 28, 561
Roelofs, F., Johnson, M. D., Shiokawa, H., Doeleman, S. S., & Falcke, H. 2017, ApJ, 847, 55
Scherrer, C., & Zhao, T. 2020, Soss: Declarative Probabilistic Programming via Runtime Code Generation, Zenodo, doi:10.5281/zenodo.5520061
Schwab, F. R. 1984, AJ, 89, 1076
Schwarz, U. J. 1978, A&A, 65, 345
Shen, Z.-Q., Lo, K. Y., Liang, M.-C., Ho, P. T. P., & Zhao, J.-H. 2005, Natur, 438, 62
Shepherd, M. 2011, Difmap: Synthesis Imaging of Visibility Data, Astrophysics Source Code Library, ascl:1103.001
Shepherd, M. C. 1997, in ASP Conf. Ser. 125, Astronomical Data Analysis Software and Systems VI, ed. G. Hunt & H. Payne (San Francisco, CA: ASP), 77
Shepherd, M. C., Pearson, T. J., & Taylor, G. B. 1995, BAAS, 27, 903
Speagle, J. S. 2020, MNRAS, 493, 3132
Stewart, I., Fenech, D., & Muxlow, T. 2011, A&A, 535, A81
Sun, H., & Bouman, K. L. 2021, in Proc. of the AAAI Conf. on Artificial Intelligence, Deep Probabilistic Imaging: Uncertainty Quantification and Multi-modal Solution Characterization for Computational Imaging, 35 (Cambridge, MA: AAAI Press), 2628
Sun, H., Bouman, K. L., Tiede, P., et al. 2022, ApJ in press, arXiv:2201.08506
Syed, S., Bouchard-Côté, A., Deligiannidis, G., & Doucet, A. 2019, arXiv:1905.02939
The pandas development team 2020, pandas-dev/pandas: Pandaspandas-dev/pandas: Pandas, Zenodo, doi:10.5281/zenodo.3509134
Thompson, A. R., Moran, J. M., & Swenson, G. W., Jr. 2017, Interferometry and Synthesis in Radio Astronomy (Berlin: Springer)
Tiede, P., Broderick, A. E., & Palumbo, D. C. M. 2022, ApJ, 925, 122
Virtanen, P., Gommers, R., Oliphant, T. E., et al. 2020, NatMe, 17, 261
von Laue, M. 1921, Die Allgemeine Relativitätstheorie Und Einsteins Lehre Von Der Schwerkraft (Braunschweig: Friedrich Vieweg & Sohn)
Whitney, A. R., Cappallo, R., Aldrich, W., et al. 2004, RaSc, 39, RS1007
Wiaux, Y., Jacques, L., Puy, G., Scaife, A. M. M., & Vandergheynst, P. 2009a, MNRAS, 395, 1733
Wiaux, Y., Puy, G., Boursier, Y., & Vandergheynst, P. 2009b, MNRAS, 400, 1029
Wielgus, M., Marchili, N., Martí-Vidal, I., et al. 2022, ApJL, 930, L19
Wielgus, M., Palumbo, D., & Hamilton, L. 2020, LCG Metric https://github.com/wielgusm/mwtools/blob/master/LCG_metric.py
Witzel, G., Martinez, G., Hora, J., et al. 2018, ApJ, 863, 15

Event Horizon Telescope Collaboration,
Kazunori Akiyama[1,2,3], Antxon Alberdi[4], Walter Alef[5], Juan Carlos Algaba[6], Richard Anantua[3,7,8], Keiichi Asada[9],
Rebecca Azulay[5,10,11], Uwe Bach[5], Anne-Kathrin Baczko[5], David Ball[12], Mislav Baloković[13], John Barrett[1],
Michi Bauböck[14], Bradford A. Benson[15,16], Dan Bintley[17,18], Lindy Blackburn[3,7], Raymond Blundell[7],
Katherine L. Bouman[19], Geoffrey C. Bower[20,21], Hope Boyce[22,23], Michael Bremer[24], Christiaan D. Brinkerink[25],
Roger Brissenden[3,7], Silke Britzen[5], Avery E. Broderick[26,27,28], Dominique Broguiere[24], Thomas Bronzwaer[25],
Sandra Bustamante[29], Do-Young Byun[30,31], John E. Carlstrom[16,32,33,34], Chiara Ceccobello[35], Andrew Chael[36,37],
Chi-kwan Chan[12,38,39], Koushik Chatterjee[3,7], Shami Chatterjee[40], Ming-Tang Chen[20], Yongjun Chen (陈永军)[41,42],
Xiaopeng Cheng[30], Ilje Cho[4], Pierre Christian[43], Nicholas S. Conroy[7,44], John E. Conway[35], James M. Cordes[40],
Thomas M. Crawford[16,32], Geoffrey B. Crew[1], Alejandro Cruz-Osorio[45], Yuzhu Cui (崔玉竹)[46,47,48],
Jordy Davelaar[25,49,50], Mariafelicia De Laurentis[45,51,52], Roger Deane[53,54,55], Jessica Dempsey[17,18,56],
Gregory Desvignes[5,57], Jason Dexter[58], Vedant Dhruv[14], Sheperd S. Doeleman[3,7], Sean Dougal[12],
Sergio A. Dzib[5,24], Ralph P. Eatough[5,59], Razieh Emami[7], Heino Falcke[25], Joseph Farah[60,61], Vincent L. Fish[1],
Ed Fomalont[62], H. Alyson Ford[12], Raquel Fraga-Encinas[25], William T. Freeman[63,64], Per Friberg[17,18],
Christian M. Fromm[5,45,65], Antonio Fuentes[4], Peter Galison[3,66,67], Charles F. Gammie[14,44,68], Roberto García[24],
Olivier Gentaz[24], Boris Georgiev[26,27,28], Ciriaco Goddi[69,70], Roman Gold[45,71], Arturo I. Gómez-Ruiz[72,73],
José L. Gómez[4], Minfeng Gu (顾敏峰)[41,74], Mark Gurwell[7], Kazuhiro Hada[47,48], Daryl Haggard[22,23], Kari Haworth[7],
Michael H. Hecht[1], Ronald Hesper[75], Dirk Heumann[12], Luis C. Ho (何子山)[76,77], Paul Ho[9,17,18],
Mareki Honma[47,48,78], Chih-Wei L. Huang[9], Lei Huang (黄磊)[41,74], David H. Hughes[72], Shiro Ikeda[2,79,80,81],

C. M. Violette Impellizzeri[62,82], Makoto Inoue[9], Sara Issaoun[7,37], David J. James[83], Buell T. Jannuzi[12],
Michael Janssen[5], Britton Jeter[9], Wu Jiang (江悟)[41], Alejandra Jiménez-Rosales[25], Michael D. Johnson[3,7],
Svetlana Jorstad[84], Abhishek V. Joshi[14], Taehyun Jung[30,31], Mansour Karami[26,27], Ramesh Karuppusamy[5],
Tomohisa Kawashima[85], Garrett K. Keating[7], Mark Kettenis[86], Dong-Jin Kim[5], Jae-Young Kim[5,30,87],
Jongsoo Kim[30], Junhan Kim[12,19], Motoki Kino[2,88], Jun Yi Koay[9], Prashant Kocherlakota[45], Yutaro Kofuji[47,78],
Patrick M. Koch[9], Shoko Koyama[9,89], Carsten Kramer[24], Michael Kramer[5], Thomas P. Krichbaum[5],
Cheng-Yu Kuo[9,90], Noemi La Bella[25], Tod R. Lauer[91], Daeyoung Lee[14], Sang-Sung Lee[30], Po Kin Leung[92],
Aviad Levis[19], Zhiyuan Li (李志远)[93,94], Rocco Lico[4,95], Greg Lindahl[7], Michael Lindqvist[35], Mikhail Lisakov[5],
Jun Liu (刘俊)[5], Kuo Liu[5], Elisabetta Liuzzo[96], Wen-Ping Lo[9,97], Andrei P. Lobanov[5], Laurent Loinard[98,99],
Colin J. Lonsdale[1], Ru-Sen Lu (路如森)[5,41,42], Jirong Mao (毛基荣)[100,101,102], Nicola Marchili[5,96],
Sera Markoff[103,104], Daniel P. Marrone[12], Alan P. Marscher[84], Iván Martí-Vidal[10,11], Satoki Matsushita[9],
Lynn D. Matthews[1], Lia Medeiros[12,105,106], Karl M. Menten[5], Daniel Michalik[16,107], Izumi Mizuno[17,18],
Yosuke Mizuno[45,46,108], James M. Moran[3,7], Kotaro Moriyama[1,45,47], Monika Moscibrodzka[25], Cornelia Müller[5,25],
Alejandro Mus[10,11], Gibwa Musoke[25,103], Ioannis Myserlis[109], Andrew Nadolski[44], Hiroshi Nagai[2,48],
Neil M. Nagar[110], Masanori Nakamura[9,111], Ramesh Narayan[3,7], Gopal Narayanan[29], Iniyan Natarajan[53,112],
Antonios Nathanail[45,113], Santiago Navarro Fuentes[109], Joey Neilsen[114], Roberto Neri[24], Chunchong Ni[26,27,28],
Aristeidis Noutsos[5], Michael A. Nowak[115], Junghwan Oh[116], Hiroki Okino[47,78], Héctor Olivares[25],
Gisela N. Ortiz-León[5,99], Tomoaki Oyama[47], Feryal Özel[12], Daniel C. M. Palumbo[3,7], Georgios Filippos Paraschos[5],
Jongho Park[9,117], Harriet Parsons[17,18], Nimesh Patel[7], Ue-Li Pen[9,26,118,119,120], Dominic W. Pesce[3,7], Vincent Piétu[24],
Richard Plambeck[121], Aleksandar PopStefanija[29], Oliver Porth[45,103], Felix M. Pötzl[5,122], Ben Prather[14],
Jorge A. Preciado-López[26], Dimitrios Psaltis[12], Hung-Yi Pu[9,123,124], Venkatessh Ramakrishnan[110,125,126],
Ramprasad Rao[7], Mark G. Rawlings[17,18,127], Alexander W. Raymond[3,7], Luciano Rezzolla[45,128,129], Angelo Ricarte[3,7],
Bart Ripperda[50,130], Freek Roelofs[3,7,25], Alan Rogers[1], Eduardo Ros[5], Cristina Romero-Cañizales[9],
Arash Roshanineshat[12], Helge Rottmann[5], Alan L. Roy[5], Ignacio Ruiz[109], Chet Ruszczyk[1], Kazi L. J. Rygl[96],
Salvador Sánchez[109], David Sánchez-Argüelles[72,73], Miguel Sánchez-Portal[109], Mahito Sasada[47,131,132],
Kaushik Satapathy[12], Tuomas Savolainen[5,126,133], F. Peter Schloerb[29], Jonathan Schonfeld[7], Karl-Friedrich Schuster[24],
Lijing Shao[5,77], Zhiqiang Shen (沈志强)[41,42], Des Small[86], Bong Won Sohn[30,31,134], Jason SooHoo[1],
Kamal Souccar[29], He Sun (孙赫)[19], Fumie Tazaki[47], Alexandra J. Tetarenko[37,135], Paul Tiede[3,7],
Remo P. J. Tilanus[12,25,82,136], Michael Titus[1], Pablo Torne[5,109], Efthalia Traianou[4,5], Tyler Trent[12], Sascha Trippe[137],
Matthew Turk[44], Ilse van Bemmel[86], Huib Jan van Langevelde[82,86,138], Daniel R. van Rossum[25], Jesse Vos[25],
Jan Wagner[5], Derek Ward-Thompson[139], John Wardle[140], Jonathan Weintroub[3,7], Norbert Wex[5], Robert Wharton[5],
Maciek Wielgus[5], Kaj Wiik[141], Gunther Witzel[5], Michael F. Wondrak[25,142], George N. Wong[106,143],
Qingwen Wu (吴庆文)[144], Paul Yamaguchi[7], Doosoo Yoon[103], André Young[25], Ken Young[7], Ziri Younsi[45,145],
Feng Yuan (袁峰)[41,74,146], Ye-Fei Yuan (袁业飞)[147], J. Anton Zensus[5], Shuo Zhang[148], Guang-Yao Zhao[4], and
Shan-Shan Zhao (赵杉杉)[41]

[1] Massachusetts Institute of Technology Haystack Observatory, 99 Millstone Road, Westford, MA 01886, USA
[2] National Astronomical Observatory of Japan, 2-21-1 Osawa, Mitaka, Tokyo 181-8588, Japan
[3] Black Hole Initiative at Harvard University, 20 Garden Street, Cambridge, MA 02138, USA
[4] Instituto de Astrofísica de Andalucía-CSIC, Glorieta de la Astronomía s/n, E-18008 Granada, Spain
[5] Max-Planck-Institut für Radioastronomie, Auf dem Hügel 69, D-53121 Bonn, Germany
[6] Department of Physics, Faculty of Science, Universiti Malaya, 50603 Kuala Lumpur, Malaysia
[7] Center for Astrophysics | Harvard & Smithsonian, 60 Garden Street, Cambridge, MA 02138, USA
[8] Department of Physics & Astronomy, The University of Texas at San Antonio, One UTSA Circle, San Antonio, TX 78249, USA
[9] Institute of Astronomy and Astrophysics, Academia Sinica, 11F of Astronomy-Mathematics Building, AS/NTU No. 1, Sec. 4, Roosevelt Rd., Taipei 10617, Taiwan, R.O.C.
[10] Departament d'Astronomia i Astrofísica, Universitat de València, C. Dr. Moliner 50, E-46100 Burjassot, València, Spain
[11] Observatori Astronòmic, Universitat de València, C. Catedrático José Beltrán 2, E-46980 Paterna, València, Spain
[12] Steward Observatory and Department of Astronomy, University of Arizona, 933 N. Cherry Ave., Tucson, AZ 85721, USA
[13] Yale Center for Astronomy & Astrophysics, Yale University, 52 Hillhouse Avenue, New Haven, CT 06511, USA
[14] Department of Physics, University of Illinois, 1110 West Green Street, Urbana, IL 61801, USA
[15] Fermi National Accelerator Laboratory, MS209, P.O. Box 500, Batavia, IL 60510, USA
[16] Department of Astronomy and Astrophysics, University of Chicago, 5640 South Ellis Avenue, Chicago, IL 60637, USA
[17] East Asian Observatory, 660 N. A'ohoku Place, Hilo, HI 96720, USA
[18] James Clerk Maxwell Telescope (JCMT), 660 N. A'ohoku Place, Hilo, HI 96720, USA
[19] California Institute of Technology, 1200 East California Boulevard, Pasadena, CA 91125, USA
[20] Institute of Astronomy and Astrophysics, Academia Sinica, 645 N. A'ohoku Place, Hilo, HI 96720, USA
[21] Department of Physics and Astronomy, University of Hawaii at Manoa, 2505 Correa Road, Honolulu, HI 96822, USA
[22] Department of Physics, McGill University, 3600 rue University, Montréal, QC H3A 2T8, Canada
[23] McGill Space Institute, McGill University, 3550 rue University, Montréal, QC H3A 2A7, Canada
[24] Institut de Radioastronomie Millimétrique (IRAM), 300 rue de la Piscine, F-38406 Saint Martin d'Hères, France

[25] Department of Astrophysics, Institute for Mathematics, Astrophysics and Particle Physics (IMAPP), Radboud University, P.O. Box 9010, 6500 GL Nijmegen, The Netherlands
[26] Perimeter Institute for Theoretical Physics, 31 Caroline Street N, Waterloo, ON N2L 2Y5, Canada
[27] Department of Physics and Astronomy, University of Waterloo, 200 University Avenue W, Waterloo, ON N2L 3G1, Canada
[28] Waterloo Centre for Astrophysics, University of Waterloo, Waterloo, ON N2L 3G1, Canada
[29] Department of Astronomy, University of Massachusetts, Amherst, MA 01003, USA
[30] Korea Astronomy and Space Science Institute, Daedeok-daero 776, Yuseong-gu, Daejeon 34055, Republic of Korea
[31] University of Science and Technology, Gajeong-ro 217, Yuseong-gu, Daejeon 34113, Republic of Korea
[32] Kavli Institute for Cosmological Physics, University of Chicago, 5640 South Ellis Avenue, Chicago, IL 60637, USA
[33] Department of Physics, University of Chicago, 5720 South Ellis Avenue, Chicago, IL 60637, USA
[34] Enrico Fermi Institute, University of Chicago, 5640 South Ellis Avenue, Chicago, IL 60637, USA
[35] Department of Space, Earth and Environment, Chalmers University of Technology, Onsala Space Observatory, SE-43992 Onsala, Sweden
[36] Princeton Center for Theoretical Science, Jadwin Hall, Princeton University, Princeton, NJ 08544, USA
[37] NASA Hubble Fellowship Program, Einstein Fellow
[38] Data Science Institute, University of Arizona, 1230 N. Cherry Ave., Tucson, AZ 85721, USA
[39] Program in Applied Mathematics, University of Arizona, 617 N. Santa Rita, Tucson, AZ 85721, USA
[40] Cornell Center for Astrophysics and Planetary Science, Cornell University, Ithaca, NY 14853, USA
[41] Shanghai Astronomical Observatory, Chinese Academy of Sciences, 80 Nandan Road, Shanghai 200030, People's Republic of China
[42] Key Laboratory of Radio Astronomy, Chinese Academy of Sciences, Nanjing 210008, People's Republic of China
[43] Physics Department, Fairfield University, 1073 North Benson Road, Fairfield, CT 06824, USA
[44] Department of Astronomy, University of Illinois at Urbana-Champaign, 1002 West Green Street, Urbana, IL 61801, USA
[45] Institut für Theoretische Physik, Goethe-Universität Frankfurt, Max-von-Laue-Straße 1, D-60438 Frankfurt am Main, Germany
[46] Tsung-Dao Lee Institute, Shanghai Jiao Tong University, Shengrong Road 520, Shanghai, 201210, People's Republic of China
[47] Mizusawa VLBI Observatory, National Astronomical Observatory of Japan, 2-12 Hoshigaoka, Mizusawa, Oshu, Iwate 023-0861, Japan
[48] Department of Astronomical Science, The Graduate University for Advanced Studies (SOKENDAI), 2-21-1 Osawa, Mitaka, Tokyo 181-8588, Japan
[49] Department of Astronomy and Columbia Astrophysics Laboratory, Columbia University, 550 W. 120th Street, New York, NY 10027, USA
[50] Center for Computational Astrophysics, Flatiron Institute, 162 Fifth Avenue, New York, NY 10010, USA
[51] Dipartimento di Fisica "E. Pancini," Universitá di Napoli "Federico II," Compl. Univ. di Monte S. Angelo, Edificio G, Via Cinthia, I-80126, Napoli, Italy
[52] INFN Sez. di Napoli, Compl. Univ. di Monte S. Angelo, Edificio G, Via Cinthia, I-80126, Napoli, Italy
[53] Wits Centre for Astrophysics, University of the Witwatersrand, 1 Jan Smuts Avenue, Braamfontein, Johannesburg 2050, South Africa
[54] Department of Physics, University of Pretoria, Hatfield, Pretoria 0028, South Africa
[55] Centre for Radio Astronomy Techniques and Technologies, Department of Physics and Electronics, Rhodes University, Makhanda 6140, South Africa
[56] ASTRON, Oude Hoogeveensedijk 4, 7991 PD Dwingeloo, The Netherlands
[57] LESIA, Observatoire de Paris, Université PSL, CNRS, Sorbonne Université, Université de Paris, 5 place Jules Janssen, F-92195 Meudon, France
[58] JILA and Department of Astrophysical and Planetary Sciences, University of Colorado, Boulder, CO 80309, USA
[59] National Astronomical Observatories, Chinese Academy of Sciences, 20A Datun Road, Chaoyang District, Beijing 100101, People's Republic of China
[60] Las Cumbres Observatory, 6740 Cortona Drive, Suite 102, Goleta, CA 93117-5575, USA
[61] Department of Physics, University of California, Santa Barbara, CA 93106-9530, USA
[62] National Radio Astronomy Observatory, 520 Edgemont Road, Charlottesville, VA 22903, USA
[63] Department of Electrical Engineering and Computer Science, Massachusetts Institute of Technology, 32-D476, 77 Massachusetts Ave., Cambridge, MA 02142, USA
[64] Google Research, 355 Main St., Cambridge, MA 02142, USA
[65] Institut für Theoretische Physik und Astrophysik, Universität Würzburg, Emil-Fischer-Str. 31, D-97074 Würzburg, Germany
[66] Department of History of Science, Harvard University, Cambridge, MA 02138, USA
[67] Department of Physics, Harvard University, Cambridge, MA 02138, USA
[68] NCSA, University of Illinois, 1205 W. Clark St., Urbana, IL 61801, USA
[69] Dipartimento di Fisica, Università degli Studi di Cagliari, SP Monserrato-Sestu km 0.7, I-09042 Monserrato, Italy
[70] INAF—Osservatorio Astronomico di Cagliari, Via della Scienza 5, I-09047, Selargius, CA, Italy
[71] CP3-Origins, University of Southern Denmark, Campusvej 55, DK-5230 Odense M, Denmark
[72] Instituto Nacional de Astrofísica, Óptica y Electrónica. Apartado Postal 51 y 216, 72000. Puebla Pue., MÉxico
[73] Consejo Nacional de Ciencia y Tecnología, Av. Insurgentes Sur 1582, 03940, Ciudad de México, MÉxico
[74] Key Laboratory for Research in Galaxies and Cosmology, Chinese Academy of Sciences, Shanghai 200030, People's Republic of China
[75] NOVA Sub-mm Instrumentation Group, Kapteyn Astronomical Institute, University of Groningen, Landleven 12, 9747 AD Groningen, The Netherlands
[76] Department of Astronomy, School of Physics, Peking University, Beijing 100871, People's Republic of China
[77] Kavli Institute for Astronomy and Astrophysics, Peking University, Beijing 100871, People's Republic of China
[78] Department of Astronomy, Graduate School of Science, The University of Tokyo, 7-3-1 Hongo, Bunkyo-ku, Tokyo 113-0033, Japan
[79] The Institute of Statistical Mathematics, 10-3 Midori-cho, Tachikawa, Tokyo, 190-8562, Japan
[80] Department of Statistical Science, The Graduate University for Advanced Studies (SOKENDAI), 10-3 Midori-cho, Tachikawa, Tokyo 190-8562, Japan
[81] Kavli Institute for the Physics and Mathematics of the Universe, The University of Tokyo, 5-1-5 Kashiwanoha, Kashiwa, 277-8583, Japan
[82] Leiden Observatory, Leiden University, Postbus 2300, 9513 RA Leiden, The Netherlands
[83] ASTRAVEO LLC, PO Box 1668, Gloucester, MA 01931, USA
[84] Institute for Astrophysical Research, Boston University, 725 Commonwealth Ave., Boston, MA 02215, USA
[85] Institute for Cosmic Ray Research, The University of Tokyo, 5-1-5 Kashiwanoha, Kashiwa, Chiba 277-8582, Japan
[86] Joint Institute for VLBI ERIC (JIVE), Oude Hoogeveensedijk 4, 7991 PD Dwingeloo, The Netherlands
[87] Department of Astronomy and Atmospheric Sciences, Kyungpook National University, Daegu 702-701, Republic of Korea
[88] Kogakuin University of Technology & Engineering, Academic Support Center, 2665-1 Nakano, Hachioji, Tokyo 192-0015, Japan
[89] Niigata University, 8050 Ikarashi-nino-cho, Nishi-ku, Niigata 950-2181, Japan
[90] Physics Department, National Sun Yat-Sen University, No. 70, Lien-Hai Road, Kaosiung City 80424, Taiwan, R.O.C.
[91] National Optical Astronomy Observatory, 950 N. Cherry Ave., Tucson, AZ 85719, USA
[92] Department of Physics, The Chinese University of Hong Kong, Shatin, N.T., Hong Kong
[93] School of Astronomy and Space Science, Nanjing University, Nanjing 210023, People's Republic of China
[94] Key Laboratory of Modern Astronomy and Astrophysics, Nanjing University, Nanjing 210023, People's Republic of China
[95] INAF-Istituto di Radioastronomia, Via P. Gobetti 101, I-40129 Bologna, Italy

[96] INAF-Istituto di Radioastronomia & Italian ALMA Regional Centre, Via P. Gobetti 101, I-40129 Bologna, Italy
[97] Department of Physics, National Taiwan University, No. 1, Sec. 4, Roosevelt Rd., Taipei 10617, Taiwan, R.O.C
[98] Instituto de Radioastronomía y Astrofísica, Universidad Nacional Autónoma de México, Morelia 58089, MÉxico
[99] Instituto de Astronomía, Universidad Nacional Autónoma de México (UNAM), Apdo Postal 70-264, Ciudad de México, MÉxico
[100] Yunnan Observatories, Chinese Academy of Sciences, 650011 Kunming, Yunnan Province, People's Republic of China
[101] Center for Astronomical Mega-Science, Chinese Academy of Sciences, 20A Datun Road, Chaoyang District, Beijing, 100012, People's Republic of China
[102] Key Laboratory for the Structure and Evolution of Celestial Objects, Chinese Academy of Sciences, 650011 Kunming, People's Republic of China
[103] Anton Pannekoek Institute for Astronomy, University of Amsterdam, Science Park 904, 1098 XH, Amsterdam, The Netherlands
[104] Gravitation and Astroparticle Physics Amsterdam (GRAPPA) Institute, University of Amsterdam, Science Park 904, 1098 XH Amsterdam, The Netherlands
[105] NSF Astronomy and Astrophysics Postdoctoral Fellow
[106] School of Natural Sciences, Institute for Advanced Study, 1 Einstein Drive, Princeton, NJ 08540, USA
[107] Science Support Office, Directorate of Science, European Space Research and Technology Centre (ESA/ESTEC), Keplerlaan 1, 2201 AZ Noordwijk, The Netherlands
[108] School of Physics and Astronomy, Shanghai Jiao Tong University, 800 Dongchuan Road, Shanghai, 200240, People's Republic of China
[109] Institut de Radioastronomie Millimétrique (IRAM), Avenida Divina Pastora 7, Local 20, E-18012, Granada, Spain
[110] Astronomy Department, Universidad de Concepción, Casilla 160-C, Concepción, Chile
[111] National Institute of Technology, Hachinohe College, 16-1 Uwanotai, Tamonoki, Hachinohe City, Aomori 039-1192, Japan
[112] South African Radio Astronomy Observatory, Observatory 7925, Cape Town, South Africa
[113] Department of Physics, National and Kapodistrian University of Athens, Panepistimiopolis, GR 15783 Zografos, Greece
[114] Department of Physics, Villanova University, 800 Lancaster Avenue, Villanova, PA 19085, USA
[115] Physics Department, Washington University CB 1105, St. Louis, MO 63130, USA
[116] Sejong University, 209 Neungdong-ro, Gwangjin-gu, Seoul, Republic of Korea
[117] EACOA Fellow
[118] Canadian Institute for Theoretical Astrophysics, University of Toronto, 60 St. George Street, Toronto, ON M5S 3H8, Canada
[119] Dunlap Institute for Astronomy and Astrophysics, University of Toronto, 50 St. George Street, Toronto, ON M5S 3H4, Canada
[120] Canadian Institute for Advanced Research, 180 Dundas St. W, Toronto, ON M5G 1Z8, Canada
[121] Radio Astronomy Laboratory, University of California, Berkeley, CA 94720, USA
[122] Department of Physics, University College Cork, Kane Building, College Road, Cork T12 K8AF, Ireland
[123] Department of Physics, National Taiwan Normal University, No. 88, Sec. 4, Tingzhou Rd., Taipei 116, Taiwan, R.O.C.
[124] Center of Astronomy and Gravitation, National Taiwan Normal University, No. 88, Sec. 4, Tingzhou Road, Taipei 116, Taiwan, R.O.C.
[125] Finnish Centre for Astronomy with ESO, FI-20014 University of Turku, Finland
[126] Aalto University Metsähovi Radio Observatory, Metsähovintie 114, FI-02540 Kylmälä, Finland
[127] Gemini Observatory/NSF NOIRLab, 670 N. A'ohoku Place, Hilo, HI 96720, USA
[128] Frankfurt Institute for Advanced Studies, Ruth-Moufang-Strasse 1, 60438 Frankfurt, Germany
[129] School of Mathematics, Trinity College, Dublin 2, Ireland
[130] Department of Astrophysical Sciences, Peyton Hall, Princeton University, Princeton, NJ 08544, USA
[131] Department of Physics, Tokyo Institute of Technology, 2-12-1 Ookayama, Meguro-ku, Tokyo 152-8551, Japan
[132] Hiroshima Astrophysical Science Center, Hiroshima University, 1-3-1 Kagamiyama, Higashi-Hiroshima, Hiroshima 739-8526, Japan
[133] Aalto University Department of Electronics and Nanoengineering, PL 15500, FI-00076 Aalto, Finland
[134] Department of Astronomy, Yonsei University, Yonsei-ro 50, Seodaemun-gu, 03722 Seoul, Republic of Korea
[135] Department of Physics and Astronomy, Texas Tech University, Lubbock, TX 79409-1051, USA
[136] Netherlands Organisation for Scientific Research (NWO), Postbus 93138, 2509 AC Den Haag, The Netherlands
[137] Department of Physics and Astronomy, Seoul National University, Gwanak-gu, Seoul 08826, Republic of Korea
[138] University of New Mexico, Department of Physics and Astronomy, Albuquerque, NM 87131, USA
[139] Jeremiah Horrocks Institute, University of Central Lancashire, Preston PR1 2HE, UK
[140] Physics Department, Brandeis University, 415 South Street, Waltham, MA 02453, USA
[141] Tuorla Observatory, Department of Physics and Astronomy, University of Turku, Finland
[142] Radboud Excellence Fellow of Radboud University, Nijmegen, The Netherlands
[143] Princeton Gravity Initiative, Princeton University, Princeton, NJ 08544, USA
[144] School of Physics, Huazhong University of Science and Technology, Wuhan, Hubei, 430074, People's Republic of China
[145] Mullard Space Science Laboratory, University College London, Holmbury St. Mary, Dorking, Surrey, RH5 6NT, UK
[146] School of Astronomy and Space Sciences, University of Chinese Academy of Sciences, No. 19A Yuquan Road, Beijing 100049, People's Republic of China
[147] Astronomy Department, University of Science and Technology of China, Hefei 230026, People's Republic of China
[148] Bard College, 30 Campus Road, Annandale-on-Hudson, NY 12504, USA